Advanced battery management system for electric vehicles with modular battery packs

By

Adnan Ashraf

A thesis submitted to the University of Birmingham
for the degree of
DOCTOR OF PHILOSOPHY

Department of Electronic, Electrical and Systems Engineering

School of Engineering

University of Birmingham

Sept 2024

This page is left intentionally blank in anticipation of double-sided printing.

Abstract

Higher voltage systems are becoming more common in electric vehicle (EV) technologies due to the convenience of quick charging. More series-connected cells in the battery pack are required due to the voltage rise. The two main issues raised by this transition are maximising power loss in the traction inverter due to higher voltage and guaranteeing that the voltage/ state of charge (SOC) remain balanced during rapid charging. The purpose of this thesis is to investigate these issues and provide recommendations for improving the effectiveness and efficiency of high-voltage EV battery packs. There are several cell balancing methods in the literature, but they don't offer flexible DC link for a traction inverter. For the purpose to provide a flexible DC connection voltage and ensure cell balancing for quick charging, this thesis offers a modular battery pack that uses a bypassed cell balancing topology. In this balancing method, the battery pack's each module is linked to a pair of switches, typically MOSFETS. These switches enable the series or bypass connection for each module in a battery pack. The SOC estimation of a battery cell is the most challenging part of the battery management system. Thus, the voltage-based control algorithm is implemented to eliminate the need for SOC estimation, and the SOC measurement results indicate that lithium-ion (li-ion) cell voltage provides a good approximation of the SOC. The default li-ion battery cell model in MATLAB Simulink is optimised by using actual parameters of the cell. The parameters tuning of an equivalent circuit model of an induction motor is performed to develop an approximately realistic motor model.

The battery charger is designed to adjust its supply voltage because the voltage of the EV battery pack varies by using the proposed bypass cell balancing topology. Field-oriented control (FOC) is implemented to control the speed of the motor and provide the voltage amplitude required

according to the speed of the motor. The controller adjusts the DC-link voltage according to the motor speed and provide adaptable DC-link voltage for the traction inverter while maintaining the voltage balance of the battery pack module.

The performance of the proposed modular battery pack is tested for voltage balancing, controller effectiveness, residual imbalance, and providing variable DC link voltage for a dynamic load condition using hardware in the loop and simulation to test the different scenarios of initial SOC or voltage imbalance. The result analyses of charging and discharging battery pack shows the proposed bypass balancing method achieved approximate zero SOC/voltage residual imbalance between series connected modules for rapid charging of 2C rate. The power loss assessments at the battery pack and traction inverter levels shows the proposed method reduce the overall system power loss and improved power efficiency.

Keywords: Battery management system, modular battery pack, battery charger, cell balancing, battery power loss, inverter power loss

Acknowledgements

In the name of **Almighty Allah**, the Most Gracious, the Most Merciful. Alhamdulillah, for all **HIS** blessings upon me.

I would like to convey my appreciation for this incredible journey of my PhD studies. It's been a long road, and without the help of some amazing individuals, it was hard for me to stay focused to the finish.

First and foremost, I want to express my gratitude to **Professor Pietro Tricoli**, my supervisor, for his unwavering support and encouragement in helping me finish this thesis. He has helped me through the highs and lows of my studies as a mentor. He has taught me so much, and I appreciate his patience and faith in me.

I would like to honour my father, **Ashraf Khan**. Although He is not with us, I still remember his words of wisdom, love, and sacrifice that inspired me to keep going and shaped me into the person I am today.

My strength has come from your unending love, prayers, and constant support, my beloved **Mother**. Your support and generosity have been the source of my motivation.

I am truly grateful to my beautiful **Wife** and son **Muhriz Adnan Khan**, for always understanding and supporting me. My achievement has been largely attributed to your love, support, and patience. Together, we kept going through the storms to accomplish this journey.

I am thankful for your encouragement and support, brothers **Zeeshan** and **Shahrukh**, and **Sisters** who have been my strength.

I express my sincere appreciation to my father-in-law **Ali Akbar** and **Mother-in-law,** and to my wife's siblings for their support and encouragement.

I would like to sincerely thank **Prof. Umar Shahbaz Khan** for his advice and willingness to help anytime I need it.

I express my gratitude to **Dr. Pual Weston** and **Dr. Faysal Hardan** for their support and advice.

I also want to express my gratitude to **Hakime**, **Halise**, **Basit**, **Mothanna**, and **Nabeel** for their continuous encouragement and support along this journey.

Finally, but most importantly, I want to thank my extended **Family** and **Friends** for being supportive and a part of this journey.

Table of Contents

List of Figures

List of Tables

List of Abbreviations

Term	Explanation
12S1P	12 Series and 1 Parallel
AFOC	Air-Gap Flux-Oriented Control
Aout	Analog output
BMS	Battery Management System
C2C	Cell to Cell
C2P	Cell to Pack
C2P2C	Cell to Pack to Cell
CAN	Controller Area Network
CC	Constant Current
CCCV	Constant Current Constant Voltage
CO2	Carbon Dioxide
CV	Constant Voltage
Din	Digital input
EN	European Norm
EV	Electric Vehicle
FOC	Field-Oriented Control
GHG	Greenhouse Gas
GWh	Giga Watt hour
HIL	Hardware-in-the-loop
IC	Integrated Circuit
IEC	International Electrotechnical Commission
ISO	International Organisation for Standardisation
li-ion	lithium-ion
MOSFET	Metal-Oxide-Semiconductor Field-Effect Transistor
Op-Amp	operational amplifier
P2C	Pack to Cell
PI	Proportional Integral
RFOC	Rotor Flux-Oriented Control
SAE	Society of Automotive Engineers International
SBP	Smart Battery Pack
SFOC	Stator Flux-Oriented Control
SiC	Silicon Carbide

SOC	State of Charge
SOH	State of Health
THD	Total Harmonic Distortion
TI	Taxes Instruments
UK	United Kingdom
WLTP	Worldwide Harmonised Light Vehicle Test Procedure
WLTP-3	WLTP Class 3
ZCS	Zero-Current Switching
ZVS	Zero-Voltage Switching

Chapter 1: Introduction

The introductory chapter of this thesis provides a short background on increased demand for Electric vehicles (EVs) and lithium ion (li-ion) batteries, and the EV battery packs specification. Furthermore, it explains problem statements, research hypothesis, research objectives, and provides the thesis structure.

1.1 Background

Production of li-ion batteries is increasing quickly as EVs becomes more popular as a means of reducing transportation's carbon footprint [1]. Giga factories are crucial to the production of EVs because they can produce batteries and other necessary parts in large quantities, which lowers prices and boosts productivity. For example, Jaguar Land Rover (JLR) and Tata Motors have partnered to use these facilities to speed up the research and manufacturing of EVs. This partnership emphasises how crucial giga plants are to expanding operations, guaranteeing a consistent supply of batteries, and eventually increasing consumer access to EVs [2].

EVs can help in reducing Greenhouse Gas (GHG)emissions, combating climate change, and reducing harm to the environment. These harmful emissions can be further decreased when EVs are charged using sustainable energy sources, such as solar or wind power [3]. The Bloomberg study [4] on EV sales in 2024 reported in Figure 1.1, shows that the number of EVs sold worldwide has been rising over time, with 74 million EVs expected to be sold by 2040. The growth rate of EV production will be the same or higher because of government incentives to businesses. By 2025, it is predicted that 21 million EVs will have been produced worldwide.

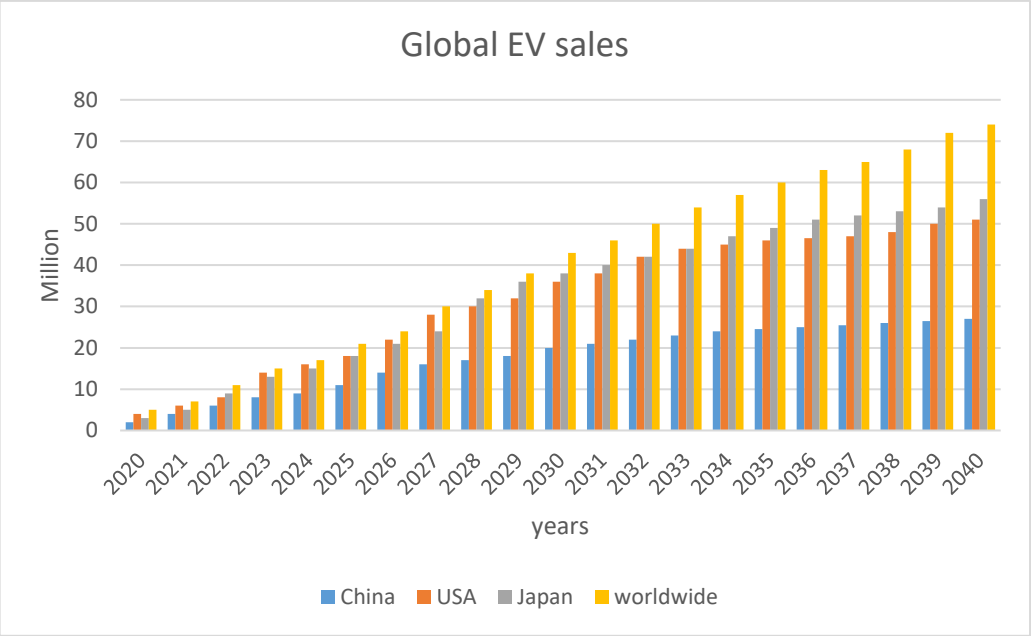

Figure 1. 1 Growth of EV sales (2020-2040), adapted from [4]

Li-ion battery use is significantly rising because of the growing demand for EVs. Since Li-ion batteries have a low self-discharge rate, a long lifespan, and a high energy density, they are recommended for electric vehicles [5, 6]. According to a Bloomberg report [4], the global demand for li-ion batteries will reach 35 million metric tons in 2040, depicted in Figure 1.2.

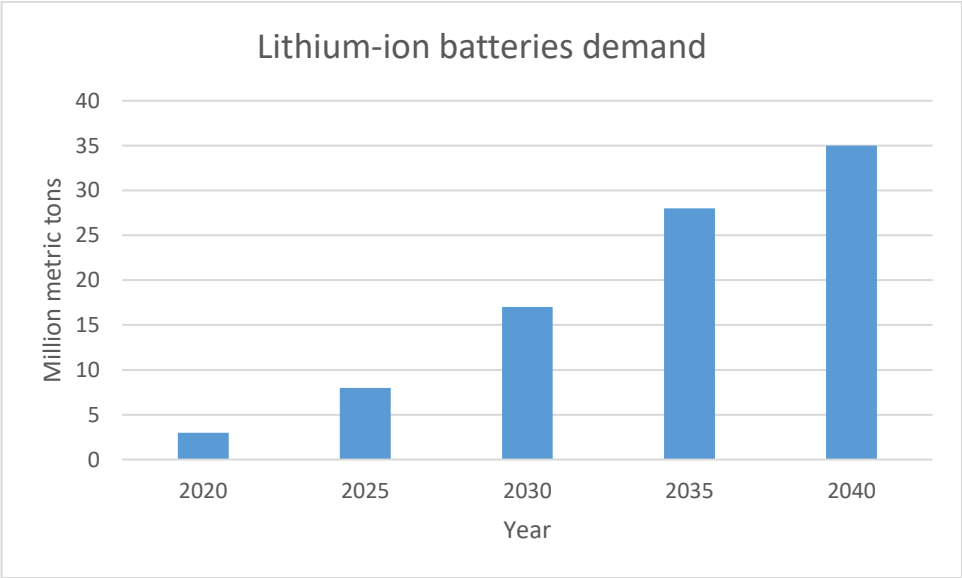

Figure 1. 2 Demand of lithium-ion batteries (2020-2040), adapted from [4]

The Li-ion battery sector has shown high potential for the EV industry. EVs require long cycle life, high-temperature tolerance, high capacity and energy density, high power, and energy battery cells. As the demand of EV and li-ion batteries are increasing, thus, the problems associated with li-ion batteries, like cell balancing also gets more attention in recent years that is further discussed in chapter 2, section 2.4. Table 1.1 displays the commercially available EVs using li-ion batteries [7].

Table 1. 1 EV battery pack parameters available in the market

Ref	**Model**	**Nominal Capacity (kWh)**	**Voltage (V)**	**Range (miles)**
[8]	Tesla Model S	75	400	170-335
[9]	Nissan Leaf	40	400	105-220
[7]	Chevrolet Bolt EV	150	400	259
[10]	Audi Q8 e-Tron	114	400	225-445
[11]	Jaguar I-Pace EV400	90	400	170-340
[7]	BMW i3	154	400	153-190
[12]	Hyundai Kona Electric	67.5	400	170-360
[13]	Porsche Taycan Turbo	93.4	800	200-390
[14]	Hyundai IONIQ 5 (Long Range 2WD)	77.4	800	170-355
[15]	Kia EV6 (Long Range 2WD)	77.4	800	180-370

There are primarily two types of EVs battery packs available in the market, 400-volt and 800-volt battery packs. Small cars employ the 400-volt battery pack architecture, while sports cars and high-powered vehicles like trucks and lorries use the 800-volt battery pack system. The reason for the vehicle's varying range is because of the various weather conditions. The high-powered EVs with fixed DC-link voltage leads to the high-power losses at traction inverter that as explained in chapter 5, section 5.4.

1.2 Problem statement

Particularly in the automotive sector lithium batteries have evolved into the industry's preferred energy storage solution for powering EVs. A battery pack is created by connecting multiple Li-ion cells in series and parallel to meet the voltage and power requirements needed for EVs. The safety, effectiveness, and durability of the Li-ion battery packs are prerequisites regarding the overall growth of EVs. Unfortunately, there are two main problems with EVs, one is the battery pack cell imbalance, and the other is the traction inverter power loss.

The cell imbalance is the main issue of battery pack, since the high voltage battery pack is required to give EVs substantial power and range, more cells must be connected in series. Although this method is effective in raising the battery pack's voltage levels, however, the increasing number of series-connected cells increases the control complexity and difficulty of minimizing cell imbalances in EV battery packs

Traction inverter efficiency is another challenge for EVs because of the recent increase in high-voltage infrastructure and fixed DC-link voltage. The traditional method of feeding the EV traction inverter with a fixed DC-link voltage leads to potentially higher power losses then variable DC-link voltage. Furthermore, variable DC-link voltage can produce higher modulation index at lower speed of motor to reduce the Total Harmonic Distortion (THD). The modulation index is the ratio between carrier signal and modulating signal, to produce the desired AC output voltage, while THD is the presence of unwanted harmonic frequencies or distortion in the output waveform of inverter. The higher THD causes electrical noise, a risk of damaging electrical components and reduce overall efficiency of the system.

1.3 Research Hypothesis

If the EV battery pack is modularised by using bypass balancing method to provide variable DC-link voltage for the traction inverter, then the traction inverter power loss will be reduced as well as SOC/voltage balancing between series connected battery modules can be achieved with the better performance at the state-of-the-art system.

1.4 Research Claims

1. Utilising the bypass balancing method to modularise EV battery packs is an effective means to improve the traction inverter's efficiency. It provides variable DC link which will reduce the traction inverter's power loss.
2. The bypass balancing method will achieve rapid SOC/voltage balancing between series-connected battery modules with approximately zero residual imbalance.

1.5 Research objective

The primary objective of this research is the development of a modular battery pack with SOC/voltage balancing capabilities to reduce SOC/voltage imbalances between battery modules and reduce the traction inverter power loss.

1. The investigation and mitigation of cell imbalance in high-voltage EV battery pack modules while charging or discharging through the development of a proposed bypass cell balancing architecture.
    1.1. A detailed examination of present cell balancing technologies to compere the number of components and power loss with proposed balancing topology. Presented in chapter 2, section 2.4.
    1.2. Overview and identify the factors of optimalisation of the proposed bypass balancing method. Presented in chapter 2, section 2.8 and 2.9.

1.3. The development of a battery cell model by modifying the parameters of MATLAB Simulink li-ion battery model according to real cell parameters. Presented in chapter 3, section 3.2.

1.4. Development of CCCV charger for battery pack charging mode with proposed bypass topology that modify the charger's supply voltage based on the quantity of series-connected modules. Presented in chapter 3, section 3.3 and 3.4.

1.5. Establish a control strategy to actively balance module voltages and track each individual module voltage in real-time. Presented in chapter 4, section 4.2.1.

1.6. The calculation of the power losses at the EV battery pack level and compare with other cell balancing methods. Presented in chapter 6.

2. The development of modular battery pack system for EVs that can automatically modify the DC-link voltage supplied to the EV traction inverter based on the motor speed to reduce power loss and provide cell balance during discharge.

    2.1. Development of an EV induction motor model that closely resembles real-world circumstances using actual parameters. Presented in chapter 3, section 3.5.

    2.2. Development of FOC for an EV induction motor, to provide speed control under varying load conditions, and determines the relationship between supply voltage and motor speed. Presented in chapter 3, section 3.7. Which will be further used for providing variable DC-link voltage to the traction inverter and perform cell balancing during discharge.

    2.3. Create a control algorithm that monitors individual module voltages and modifies the DC-link voltage, considering a dynamic load condition (variable motor speed profile) as well as facilitates voltage balancing during the battery pack discharging. Presented in chapter 4, section 4.3.1.

2.4. The calculation of power loss at traction inverter level for fixed and variable DC-link configurations and analyse the effect of both configuration on traction inverter power loss. Presented in chapter 6.

3. Implementation of the modular battery pack based on proposed bypass balancing topology using MATLAB Simulink and HIL. Perform testing for different cases of initial SOC imbalance under controlled conditions, to verify the proposed balancing method's performance and control algorithm. Results are presented in chapter 5 and 7.

1.6 Research Publications

The research paper published in peer-reviewed international journal is:

1. “Review of cell balancing schemes for electric vehicle battery management systems,” (Energies, MDPI), (Published).

1.7 Thesis structure

This thesis is further divided into six chapters other than introduction. The other chapters that follow are:

Chapter 2 presents an explanation of the battery management system and its standards, the causes of cell imbalance and balancing control algorithms. Additionally, this chapter provides review of existing cell balancing topologies, the energy transfer methods, and the latest trends of cell balancing topologies and important aspects for optimisation of bypass cell balancing technique.

Chapter 3 explains the modelling of a battery cell and three-phase induction motor, the controller design for battery charging, and the FOC for motor speed control.

Chapter 4 introduces the proposed bypass balancing method and the operating principle of EV battery pack charging and discharging mode of operation, and controller design flowchart of voltage balancing and variable DC-link voltage.

Chapter 5 analyses the performance of the proposed bypass method and modular battery packs by conducting testing based on MALTB Simulink. The simulation results validate the controller design and proposed bypass method considering low and high initial SOC difference for charging and discharging.

Chapter 6 This chapter provides the power loss assessment at both traction inverter and battery pack level.

Chapter 7 provides the experimental verification of simulation results with HIL.

The conclusion and future recommendations of this research are presented in Chapter 8.

Chapter 2: Literature Review

An overview of the battery management system is provided in this chapter, along with information on battery standards, cell imbalance causes, and control algorithms for cell balancing. The chapter also provides a detail of current advancements in cell balancing methods, energy transfer strategies, and existing cell balancing topologies. This chapter more specifically presents an overview and highlights crucial aspects for optimization of the bypass cell balancing technique.

2.1 Battery System Standards

Table 2.1 displays the British and international standards for safety requirements for li-ion batteries. The “International Electrotechnical Commission” (IEC), the “Society of Automotive Engineers International” (SAE), and the “International Organisation for Standardisation” (ISO) are the international organisations that standardise EVs. ISO focuses on applications for vehicles and the recent ISO standards about li-ion batteries in EVs include ISO 6469 and ISO 12405-4. The ISO 6469 offers several specifications for EV's overall safety. To support EV manufacturers the ISO 12405-4 provides testing methodologies to assess the fundamental attributes of battery systems, such as reliability, performance, and functionality. The IEC has issued standards for traction batteries, such as the IEC 62660 series, which are primarily for li-ion battery safety requirements as well as performance, reliability, and abuse testing. The automobile industry, along with other associated industries, extensively adopts the authoritative standards set by SAE. SAE J2464 and SAE J2929 are battery safety standards. The standard SAE J2464 provides the requirements for battery abuse testing, and the focus of SAE J1766 is

on EV crash integrity testing. The main regional standard, which refers to ISO and IEC standards.

Table 2. 1 Important EV battery safety standards, adapted from [16]

Name	Number	Description
ISO	ISO 6469-1	safety requirements for rechargeable energy storage systems (RESS) of EV
	ISO 6469-2	Operating the safety of vehicles and protecting against failures
	ISO 6469-3	protecting people from electric shock
	ISO 6469-4	electrical safety after an accident
	ISO 12405-4	System and battery pack performance testing
IEC	IEC 62660-1	Performance evaluation
	IEC 62660-2	Testing for reliability and abuse
	IEC 62660-3	Safety specifications and testing procedures
SAE	SAE J1766	Recommended procedure for assessing the crash integrity of electric, fuel cell, and hybrid electric vehicles
	SAE J2464	Rechargeable energy storage systems for electric and hybrid vehicles: abuse and safety testing
	SAE J2929	Safety standard for the battery systems of electric and hybrid vehicles: lithium-based rechargeable cells
British	BS EN 62133-2	Requirements for safety while using secondary cells that are portable, and batteries formed of them in portable applications
	BS EN 62619	Batteries and secondary lithium cells for industrial usage
	BS EN 62660-2	road vehicles powered by battery. safety requirements. cars powered by electricity and equipped with a reusable energy source.

2.2 Battery Management System

BMS is required to ensure the better performance and secure operation of EV battery packs. Initially, BMS involved simple monitoring of voltage and current to avoid excessive charging and discharging, which could damage the batteries [17]. The developments in BMS technology are more important than before for maximising battery performance, increasing their lifespan,

and guaranteeing general safety. Improving BMS capabilities to satisfy EVs' evolving needs has drawn a lot of attention lately [18]. The primary functions of the BMS include monitoring individual cell voltages, charging and discharging management, states estimation, fault diagnosis, data logging and communication, safety, thermal management, and cell balancing. A brief explanation of BMS functions is presented here and shown in Figure 2.1.

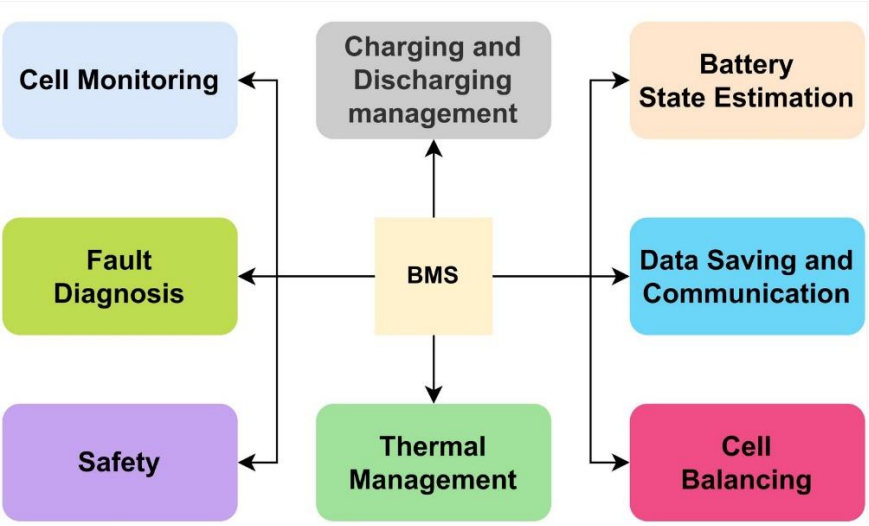

Figure 2. 1 Battery Management System functions

2.2.1 Cell Monitoring

Cell monitoring is an important function of BMS that involves monitoring and evaluating each battery pack cell condition regularly [19]. Each battery cell in a pack increases or decreases the overall performance, capacity, and health of the battery system. Cell monitoring enables the BMS to take corrective action when necessary and guarantees that each cell works within certain limits [20]. The BMS keeps continuously measure each cell voltages and calculate the voltage difference between them. Variations from the typical voltage range may be a sign of unbalanced cells, overcharging, or undercharging. Additionally, during the charging and discharging processes, BMS monitors each cell current [21].

2.2.2 Charging and Discharging management

To maintain safe and effective functioning, the BMS monitors and manages the electrical energy that enters and exits the battery pack. By regulating the charging voltage and current, the BMS controls the charging procedure [22]. To avoid overcharging, which can result in overheating, a shorter battery life, and safety risks, it makes sure the battery is charged within safe bounds. The BMS carefully controls the charging process when using fast charging to avoid overheating or thermal stress. BMS may dynamically adjust the charging parameters to achieve a balance between charging speed and battery health [23]. To maintain safe operation and avoid over-discharging, the BMS regulates the voltage and discharge current. Over-discharging can shorten the battery's lifespan and cause harm. Like charging current optimisation, the BMS modifies the discharging current according to temperature, battery state, and load requirement [24].

2.2.3 States Estimation

The voltage and current of every battery cell must be continuously monitored by BMS to calculate the battery states. The two main elements of battery state estimation are the SOC and SOH. The percentage of the cell's total capacity that is left on charge is known as the SOC. SOH is an indicator of the overall health of the cell [25].The BMS uses several models and algorithms to calculate SOC, like, Coulomb-Counting, open circuit voltage-based, and Kalman filtering. Every approach has advantages and disadvantages, and BMS may combine different strategies to increase the accuracy of SOC estimation. Coulomb-Counting determines the SOC by integrating the current entering or leaving the battery over time [26]. This is simple method of SOC estimation, but it requires the information of initial SOC. Additionally, SOC can be estimated by measuring the open circuit voltage [27], but, under dynamic conditions like heavy

loads or fast charge/discharge only voltage measurement may not provide accurate SOC information [28]. Multiple information voltage, current, and temperature, are combined by Kalman filters to produce better SOC estimation.

2.2.4 Fault Diagnosis

The BMS is responsible measuring several parameters to spot any potential issues with the battery system. The battery pack and each cell voltages are continuously monitored by the BMS. The two main kinds of voltage faults are undervoltage, when the cell voltage drops below the cutoff voltage, and overvoltage, when the cell voltage exceeds the fully charged voltage limit [29]. Voltage imbalances, cell deterioration, or any other problems can occur due to these failures during charging or discharging process [30]. Likewise, BMS regularly monitoring the temperature and current of each cell [31].

2.2.5 Data Saving and Communication

The BMS collects, stores, and distributes data regarding the temperature, voltage, and current of each cell. BMS tracking these variables over time makes it easier to determine SOC and SOH. Data logs include details about the type of fault and its location that can help in rapid troubleshooting and solution [32]. The BMS uses CAN protocol to communicate with a variety of external interfaces. These interfaces make it possible to communicate with the battery charger, main control unit, and other essential electronic parts of the EVs. Managing the charging process requires communication with external charging infrastructure [33].

2.2.6 Safety

In EVs, the safety feature of a BMS is essential for guaranteeing the security of the battery pack, the vehicle itself, and the occupant. To prevent and reduce potential problems related to

the usage of high-voltage battery systems, the BMS integrates several safety features. The BMS performs preventative measures, like lowering the charging current or disconnecting the battery, if the voltage exceeds safe limits to avoid overvoltage scenarios that could cause thermal runaway [34]. In the same way, BMS protects from undervoltage caused by sudden discharge. To avoid undervoltage conditions that could harm the battery, the BMS may restrict the discharge current or initiate a low-power mode. Additional safety features of the BMS include isolation of the unsafe cell, emergency shutdown, and short circuit protection [35].

2.2.7 Thermal Management

Thermal management is monitoring and controlling the temperature of individual cells and battery packs to ensure optimal performance and security. Thermal imaging sensors can be included for more advanced BMS to give a greater understanding of the battery pack's temperature distribution [36]. This maintains consistent thermal conditions which helps in the diagnosis of temperature faults. To disperse excess heat, the BMS activates cooling systems when temperatures climb beyond acceptable limits[37]. Depending on the needs and design of the vehicle, common cooling techniques include air cooling and liquid cooling. To improve performance and ensure safe operating conditions, the BMS controls the charging and discharging current of the battery pack based on temperature readings [38].

2.2.8 Cell Balancing

BMS needs to regulate each battery pack cell's SOC and voltage to guarantee that each cell functions within specified limits and to reduce imbalances that can affect performance, safety, and battery life overall [39]. Every single series-connected cell in the battery pack is continuously monitored for voltage by the BMS [40, 41]. Different cell capacities, self-discharge rates, temperature differences, manufacturing variances, uneven internal resistance,

irregular charging and discharging current, and other factors can all lead to SOC or voltage imbalances among series-connected cells. The BMS continuously analyses and modifies the voltages distribution across series-connected cells, particularly under dynamic circumstances like fast charging and fluctuating load demands. Additionally, to guarantee that each cell in a battery pack operates within its voltage range limit and to avoid overcharging and over discharging an effective cell balancing is necessary.

2.3 Fundamentals of Cell Balancing

2.3.1 Cell Imbalances

The temperature characteristics, capacity, impedance, self-discharge rate, and SOC of each cell is always different [42]. Even if the cells come from the same production lot, manufacturer, and model, this is still true [43]. Although manufacturers attempt to match the capacity of the cells as closely as possible, however, small variations in each cell's capacity, impedance, and self-discharge rate can eventually become the source of the variation in voltage or SOC between cells. An imbalance between cells can be caused by anything that could lead to a divergence in the SOC or voltage between cells. All the cells can begin with the same amount of initial $SOC(t-1)$, have the same capacity (Q_r), and current (I_{bat}). However, during charging or discharging, cell SOC diverges due to different internal impedance or efficiency (η_{bat}) of individual cells. The straightforward method of calculating the $SOC(t)$ given in equation *(2.1)* is called coulomb counting.

$$SOC(t) = SOC(t-1) + \frac{1}{Q_r}\int_{t-1}^{t}(I_{bat})dt \qquad (2.1)$$

To consider the effect of individual cell efficiency (η_{bat}), equation *(2.1)* can be rewrite as equation *(2.2).*

$$SOC(t) = SOC(t-1) + \frac{1}{Q_r}\int_{t-1}^{t}(\eta_{bat})(I_{bat})dt \qquad (2.2)$$

Another factor that might lead to imbalance is when cells have different total current $I_{tot}(t)$ from one another. It must be considered, so the total current is,

$$I_{tot}(t) = I_{bat}(t) + I_{self-dis}(t) + I_{leakage}(t) \qquad (2.3)$$

Where, $I_{bat}(t)$, $I_{leakage}(t)$, and $I_{self-dis}(t)$ are individual cell current, leakage current, and self-discharge current, respectively. So, the total current difference can lead to an imbalance during discharge process.

Numerous other factors can also contribute to cell imbalance, the long-term charge/discharge cycle will cause a decline in battery capacity and life [44]. The internal factors include chemical fluctuations, weak cell capacity, internal impedance, and non-uniform temperature stress [45]. Selecting the right cell and creating a well-designed pack helps reduce some of these causes. Nevertheless, despite all the initial design work, non-uniform internal impedance is the main cause of cell imbalance in Li-ion cells [46]. The external factors include vibration, rapid charging, and discharging. The vibration raises cell internal resistance, reduces capacity, and slightly deteriorates consistency [47]. Fast charging may result in overheating and overvoltage of the cells when a high amount of charging current is given to the battery. Similarly for discharging a sudden change in load produces a high discharge current from the battery. The cell imbalance may be induced due to both the rapid charging and discharging processes [48].

2.3.2 Battery utilisation without balancing method

Without cell balancing, battery use can have several serious negative effects. The possibility of unequal charging and discharging amongst the separate cells within the pack is a major worry [49]. In the absence of cell balancing circuit, certain cells might be used to their full capacity while other cells might not be used to their full capacity. [21].

Generally, the battery charger cuts off the power when a battery is fully charged. The battery charger detects if the battery pack has reached to its threshold and whether each cell voltage remains under an overvoltage protection limit. The weak cells connected in series are those with a lesser capacity or a larger internal resistance and show a higher voltage than the other series cells with the same capacity during charging, while weaker capacity cells have lower voltages than the other series cells during discharge. This means that when one cell voltage falls below the cell cutoff voltage limit, the BMS will stop discharging, preventing over-discharge that could harm the cell (generally, around 2.5 V for Li-ion cell [50]), and the BMS will stop charging the whole battery pack when one of the cells in series reach to its full charge state (generally around 4.2 V for li-ion cell [50]). The battery will not be used to its maximum potential because of the BMS stopping the charging or discharging process without taking the other cells into account. When any weak cell gets close to the under-voltage or over-voltage protection limit, the EV will stop using the battery as the simulation results presented in chapter 5, section 5.2.

2.3.3 Cell balancing control strategies

The balancing control strategy directly affects the cell balancing topology's performance. The most common cell balancing control strategies are based on SOC and voltage of individual cells.

2.3.3.1 Voltage-based control

The voltage of each cell in the battery pack is measured using voltage sensors. Determine the voltage difference and examine it for any imbalances in the cell voltage. Use resistors to release extra energy from the higher voltage cells or turn on an active balancing circuit to move energy from the higher voltage cell to the weaker cell [51-53]. Continue monitoring cell voltage and balancing process until the voltage differences among cells are within an acceptable range.

2.3.3.2 SOC-based control

The SOC based control required an accurate SOC estimation which is the challenging part for of this method. The SOC of individual cells is estimated using voltage and current data that continuously monitored through sensors. The voltage of each individual cell can be used to determine SOC using a straightforward open circuit voltage-based estimation technique, which measures the voltage and compare it with the SOC and voltage relation curve [54]. To estimate SOC of individual cells in real-time, more complex methods like neural networks, coulomb counting, or Kalman filters can be used [55]. The SOC based control can be used in activate cell balancing process and reduce cell imbalance in a battery pack with active balancing topologies.

2.4 Cell balancing methods

The procedure for achieving the same SOC or voltage across all series-connected battery cells, during charging, discharging, or ideal mode is known as cell balancing. Battery packs with cell balancing circuits ensure each cell is charged and discharged equally, which is essential for maximising battery pack performance and lifespan [56]. The literature [6, 7, 16, 18, 20, 40, 57-63] has presented a wide range of cell balancing approaches each of them having its unique

advantages and limitations. Active and passive cell balancing topologies are the two primary types of cells balancing topologies as presented in Figure 2.2.

The active cell balancing methods actively move energy across cells by use of switches, capacitors, and inductors and the passive cell balancing techniques use resistors or dissipative components to equalise cell voltages or SOC. The Hybrid cell balancing techniques offer a balance between cost and efficiency by combining elements of both passive and active strategies. In applications like EVs, where maintaining constant cell voltages is crucial for overall battery system efficiency, performance, longevity, and reliability, effective cell balancing techniques are essential [64].

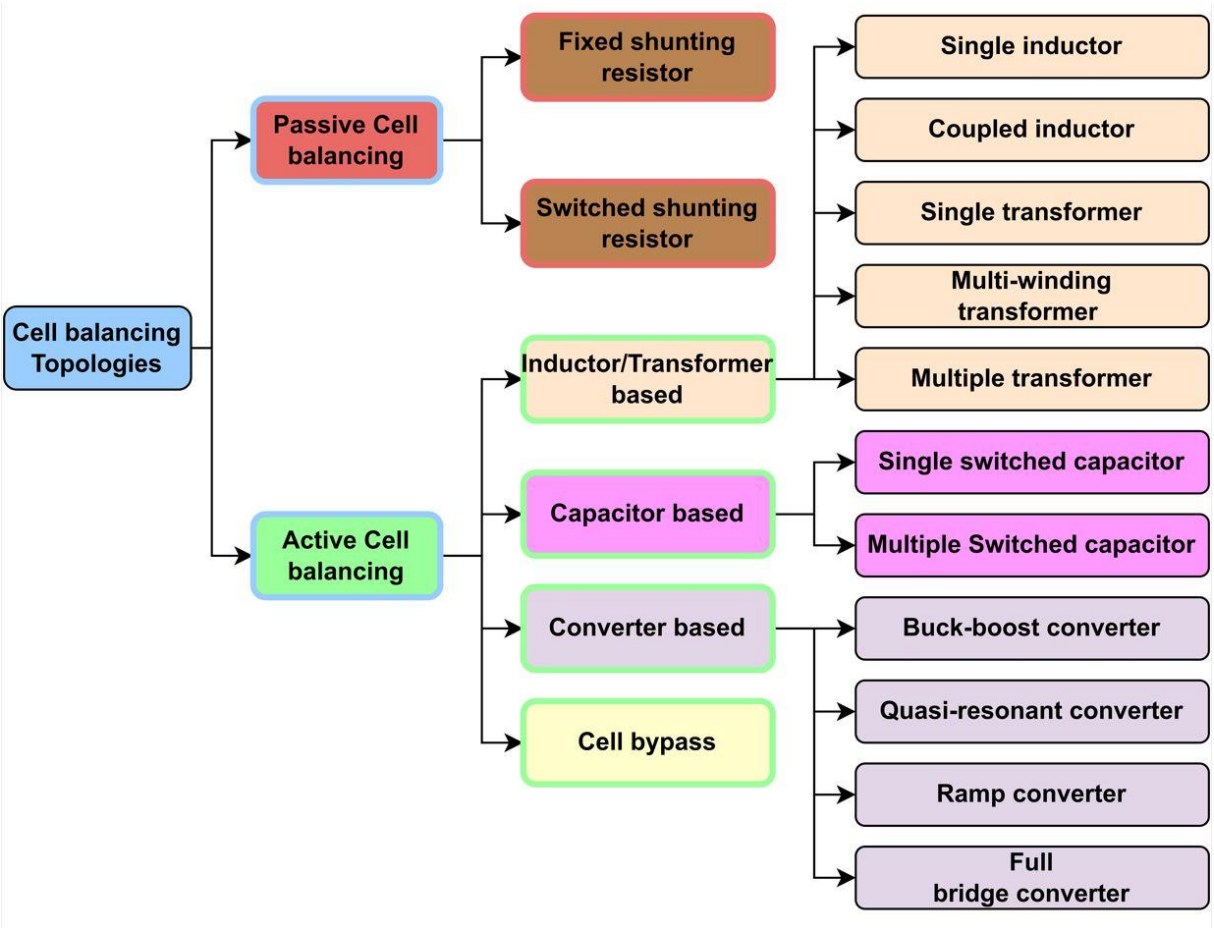

Figure 2. 2 Basic cell balancing topologies distribution, adapted from [6, 7, 16, 18, 20, 40, 57-63]

2.4.1 Passive balancing

Passive balancing involves connecting deceptive components, such as resistors, in parallel with every cell in series connected cells [3, 56, 65]. The associated resistor is triggered when one or more cells' voltage is higher than the weak cell voltage connected in series, letting extra energy escape as heat. Switch shunting resistors and fixed shunt resistors, often known as bleeding resistors, are two common types of passive cell balancing techniques. Switched shunting resistors lower the voltage of the high-energy cell by redirecting excess energy away from it. Bleeding resistors maintain cells at a stable voltage level by continuously drawing a tiny amount of current [66]. Li-ion battery packs can be balanced easily and affordably with passive cell balancing, particularly in situations where energy efficiency is not the primary concern.

2.4.1.1 Fixed shunting resistor balancing

Bleeding resistors are connected among single cells or groups of cells in a battery pack in a fixed shunting resistor cell balancing system. Higher voltage cells can gradually discharge and eventually balance with lower voltage cells due to the dissipating function of these resistors [67-69] . To avoid overcharging or over-discharging of the cell connected to the bleeding resistor, proper resistor sizing and cell voltage monitoring are crucial[52]. The fixed shunting resistor balancing topology is depicted in Figure 2.3, where each cell (*B1, B2,..., Bn*) is connected to a bleeding resistor (*R1, R2,.., Rn*).

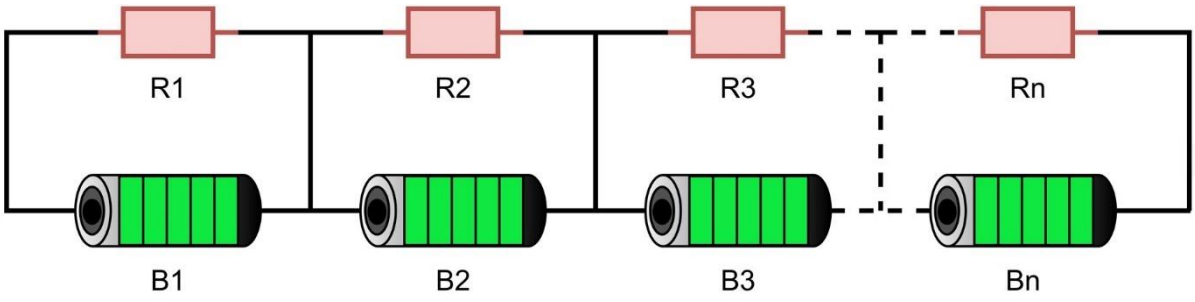

Figure 2. 3 Fixed shunting resistor diagram, adapted from [70-72]

2.4.1.2 Switched shunting resistor balancing

A slightly more effective method of passive balancing is to use switched shunting resistor cell balancing circuits for voltage balancing between cells. This technique uses shunting resistors in combination with switches [68, 73] . Every cell is connected in parallel to a shunting resistor, which is connected in series with a switch. When a particular cell's voltage surpasses the desired voltage difference with other cells in a battery pack, the associated switch becomes active. By generating a lower-resistance route, the high-voltage cell's extra energy can pass through the shunting resistor and dissipate as heat. The switch turns off when the voltage is balanced with the other cells connected in series [78]. This method reduces energy waste because the shunting resistors are only activated when balancing is required, in contrast to fixed shunting resistor approaches[74, 75]. Figure 2.4 displays a basic circuit diagram for switched shunting resistor topology. Resistors are linked in parallel with cells (*B1, B2, ..., Bn*) and series connected switches (*S1, S2, ..., Sn*) with shunting resistors (*R1, R2, ..., Rn*). The control algorithm for switches in the switched shunting resistor cell balancing topology can be implemented in a way to monitor all the cell voltages and only turn on the specific switch connected with the higher voltage cell to dissipate energy through a resistor.

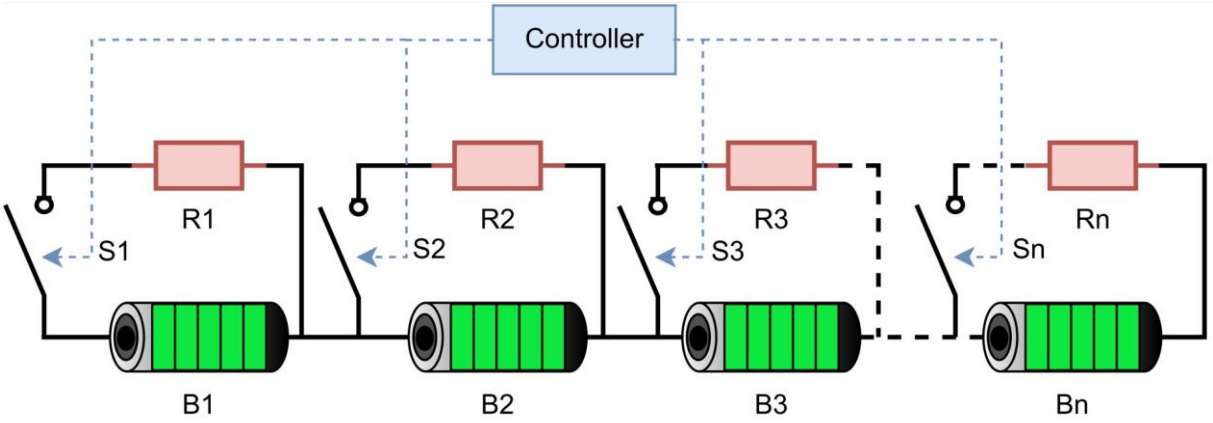

Figure 2. 4 Switched shunting resistor diagram, adapted from [70-72]

2.4.2 Active balancing

Active cell balancing is an important part of an advanced BMS that ensures the optimal performance and longevity of rechargeable batteries, especially in applications like EVs and renewable energy storage systems [55, 71]. Active balancing actively redistributes energy among the individual cells in a battery pack as opposed to passive balancing, which releases extra energy as heat. This process assists in achieving SOC, or voltage balance, for each cell, guarantees optimal battery capacity utilisation, and avoids excessive charging or discharging of any single cell within the pack. Active balancing improves the battery pack's overall capacity, energy efficiency, and safety by ensuring balanced voltage or SOC throughout the individual cells [38, 76-87].

The four main types of active cell balancing topologies are bypass [88-92], converter-based [35, 82, 83, 93-103], inductor/transformer-based [80, 81, 104-111], and capacitor-based [112-124]. Using transformers or balancing capacitors, energy is moved from a high-voltage cell to a low-voltage cell during the cell balancing process. Another way to balance the battery voltage is to use converters to move excess energy from a high-voltage cell to a low-voltage cell. The bypass balancing operates distinctly from the other active cell balancing techniques. To achieve cell balance, the controller logic of this topology, bypass the charging or discharging current, rather than transferring energy from a higher voltage to a lower voltage cell.

2.4.2.1 Single inductor-based balancing

A method of active cell balancing that uses just one inductor to balance each cell in a battery pack [110, 111]. In this approach, a single inductor is connected to various cells using the switching network, usually made up of MOSFETs. The voltage levels of individual cells are supervised by a control circuit using microcontrollers. The switching network links the inductor

to the high-voltage cell which needs to be balanced, the energy from that cell is temporarily stored in the inductor. The stored energy is then transferred to the lower-voltage cell by means of switches connecting the inductor to that cell. During the cell balancing process, energy is continuously transferred, bringing the voltage or SOC difference between the two cells into balance. A single inductor reduces the voltage, size, weight, and cost, which makes it a desirable option for several applications particularly EVs and portable devices [125]. However, the design of an adaptive control algorithm is essential for the better performance of a single inductor active cell balancing. Additionally, compared to a coupled inductor, balancing takes longer because it can only balance one cell at a time [78].

The single inductor (L) active cell balancing is shown in Figure 2.5. The switching network (*S1, S2,..., Sn*), with antiparallel diodes, relates to the individual cells (*B1, B2,..., Bn*). This method is especially helpful in situations where weight, and space are limited, as it required few components compared to coupled inductor balancing method.

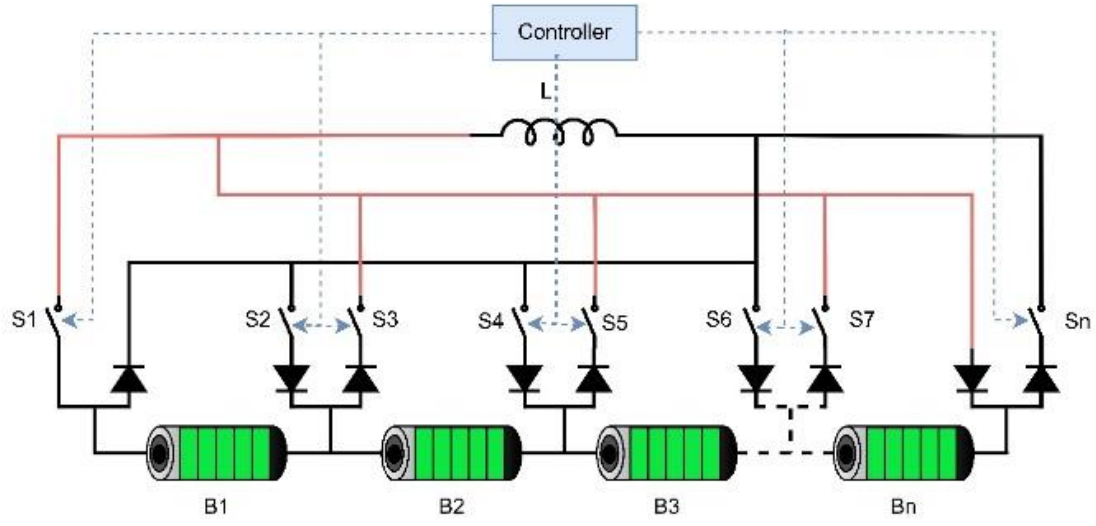

Figure 2. 5 Single inductor cell balancing topology, adapted from [70-72]

2.4.2.2 Coupled inductor balancing

Instead of using a single inductor for each cell, the coupled inductor cell balancing approach uses many inductors. It uses magnetic coupling between the inductors to facilitate energy transfer across multiple cells at a time [78]. When one of the two cells needs to be balanced, the high-voltage cell, which is connected to a common inductor between them, sends energy to the low-voltage cell. The coupled inductor method simultaneously transfers the energy between multiple cells in a series of cells [126]. Rapid energy transfer is made possible by the coupled inductor design as compared with the single inductor method [101].

Figure 2.6 shows the basic coupled inductor cell balancing topology in which two cells (*B1*, *B2*) are connected to a coupled inductor (*L1*) via switches (*S1*, *S2*). Inductor *L1* is used to transmit energy between *B1* and *B2* to achieve cell balancing. Similarly, *L2* is responsible for doing the cell balancing between *B2* and *B3*, and so on.

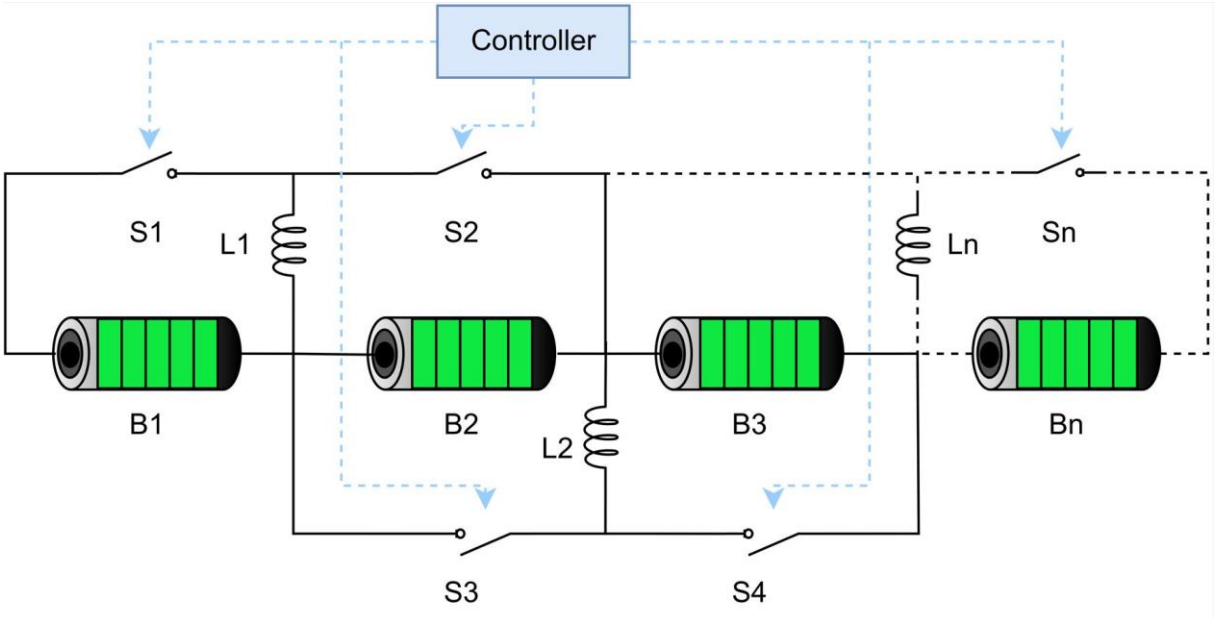

Figure 2. 6 Coupled inductor cell balancing topology, adapted from [70-72]

2.4.2.3 Single capacitor balancing

The single capacitor cell balancing circuit uses a single capacitor that can connect with each cell through switches. One capacitor and a group of switches, usually MOSFETs are used in this cell balancing technique. Sensors consistently monitor the voltages of all cells, initiating the cell balancing procedure when the voltage variance among two or more cells exceeds a specified threshold [112-114]. In the first cycle, the corresponding switch is activated to enable the connection between the high-voltage cell and the capacitor, to charge the capacitor. In the second cycle, the capacitor's stored energy is discharged back into the undercharged or low-voltage cell, and that brings the high-voltage cell back to equilibrium. The advantage of using a single capacitor cell balancing technique is the use of a single capacitor instead of numerous capacitors, lowers the cost and complexity of the circuit. Since it can only balance one cell at a time, the balancing speed could be slower than with multiple switch capacitor cell balancing procedures [120]. A single capacitor balancing method is illustrated in Figure 2.7, a single capacitor (*C*) is connected with a series resistor (ESR) and the two layers of the switching network (*S1, S2,..., Sn)* build a connection between a capacitor and the battery cells (*B1, B2,..., Bn*).

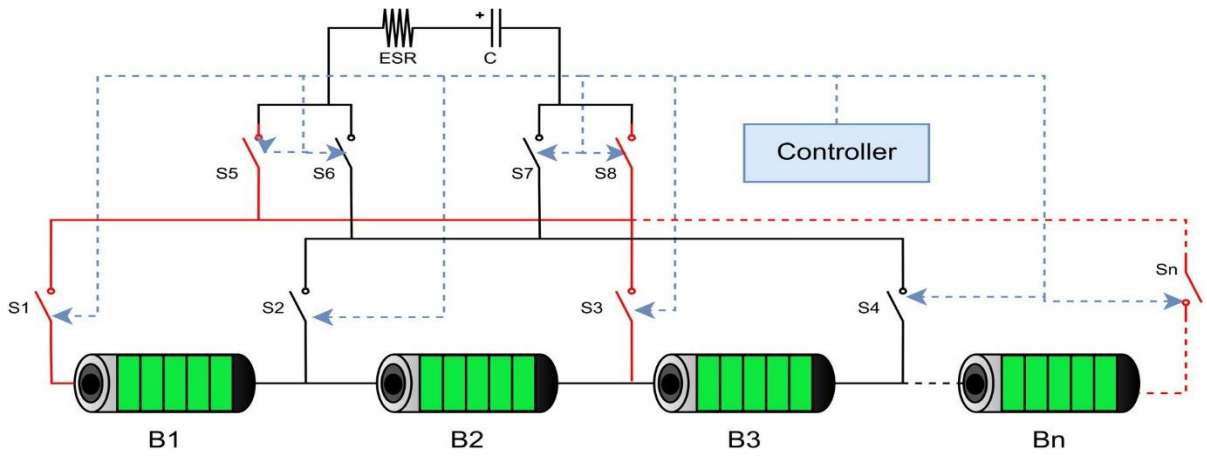

Figure 2. 7 Single capacitor cell balancing topology, adapted from [70-72]

2.4.2.4 Multiple Switched capacitor balancing

Multiple Switched capacitor cell balancing circuits can be used to equalize the voltages or SOC between cells. The switched capacitors can be connected to the battery cell in a different combination. The popular, multiple-switched capacitor cell balancing techniques are double-tired switched capacitor [118, 124] and single-tire switched capacitor cell balancing [113, 117, 119, 122]. In the single tier capacitor cell balancing technique multiple cells can be balanced during the balancing process by using a layer of capacitors. High-voltage cells transfer their energy to a layer of capacitors, which then transfer it to low-voltage cells during the cell balancing process to perform simultaneous energy transfer [122]. Figure 2.8 shows the single tier capacitor cell balancing method, in which series connected capacitors build a layer of capacitors (*C1, C2,.., Cn-1*). The layer of the capacitor is then connected with the battery cells (*B1, B2,..., Bn*) through a switching layer (*S1, S2,..., S2n*). A single capacitor (*C1*) relates to a pair of battery cells (*B1, B2*) through two switches (*S1, S2*).

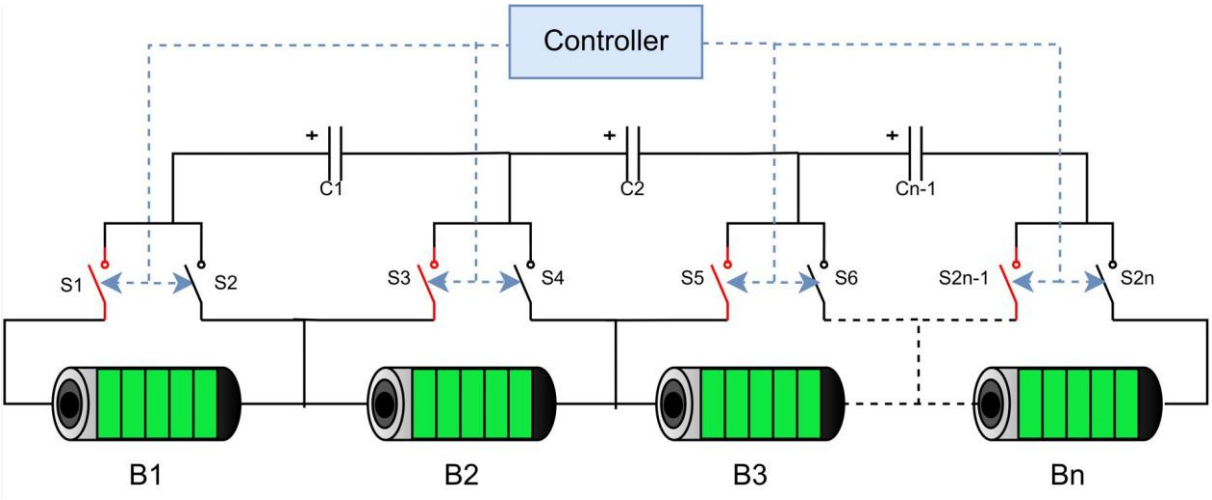

Figure 2. 8 Multiple switched capacitor cell balancing topology, adapted from [70-72]

Compared to multi-tiered balancing circuits, the single tier capacitor method uses a single layer of switches and capacitors, which simplifies the design and lowers overall complexity and

expense. Cell balancing can also be accomplished with double layers or other novel combinations of capacitors. However, it has the disadvantage of having more capacitors, which raises the cost and increases the size of the balancing circuit.

2.4.3 Bypass balancing

According to the bypass cell balancing topology depicted in Figure 2.9, each battery pack cell or module is connected to two switches [90-92]. One that bypasses the cell, while the other establishes connections between the cells in series within a battery pack. Cell balancing is accomplished by using these switches to regulate the current flow [127]. This method has simple structure and straightforward control, as the switches are controlled according to the cell voltage or SOC during balancing procedure. This method can perform cell balancing process during charging or discharging mode of operation of the battery pack but cannot perform cell balancing during static mode, as it depends on the charging and discharging current. The working principle of this method is to bypass the higher voltage cell during charging mode, while lower voltage cell is bypassed during discharging mode. The bypass balancing method is further discussed in the section 2.8 and 2.9.

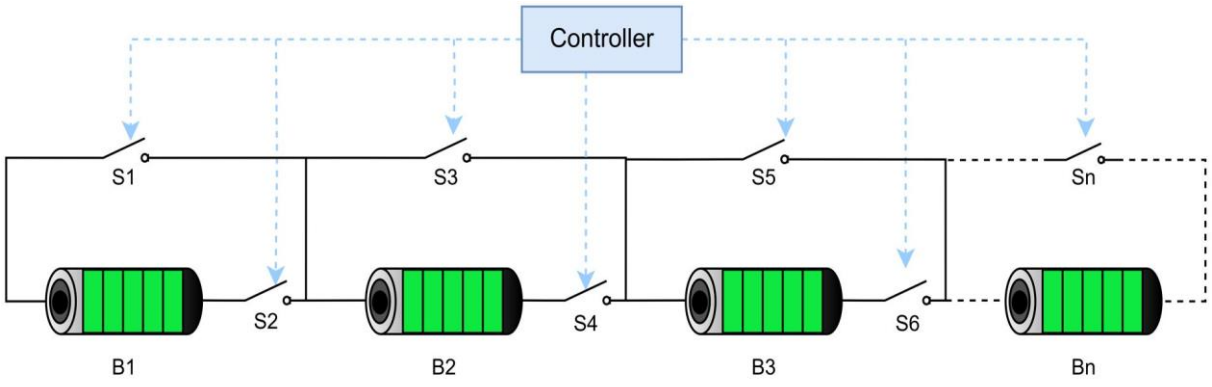

Figure 2. 9 Bypass cell balancing topology, adapted from [90-92]

2.5 Energy transfer in active balancing

Cell balancing circuits use a variety of energy transfer strategies to maintain the voltage or SOC levels of each individual cell in a battery pack. In cell balancing, the primary forms of energy transfer techniques are categorised into four groups. Direct energy transmission between individual cells within a battery pack is known as C2C energy transfer. In balancing process with C2C method, until the voltage or SOC are not matched, energy is transmitted from the overcharged to the undercharged cell. The C2P method transfers energy between individual cells and a battery pack. To balance the cells, the higher voltage cell energy is transferred to battery pack then from pack to the lower voltage cell. P2C method operates in the opposite way as the C2P energy transfer method, in which individual cells receive energy from the battery pack. The pack transfer the energy to an undercharged cell and raises its voltage to bring it into voltage equilibrium with the other cells. A more complex method of energy transfer in two steps is the C2P2C method. During balancing, the energy is initially moved from the strong cell to the pack, then transferred from the pack to the weaker cell that need to be balanced. Comparison of cell balancing topologies [70-72, 128].

2.6 Comparison of cell balancing topologies

Simple and affordable passive balancing methods include diodes and shunting resistors. The passive balancing topologies are less energy-efficient because of heat dissipation, but it is suitable for applications with low power requirements and a few numbers of cells connected in series. Conversely, active balancing techniques use inductors, capacitors, transformers, and converters, with switches to actively move energy across cells. These methods are better than passive balancing because it can reduce energy loss, which makes them appropriate for high-power applications and many series-connected cells. By combining aspects of passive and

active techniques, hybrid cell balancing solutions compromise between complexity and efficiency. Resonant circuits are another tool used in cell balancing approaches to maximise the efficiency of energy transfer by reducing power loss. Topology selection for cell balancing is influenced by various aspects such as power limitations, system complexity, and financial restraints. Table 2.2 gives a comparison between cell balancing topologies in terms of number of components and energy transfer methods.

Table 2. 2 Number of components utilized in various topologies for cell balancing

Ref	**Cell balancing types**	**Number of components**						**Energy transfer method**
		R	L	T	C	D	S	
	Passive							
[65]	Fixed shunting resistor	n	0	0	0	0	0	cell to heat
[65]	Switched shunting resistor	n	0	0	0	0	n	cell to heat
	Active							
[125]	Single inductor	0	1	0	0	2n+2	2n+2	P2C, C2P, C2P2C
[126]	Coupled inductor	0	n-1	0	0	0	2n-2	C2C
[129]	Single transformer	0	0	1	0	1	2n+2	P2C, C2P, C2P2C
[79]	Multi winding transformer	0	0	1	0	n	n+1	C2P, P2C, C2P2C
[130]	Multiple transformers	0	0	0	0	n	n	C2P, P2C, C2P2C
[118]	Single switched capacitor	1	0	0	1	0	n+5	C2P, P2C, C2C, C2P2C
[118]	Multiple switched capacitor	n-1	0	0	n-1	0	2n	C2C
[85]	Buck-boost converter	0	n	0	n	0	2n	C2C
[103]	Quasi-resonant converter	0	2n-2	0	n-1	0	2n-2	C2C
[131]	Ramp converter	0	0	1	n	n	n	C2C
[96]	Full bridge converter	0	0	0	n	0	4n	C2C
[89]	Bypass	0	0	0	0	0	2n	no energy transfer

R: number of resistors, L: number of inductors, T: number of transformers, C: number of capacitors, D: number of diodes, S: number of switches, n= number of cells.

2.7 Latest trends and optimisation of cell balancing topologies

Table 2.3 presents a summary and optimisation of recent developments in cell balancing approaches. The basic circuit topology, optimised results, and important parameters has been mentioned in the Table 2.3. Every method described in the literature tested with varying conditions, cell characteristics, and switches power levels. Convert the initial and final voltages to obtain the approximate values in percentage by using li-ion cell nominal voltage is (typically 3.7V) for comparing cell balancing topologies. If the quantity of switches or relays is considered as a cost of the balancing topology, the techniques described in [126] and [124] are the ones that use a single switch per cell are cheaper than other topologies. Since all the available data were measured or assessed with different starting imbalances, charging current, and battery capacity, it was difficult to compare the balancing speed. However, an indicative balancing time is calculated by using the capacity and balancing current information. In this case, it appears that the approach described in [124] produced the smallest indicative time, which is 31.4 minutes. However, by raising the balancing currents, the balancing speed can be improved. To observe the power loss comparison in terms of number of switches, and regardless of other factors the method reported in [124] and [126] give lower losses due to less number of switches.

Table 2. 3 Recent advancements and optimizations of cell balancing techniques.

Ref	Type	Type of Method	Initial imbalance (%)	Final imbalance (%)	Per cell capacity (Ah)	Balancing current (A)	Indicative cell balancing time (minutes)	No. of Switches	Control method	Comments
[119]	Switched capacitor	Close loop switched capacitor equaliser	34.8 V	2.9 V	2.6	1.72	90.7	2N	SOC	the cell balancing process is explained by simulation findings, the experimental results simply display the final residual difference between cells. connect the first and last cell with an additional capacitor.
[116]	Switched capacitor	Parallel resonant	8.1 V	0.01 V	1.1	0.4	165	4N	Voltage	It eliminates the inrush current and provides a three times faster cell balancing speed than the standard PSC

		switched capacitor equaliser								equalizer. However, the expense is more than that of traditional PSC balancers.
[132]	Inductor based	Single Inductor bidirectional cell balancing	6.3 V	0.5 V	20	0.8	1500	4N+4	Voltage	This study used many cell balancing paths to attain fast balancing speed. However, there are some disadvantages to this method, such as loop resistances and losses on bypassed circuits.
[126]	Inductor based	Coupled inductor cell balancing	24.2 V	0	NA	2	NA	N	Voltage	For static balance, use simulation; for charge balancing, use experimentation. The process takes only 6 seconds since it employs inductor voltage rather than battery cells to demonstrate cell balancing. In comparison to the conventional linked inductor topology, each cell pair requires one fewer switch.
[111]	Inductor based	Single inductor cell balancing with an auxiliary battery	30.2 SOC	0	12.8	6.4	120	2N+3	SOC	The choice of the control variable is the average SOC and using an additional battery to perform cell balancing process.
[133]	Inductor based	Double-layer inductive Equalisation Circuit with a resistor in parallel with each inductor	25 SOC	0	NA	7	NA	N+N/2	SOC	The superior performance of the suggested system is demonstrated by comparing the outcomes with a single layer and with a dual-layer inductor topology. The 0.5c, 1c, and 2c rates current for charging and discharging were also evaluated. However, the charging results are not displayed in the paper.
[124]	Capacitor and inductor based	Advanced Switched capacitor equaliser circuit	19.8 V	0	2	3.82	31.4	N	Voltage	Implemented a hybrid balancing method combining Switched capacitor and buck-boost converter and considers the impact of parasitic resistance of the magnetic components.
[134]	Converter based	Push-pull converter-based cell Balancing Circuit	6.7 V	0	NA	1.5	NA	4, 2N relays	Voltage	It performed cell balancing through C2C method using an isolated Push-Pull converter. The converter switches' duty cycle is adjusted to 50% to minimize ripples in voltage and current.
[86]	Converter based	Dual DC-DC converter-based cell balancing with an auxiliary battery	20 SOC	1 SOC	NA	4	NA	2N+5	SOC and Voltage	The auxiliary battery connected to the inductor by switches forms a buck converter, while the inductor and associated switches build a flyback converter. When charging, the flyback converter maintains C2P balance, and when discharging, the buck converter charges the auxiliary battery through regenerative braking. Make use of both voltage-based and SOC control.

[98]	Resonant converter	Single resonant converter balancing Circuit with reduced resonant frequency	5.4 V	0	4.2	1	252	4(N-1)	Voltage	A single resonant converter with reduced resonant frequency is used to improve balancing time and reduce power losses as compared with independent resonant tank topology. The proposed topology is also tested for supercapacitor and lead-acid battery cell balancing other than lithium-ion cells gives promising results.

N: number of cells, NA: not available

2.8 Overview of bypass balancing method

There are few research studies available on bypass cell balancing in the literature. The first battery cell bypass topology patent (US5898291A, United States) was published in the literature by John C. Hall Space Systems Loral LLC in 1999 [135]. When a battery cell fails in a series of connected cells, human intervention is not possible to fix the issue, specifically with li-ion batteries. A mechanism was offered to maximise the battery energy storage capacity. Electrical connections are made in series between at least two cell strings, each of which has several battery cells in parallel. The fact that a failed cell in one series string of battery cells in an array of li-ion batteries in a series-parallel configuration unfavourably lowers the permitted charging voltage of the remaining series strings of the array and consequently lowers their capacity is a crucial factor to consider. By eliminating cells from every series string in the array, this invention prevents such an unwanted outcome. The patent explains that the bypass topology was used to detect faulty cells in a battery pack to bypass but does not consider adaptive control to perform cell balancing.

The author of [136] added an extra cell to the battery pack to allow one cell to be bypassed during the charging or discharging process. Although this topology is named "lossless cell balancing," but it did not consider switching matrix power loss. However, the control algorithm is very straightforward, bypassing the cell for a set period rather than using an intelligent control to make decisions based on soc/voltage measurements of individual cells and perform cell

balancing. The paper reports on the enhancement in the capacity of the cells with rest periods but does not address its effect on cell balancing.

The paper [90] presents the bypass approach for introducing a bypass cell balancing topology for EVs. Each battery cell relates to half-bridge switches, which enables cell balancing according to the SOC. However, for verification of the balancing topology, only consider a very modest initial SOC imbalance of 1% and cell balancing is tested in simulation for a low charge current of about 0.2c. The simulation results for discharging do not validate the cell balancing, as it does not show a clear difference in the starting and ultimate residual SOC imbalance between cells.

The paper [91] explains the idea behind a Smart Battery Pack (SBP) using bypass balancing topology. The balancing control is based on SOC to bypass the specific cell. The paper is more focused on wireless communication to send and receive commands. However, the SOC is measured from hardware in the loop simulator and the cell balancing does not consider the worst conditions for initial SOC imbalance.

The combination of bypass and passive balancing is demonstrated in [137]. The control software will determine which topology operates at any given time. However, according to this paper, the limitation of bypass cell balancing topology implementation is the manual adjustment of the charger supply voltage.

The article [92] discusses a short circuit (bypass) topology, including SOC as a balancing control variable. Relays are employed as a switching mechanism to either connect the cell in series or bypass it. To provide the necessary power, EVs use a range of series and parallel combinations of Li-ion batteries. Because of this, this architecture needed 2N relays for

every N series-connected cell, making the balancing circuit large and may be unsuitable for EVs.

The most recent work in [89] proposes a double-layer equalization method for battery packs, including DC-DC converters and bypass cell balancing topology. The outside layer uses a buck-boost converter, while the inner layer uses a reconfigurable (bypass) architecture. The buck-boost converter is connected to the cell or module to stabilise the total output voltage of a specific module, and the bypass topology is utilised to establish balance across cells inside the module for cell balancing. However, the article describes that accurate SOC estimation is challenging, so it uses SOC measurement from the battery Simulink model rather than designing an algorithm for accurate SOC estimation. Additionally, the output voltage individual module will be stabilised by using a separate converter, but the cell balancing circuit will be more bulky and costly. The use of a power converter will also add additional losses.

2.9 Utilisation of DC-DC Converters in EV

In the EV's powertrain system, there are three different kinds of power converters, DC-DC, DC-AC, and AC-DC. DC-AC converters were needed to convert the DC voltage to AC for the induction motor drive. To charge the battery pack during regenerative braking, EVs require AC-DC converters to convert AC power to DC. DC-DC converters are employed to supply reduced power to components with lower power ratings and to supply variable DC-link voltage to the traction inverter [138]. Mostly induction motor drives that use voltage source inverters run on a fixed, high-voltage DC connection. Nevertheless, using a high DC-link voltage at low drive speeds will cause the inverter to have a low modulation index, which will result in inefficient DC bus usage [139].

The utilization of a variable DC link in traction inverters for EVs offers distinct advantages over fixed DC link configurations. The main drawback of using a fixed DC-link for traction inverter is high power losses, due to high voltage supply at lower speed. A variable DC-link voltage capable of adapting to various speed conditions is more preferred for minimising overall traction losses. In the real world, the driving speed of the vehicle is always varying. The DC-link voltage can be raised to supply the appropriate power in circumstances requiring high power, such as when accelerating or climbing hills. Conversely, during periods of reduced power demand, such as cruising or deceleration, the DC-link voltage can be lowered for minimising traction inverter power losses and improving overall power efficiency. The advantages of employing variable DC-link voltage over fixed DC-link voltage are demonstrated by several research publications on variable DC-link voltage optimisation for traction inverters [88, 139-143]. However, mostly the DC-DC converters are used in hybrid or plug-in hybrid EVs [144] where the primacy concern is battery charging during regenerative braking system. The article [145] also introduce DC-DC converter in Ev but the focus of the research is to reduce the THD with different modulation techniques and the results analysis shows that the variable DC-link can reduce the THD and increase the efficiency of traction inverter.

In EVs, the researchers [146, 147] proposed a variable DC-link voltage by substituting the DC-DC converter between the battery pack and the traction inverter. However, the drawback of using a DC-DC converter will also produce power losses and most importantly, the EV will require extra balancing circuit as this cannot deal with the cell imbalance of the EV battery pack. Nevertheless, because the DC-DC converters rely on input voltage, duty cycle, and load characteristics, designing DC-DC converters appropriately might be difficult. Furthermore, because of the switching operations, DC-DC converters show non-linear behaviour and slightly damped dynamics [61].

2.10 Research gaps in cell balancing topologies

After a thorough investigation of the current cell balancing topologies in literature, the following important points have been identified that need to be considered for optimisation.

1. Although designing a SOC-based controller for cell balancing is simple. However, estimating SOC accurately is one of the most challenging parts of BMS. Coulomb-Counting is a simple method of SOC estimation, which requires the cell's initial SOC information as well as the current over time. However, in practice the current contains noise and variations, which make it challenging for accurate SOC estimation.
2. Another method is to utilise a voltage-based controller. Measuring voltage is simple, but in practice, it is also difficult because of electromagnetic noise and fluctuation in voltage, which must be considered.
3. When using a bypass cell balancing topology during charging, the charger and BMS need to have an adaptive control system that the charger can modify the supply voltage according to bypass number of modules in real-time.
4. The necessary DC voltage must be determined in proportion to the speed of the induction motor to carry out SOC/voltage balancing while providing sufficient power to the vehicle during discharging.
5. The selection of electronic components to design cell balancing circuit, especially for EV applications needs to be lightweight, and small, and volume so that it is applicable in practice.
6. To assess the overall efficiency of balancing circuit, it is important to analyse and compute the power loss related to the traction inverter and balancing circuit.

2.11 Research gaps optimisation

The above-mentioned research gaps in cell balancing topologies are tackled through the proposed state of the art system.

1. Instead of using SOC as a control variable, the voltage is used. The balancing results in chapter 5 shown a good relationship between SOC and voltage of li-ion cell.
2. The voltage-based control method used for charging and discharging of battery pack, which is further describe in chapter 4, section 4.2.1. The voltage fluctuation is reduced by moving average filter as shown in chapter 6, section 6.3 and 6.5.
3. To achieve adaptive control for a DC fast charger, CCCV charger is designed in chapter 3, section 3.4 and the results in chapter 5, section 5.3 provide the verification of adjustment of charger supply voltage.
4. The relationship between the voltage requirement and motor speed is determined by FOC and presented in chapter 3, section 3.6.7.
5. The component selection of the state-of-the-art system is according to the power rating required for charging and discharging circuit. The selection of electronics components is explained in chapter 5, section 5.5 and 5.8. The power losses are calculated and compared in chapter 5, section 5.7 and 5.8.

In the summary of this chapter, several cell balancing techniques has been discussed and focused on bypass balancing method. Review the existing literature on cell balancing topologies to find the research gaps and briefly explain the ways of resolving these gaps through proposed state of the art system. The literature also verifies the advantages of using variable DC-link over fixed DC-link for traction inverter. The following chapter will introduce the development of battery cell and motor approximate models.

Chapter 3: Battery and Induction Motor Modelling

This chapter describes the three-phase induction motor and battery cell model approximation. These models are used to test the proposed method and controller using simulation software before applying on physical models or implementation in HIL. The Panasonic Li-ion cell (NCR18650B) parameters are used to modify the default MATLAB Simulink model of the Li-ion cell and use actual induction motor parameters to estimate the induction motor per phase equivalent circuit parameters. This chapter also explains the operating principle of the battery charge controller and FOC.

3.1 Battery cell modelling

The MATLAB Simulink general battery cell model presents four different battery types, nickel-cadmium, lead-acid, nickel-metal-hydride, and lithium-ion. It allows users to modify several parameters, including the nominal voltage, rated capacity, initial state of charge, and discharging parameters. Figure 3.1 and 3.2 displays the block diagram and MATLAB Simulink diagram of the li-ion battery cell, receptively. Figure 3.2(a) represent a general block diagram with controlled voltage source and internal resistance. The mathematical model a cell is presented in Figure 3.2(b).

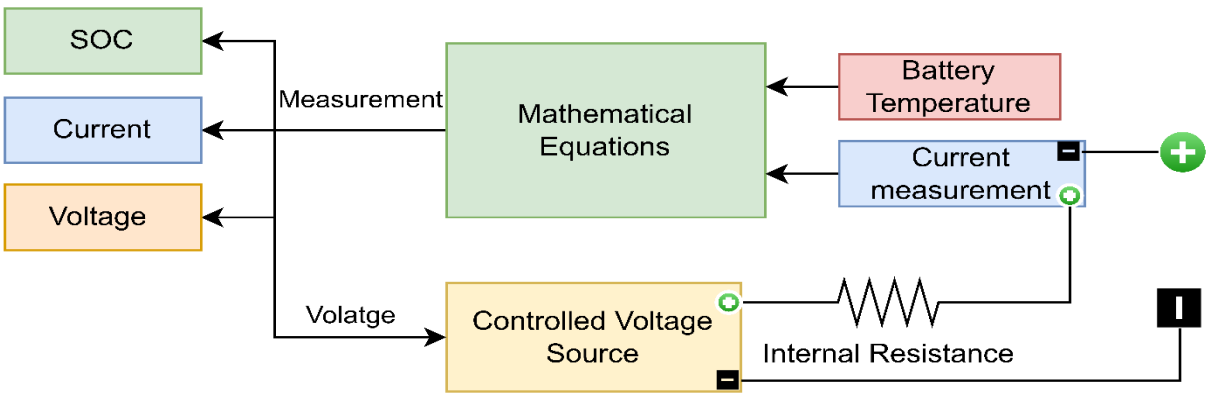

Figure 3. 1 Generic li-ion battery cell block diagram

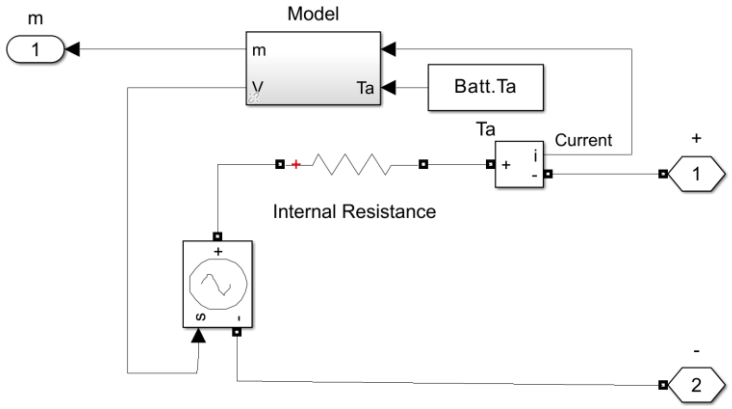

(a)

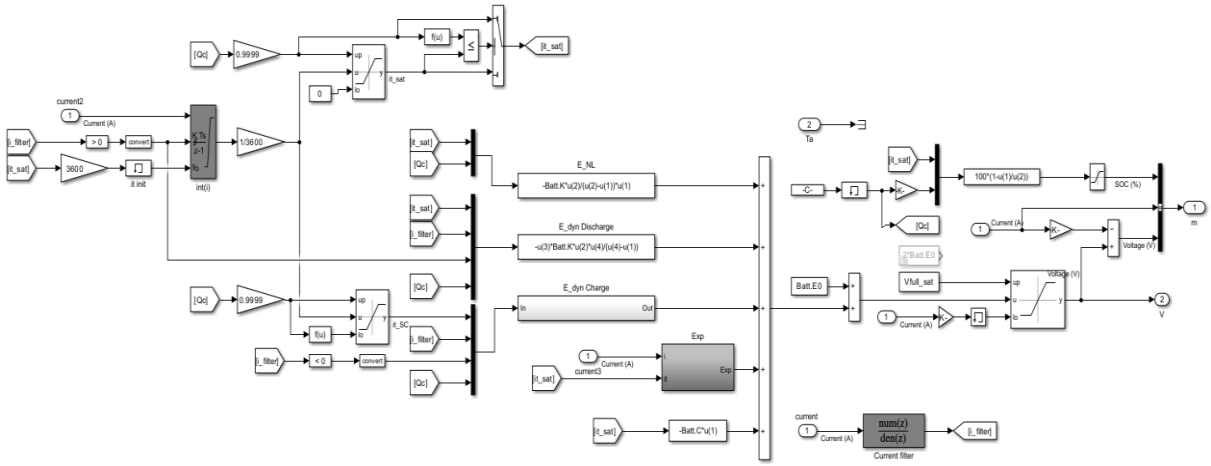

(b)

Figure 3. 2 Generic li-ion battery cell MATLAB Simulink model

Battery temperature and current signals are required for the battery cell mathematical model. The model measuring port allows for the measurement of voltage, current, and SOC. The cell voltage in the model is provided by a controlled voltage source. In this research voltage-based controller is used for controller design and SOC is measured directly from the battery cell model. Although temperature management is important but its more related to mechanical issue, so this research is mainly focused on electrical aspects of the BMS.

The Simulink battery model has some limitations and assumptions [148].

3.1.1 Limitations

1. The fully discharged cell minimum voltage with no-load is zero (0 V) but the real Li-ion cell voltage should not be less than it's cut off limit, otherwise the cell will be damaged permanently.
2. The fully discharged cell minimum capacity is zero (0 Ah), however, the real Li-ion cell have some residual capacity but may not be able to store or transfer energy.
3. The initial voltage is zero, but the voltage is stabilised within 0.1 seconds.

3.1.2 Assumptions

1. The internal resistance is constant and independent of the current.
2. The discharge parameters are used to determine the model and assume the charging characteristics are the same as and discharging.
3. The battery capacity remains constant regardless of the current amplitude.
4. There is no representation of the battery self-discharge.

3.2 Modification in the default MATLAB Li-ion cell model

The proposed method can be applied on any type of li-ion cell, but choice is made due to availability of the cell in the market. the automotive battery pack data is very confidential and not available for everyone but the data sheet of NCR18650B li-ion cell is available, and it can be used to modify the MATLAB Simulink model. The Panasonic li-ion cell (NCR18650B) was chosen with rated capacity of 3.25 Ah to make high power battery pack, instead of default MATLAB Simulink Li-ion cell model (CGR18650AF) with a rated capacity of 2.05 Ah. The parameters extracted from the datasheet of NCR18650B [50], and adjusted to get approximate charge and discharged characteristics of the cell to develop a practical cell model are reported in Table 3.1.

Table 3. 1 Li-ion cell parameters (NCR18650B)

Parameters	**Value**	**Units**
Nominal voltage	3	V
Rated capacity	3.25	Ah
Initial state-of-charge	0-100	%
Maximum capacity	3.25	Ah
Cut-off Voltage	2.5	V
Fully charged voltage	4.2	V
Nominal discharge current	3.25	A
Internal resistance	0.001	Ω
Capacity at nominal voltage	3	Ah
Exponential zone Voltage	3.95	V
Exponential zone Capacity	0.1	Ah

Both Figure 3.3 and Figure 3.4 are closely matched, which depict the expected discharge curves produced by altering the discharge parameters in the battery cell model and the datasheet discharge curves, respectively.

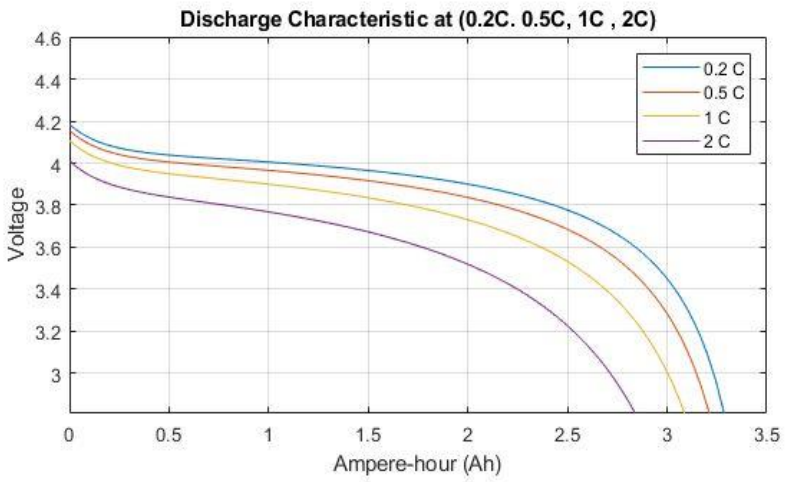

Figure 3. 3 li-ion cell discharge characteristics at (0.2C, 0.5C, 1C, 2C) from MATLAB Simulink

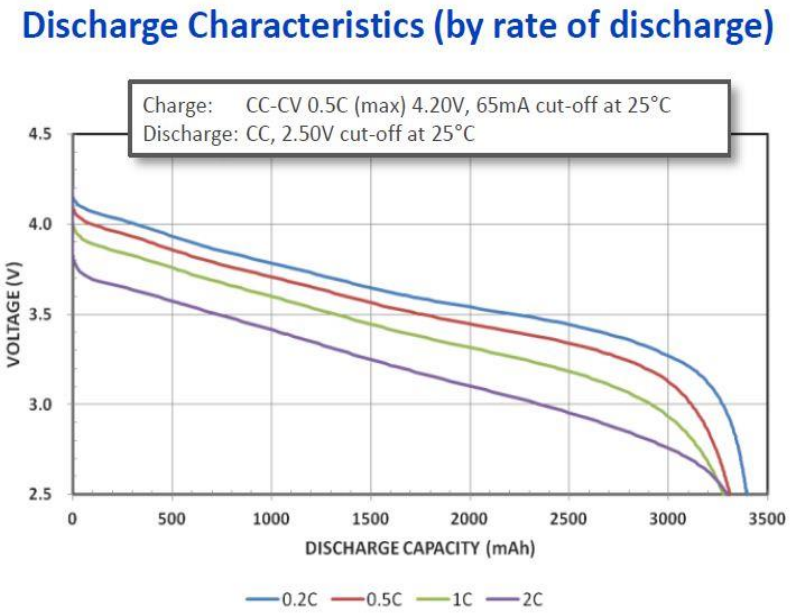

Figure 3. 4 li-ion cell discharge characteristics from datasheet [50]

Before creating the EV battery pack, a single li-ion cell model is put through a constant current constant voltage (CCCV) charging test. There is a good match between the simulation results and the data sheet charge characteristics, illustrated in Figure 3.5 and Figure 3.6, respectively.

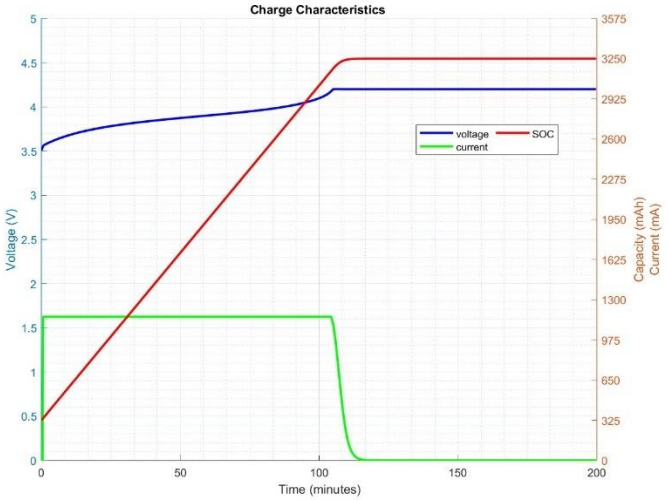

Figure 3. 5 CCCV charge characteristics of the li-ion cell at 0.5C-rate from MATLAB Simulink

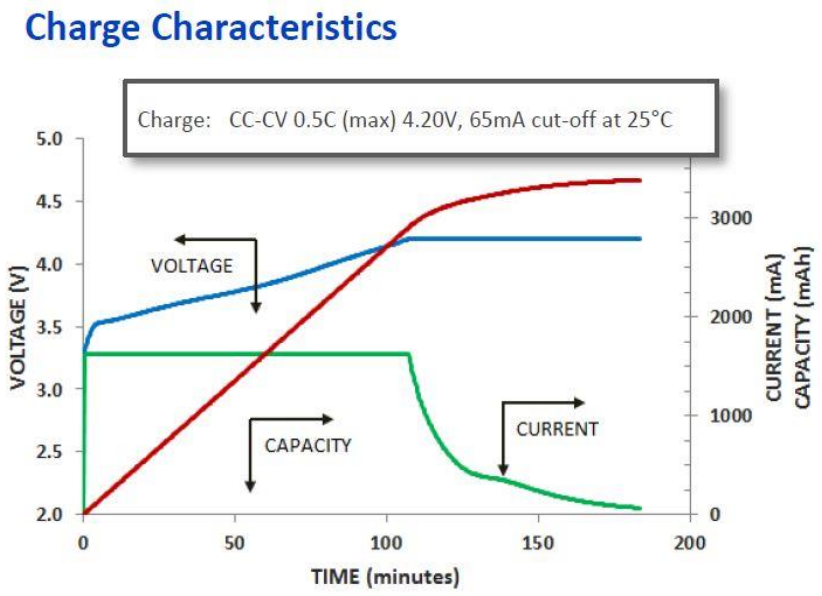

Figure 3. 6 CCCV charge characteristics of the li-ion cell at 0.5C-rate, from the datasheet [50]

3.3 CCCV charger

CCCV charging is a general method for charging li-ion batteries utilised by EVs. By optimising the charging procedure, this technique provides effective and secure charging. The CC phase and the CV phase are the two primary stages of the CCCV charging process. The controller design and working principle of CCCV charger is further explained in the next section 3.4. The battery receives a constant current during the CC phase of charging. The CC phase objective is to rapidly charge the battery up to a predetermined SOC level then change to CV phase to protect the battery from overcharge. The battery voltage consistently rises throughout CC stage. When the li-ion cell reaches its fully charged voltage (typically 4.2V), the charger switches to the CV phase and the charging current starts to decrease, while the voltage stays constant. For battery safety and health, the change from the CC to the CV phase is essential. Overcharging or allowing a lithium battery to reach dangerously high voltages can cause overheating, capacity loss, and potential safety risks. The CCCV charging algorithm switches to the CV phase to finish the charge more gradually and prevent overcharging after allowing for a quick charge in

the CC phase, which is advantageous for rapidly refilling the battery. The dynamic adjustment of charging parameters depending on several elements like battery temperature, SOC, and cell condition is a significant feature found in modern EV chargers and BMS. This guarantees that the charging procedure and surrounding circumstances, are customised to the battery hence enhancing the battery's longevity and safety.

3.4 Battery charge controller

The proposed bypass topology's battery pack output voltage is determined by the quantity of bypassed and serially linked modules. Under static conditions, the battery pack's maximum output voltage ($V_{\max\ \_out}$)) is equal to the total of the voltages of all the modules that are linked in series. On the other hand, the battery pack output voltage (V_{out}) during cell balancing is equal to the sum of the bypass cell voltages (V_k) subtracted from the sum of the voltages of the individual cells (V_i).

$$V_{\max\ \_out} = \sum_{i=1}^{n} (V_i\ ) \tag{3.1}$$

$$V_{out} = \sum_{i=1}^{n} V_i - \sum_{k=1}^{m} V_k \tag{3.2}$$

Where n is number of modules and m is the number of bypass modules.

When the battery pack nearly reaches its maximum voltage, due to fluctuation in the individual cell voltages, the battery can produce reverse current and may discharge. To protect the charger from reverse current, and prevent the battery from discharging, the charge controller added extra voltage (ΔV) to calculate the charger supply voltage (V_s).

$$V_s = V_{out} + \Delta V \qquad (3.3)$$

Figure 3.7 displays the block diagram of the battery charge controller utilized for the proposed bypass topology. Two cascaded PI controls build the CCCV charging control mechanism. When charging a battery with the CCCV charger, the charger first supplies a constant high current in the CC mode until the battery reaches 80% SOC. After that, it switches to the CV mode, which maintains a constant voltage while progressively lowering the charging current to charge the remaining 20% SOC.

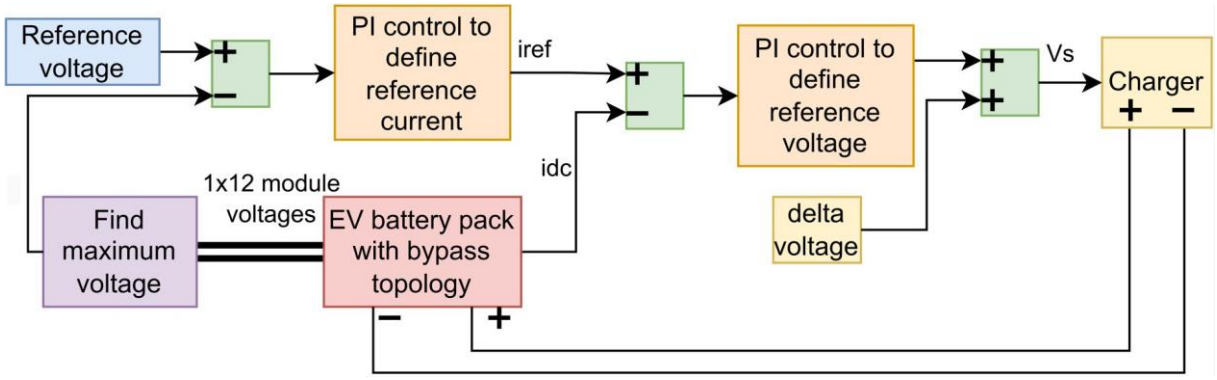

Figure 3. 7 Battery charge controller block diagram

The MATLAB Simulink implementation of battery CCCV charger is presented in Figure 3.8, which continuously monitors the voltages of each module (Vall). The mathematical operational block is utilised to determine the maximum voltage. The first PI controller, which serves as a voltage controller and supplies the reference current (i_{ref}) following the voltage variation of the battery module, receives the difference between the reference voltage and the maximum voltage of the module. Typically, the fully charged voltage of a module serves as the reference voltage. In this thesis, the fully charged voltage of a module is 25.2 V that used as the reference voltage. The error signal becomes zero when the maximum capacity module voltage achieves its full charge voltage (25.2V), and the voltage control maintains a steady voltage while supplying the lowered reference current to progressively lower the charging current. The error

signal between the reference current (i_{ref}) and battery pack charging current (i_{dc}) is received by the second PI controller, which serves as a current controller, and it is used to modify the charger's supply voltage (V_s). The battery can create reverse current and discharge if the voltage of the battery exceeds the charger's supply voltage because of variations in the voltages of the individual battery cells. Therefore, a small delta voltage (10V) is added to the supply voltage.

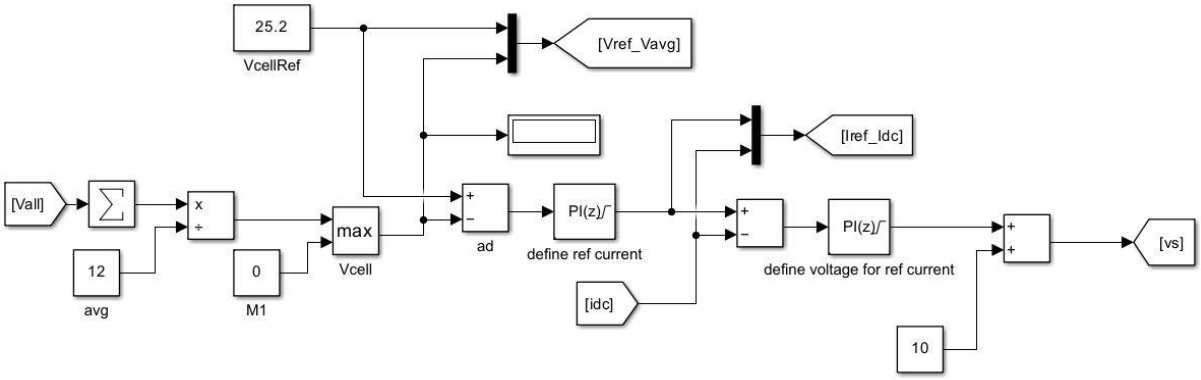

Figure 3. 8 Implementation of battery charge controller in MATLAB Simulink

3.5 EV battery pack and motor selection for testing

The literature [149, 150] shows automotive industry used multiple type of battery cell configuration and motors. The proposed method is flexible and may be applied to any arrangement of series-connected li-ion cells. However, the choice of the Tesla Model S battery pack and induction motor for the purpose state of the art system testing is based on its complex battery architecture. Many cells connected in both series and parallel configurations, offering a comprehensive test environment. Furthermore, according to the literature [151-155], the Tesla Model S is powered by a three-phase, two-pole pair, 270 kW induction motor that has a maximum speed of 9500 rpm, a torque of 440 Nm, lagging power factor 0.88 and efficiency 93%. The reason of taking these parameters from literature is to calculate unknown induction motor equivalent circuit parameters for MATLAB Simulink modelling. This combination

offers a reliable and efficient baseline for assessing the proposed system's effectiveness in real-world circumstances. The Tesla Model S battery pack module consist of 6 submodules and one submodule is made up of 74 cells connected in parallel. So, one module contains 444 cells, with 6S74P configuration. The parameters to construct one battery module are shown in Table 3.2.

Table 3. 2 Battery module parameters (NCR18650B)

Parameters	**Value**	**Units**
Nominal voltage	18	V
Rated capacity	240.5	Ah
Initial state-of-charge	0-100	%
Maximum capacity	240.5	Ah
Cut-off Voltage	15	V
Fully charged voltage	25.2	V
Nominal discharge current	240.5	A
Internal resistance	81	$\mu\Omega$
Capacity at nominal voltage	222	Ah
Exponential zone Voltage	23.28	V
Exponential zone Capacity	7.4	Ah

The Tesla Model S battery pack consist of 16 modules but in this study, the whole battery pack consist of 12 series connected modules makes a configuration of 74P6S12M and contains 5328 cells. This is due to the real-time microcontroller launchpad (TMS320F28379D) ADC converter limitation of 3 ADCs (each with 4 channels) that can read 12 signals simultaneously. The parameters of whole battery pack and induction motor used in this thesis are presented in Table 3.3 and 3.4, receptively.

Table 3. 3 Parameters of the battery pack (74P6S12M)

Parameters	**Value**	**Units**
Nominal voltage	216	V
Rated capacity	240.5	Ah
Initial state-of-charge	0-100	%
Maximum capacity	240.5	Ah
Cut-off Voltage	180	V

Fully charged voltage	302.4	V
Nominal discharge current	240.5	A
Internal resistance	81	$\mu\Omega$
Capacity at nominal voltage	222	Ah
Exponential zone Voltage	279.36	V
Exponential zone Capacity	88.8	Ah
Battery pack power	72	kWh

3.6 Per-phase Induction motor Equivalent circuit model

The per-phase induction motor equivalent circuit model offers approximate representation of its electrical characteristics. Usually, the stator, rotor, and core losses are represented by various parts of the model. Traditionally, the model for a standard induction motor is represented by the stator winding resistance (R_s), stator leakage inductance (L_s), rotor winding resistance (R_r), rotor leakage inductance (L_r) and with the magnetizing branch, which consists of the mutual inductance (L_m) and the core-loss resistance (R_c) in parallel, and R_L is the equivalent mechanical load resistance is a function of rotor resistance and slip (s) as illustrated in Figure 3.9.

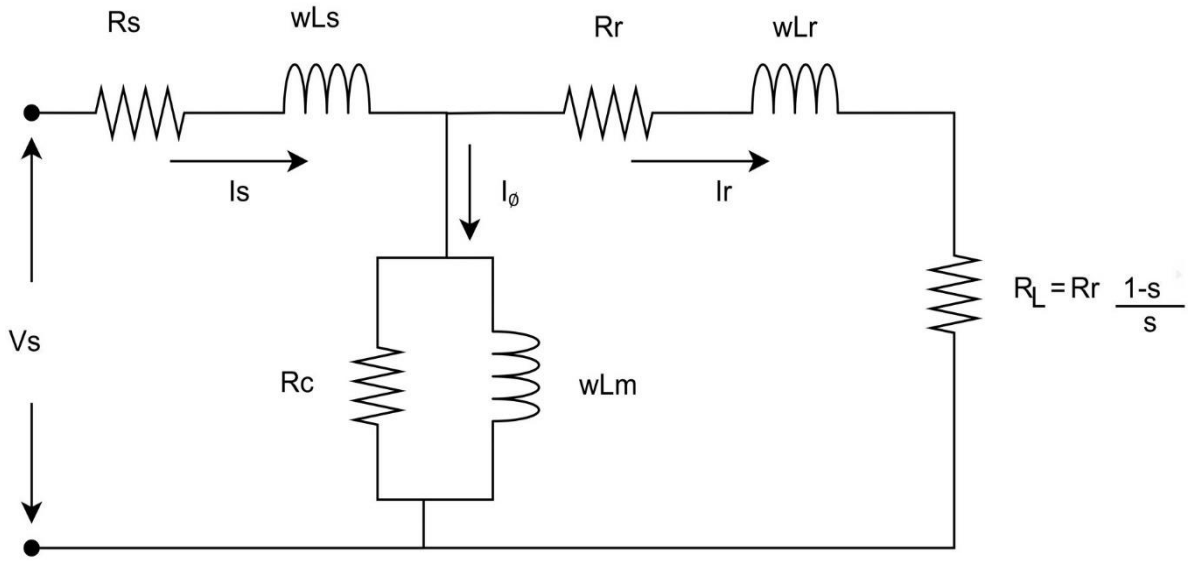

Figure 3. 9 Per-phase equivalent circuit model of an induction motor

The frequency of the motor can be calculated as:

$$f_{\mathrm{n}} = \frac{n_s * \ p}{60} \tag{3.4}$$

The slip (s) is the difference between the rotor's real speed (n_r) and the motor's synchronous speed (n_s) divided by synchronous speed.

$$s = \frac{n_s - \ n_r}{n_s} \tag{3.5}$$

Table 3. 4 Parameters of induction motor and battery pack

Parameters	**Value**	**Units**
Induction motor		
Power (P)	270	kW
Torque (T_{el})	440	Nm
Speed (ω_r)	5800	rpm
Synchronous speed (n_s)	6000	rpm
Maximum speed (ω_{max})	9500	rpm
Power factor ($cos\theta$)	88	%
Efficiency (η)	93	%
Pole pair number (p)	2	
Inertia (j)	2.9	Kg.m^2
Frequency (f_n))	200	Hz
Battery pack		
Voltage (V_s)	302.4	V
Capacity (Q_r)	240.5	Ah
Power (P_{dc})	72	kW

To find the stator current I_{s} of three phase induction motor:

$$I_{\mathrm{s}} = \frac{T_{el} * \ \omega_r}{\sqrt{3}\, V_s\, \eta\, cos\theta} \tag{3.6}$$

The stator starting current I_{st} and maximum torque T_{elmax} are assumed by multiplying a constant value by the stator current and electrical torque of the motor:

$$I_{\mathrm{st}} = 6.5 * I_{\mathrm{s}} \tag{3.7}$$

$$T_{elmax} = 2.8 * T_{el} \tag{3.8}$$

Assuming the stator and rotor resistance (R_s , R_r) and inductance (L_s, L_r) are equal and considering the Table 3.4 parameters to be accurate, solving the following stator starting current (I_{st}) and the maximum torque (T_{elmax}) equations simultaneously to calculate the approximate values of the equivalent circuit parameters for an induction motor as presented in Table 3.5.

$$I_{\mathrm{st}} = \frac{V_s}{(R_s + R_r)^2 + \omega^2 (L_s + L_r)^2} \tag{3.9}$$

$$T_{elmax} = \frac{3p}{2\omega} \frac{{V_s}^2}{(R_s) + \sqrt{{R_s}^2 + (L_s + L_r)^2}} \tag{3.10}$$

Table 3. 5 Approximation of equivalent circuit parameters

Parameters	**Value**	**Units**
stator resistance (R_s)	71.7	$m\Omega$
rotor resistance (R_r)	71.7	$m\Omega$
stator leakage inductance (L_s)	63.41	μH
Rotor leakage inductance (L_r)	63.41	μH

Furthermore, torque, mechanical power, stator current, and efficiency vs. speed of the induction motor are plotted to validate the estimated induction motor parameters. Unfortunately, the results were not satisfactory as the values of power (13 kW), torque (22Nm), and stator current (70 A) were small but the efficiency was 90%. To obtain the necessary rated torque (440 Nm), mechanical power (270 kW), stator current (1018 A), and efficiency (93%) of the induction motor, tunned the equivalent circuit parameters (R_s , R_r , L_s, L_r) to closely follow the torque,

power, stator current, and efficiency, vs speed characteristics. First started with changing the rotor resistance and observing the effects. Reduced rotor resistance results in increased torque, stator current, and mechanical power at a cost of slightly decreased efficiency. Reducing the stator resistance also increased these values, hence, to reach the nominal values, the rotor and stator resistances decreased at the same time. In the third stage, reduce the leakage inductance, which causes a small decrease in power and torque but a larger decrease in stator current. Finally, after careful observation and changes in equivalent circuit parameters, promising results of desired characteristics are obtained with the modified parameters, as Figure 3.10 illustrates. The approximate rated mechanical power is shown in Figure 3.10(a). The torque vs. speed graph of the induction motor is displayed in Figure 3.8(b), which verifies the approximate rated torque at the nominal speed of 607.3 rad/s. Comparably, Figure 3.10(c) displays stator current and Figure 3.10(d) displays 92.8% efficiency at nominal speed.

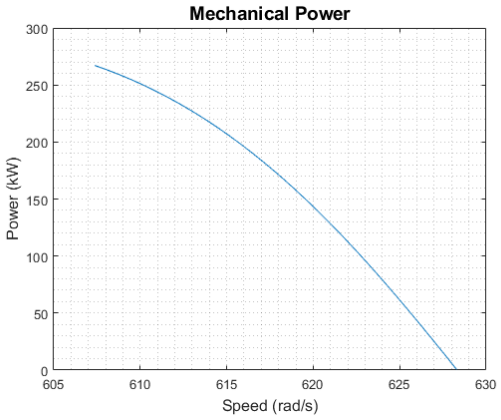

(a) power vs speed

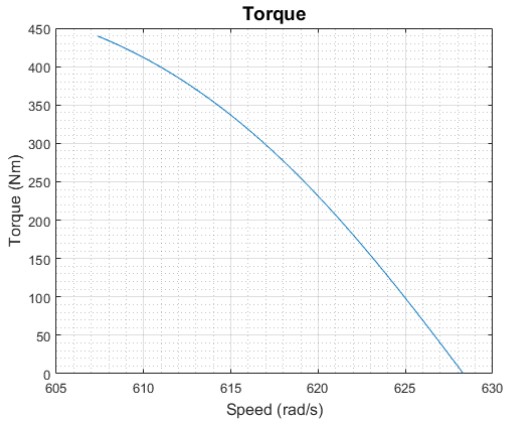

(b) torque vs speed

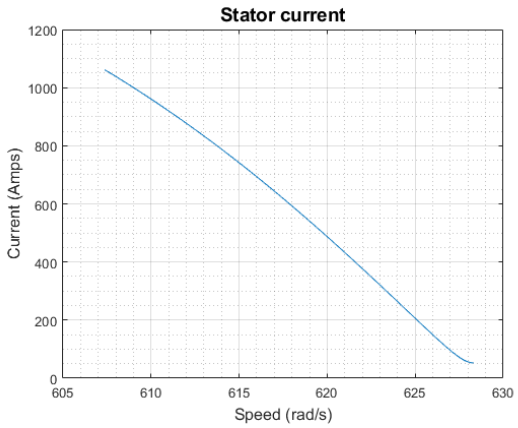

(c) stator current vs speed

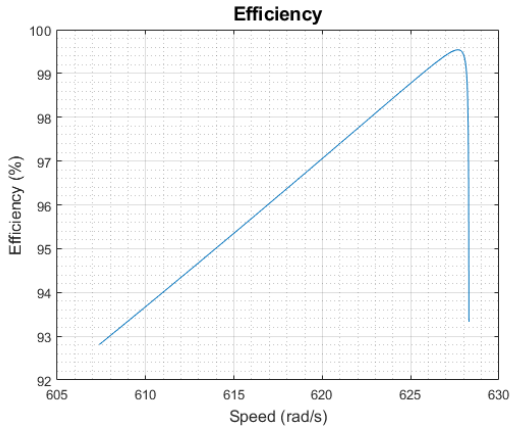

(d) efficiency vs speed

Figure 3. 10 Induction motor speed vs (a) power (b) torque (c) stator current (d) efficiency characteristics

Table 3.6 presents the equivalent circuit characteristics for an induction motor, which are utilised in simulation and HIL experimentation presented in chapter 5 and 7.

Table 3. 6 Equivalent circuit parameters of induction motor

Parameters	**Value**	**Units**
stator resistance (R_s)	3.4	$m\Omega$
rotor resistance (R_r)	2.8	$m\Omega$
Stator leakage inductance (L_s)	22.09	μH
Rotor leakage inductance (L_r)	22.09	μH
Mutual inductance (L_m)	1.6	mH

3.7 FOC of an induction motor

The block diagram of the FOC of an induction motor is presented in Figure 3.12 and it is used for better torque and speed control of induction motors. Depending on the information gained about the flux angle, the vector control or FOC can be either direct or indirect FOC. The slip angular velocity is used in indirect vector control, where the stator currents are split into flux and torque-producing currents and the flux angle in direct vector control is directly determined from the flux. AFOC, RFOC, and SFOC are further classifications for vector control. In this study, the FOC is predicated on indirect control and RFOC, and the complex vectors approach

is used to perform the reference frame transformation. In the following equations subsections of 3.7, the subscript *abc* is used for three-phases, *d* and *q* for the *d*-axis and *q*-axis, *s* for the stator, *r* for the rotor, *m* for mutual, the superscript *r* for the rotational reference frame, and the superscript *s* is used for the synchronous reference frame. The following mathematical formulation for the FOC is adapted from electric motor control book [156] and then used these mathematical formulation to develop the FOC modelling in MATLAB Simulink and OPAL-RT.

3.7.1 Complex vector reference frame representation

There are several reference frame transformations to simplify the calculations, by altering the rotation speed, for instance, the generalized rotating transformation or arbitrary reference frame transformation. The time-varying coefficients are eliminated via the reference frame transformation, which converts the three-phase *abc* variables into *dqn* variables. A three-phase current in the complex plane can be represented by a vector I_{abc} known as a complex vector. The whole three-phase system can be analysed instead of one phase separately using the complex vector method. The complex vector for three-phase current is represented as:

$$I_{abc} = \frac{2}{3}(i_a + i_b e^{j\frac{2\pi}{3}} + i_c e^{j\frac{4\pi}{3}}) \tag{3.11}$$

The inverse transformation from complex vector to three-phase currents is given by:

$$I_a = Re[I_{abc}] \tag{3.12}$$

$$I_b = Re\left[e^{-j\frac{2\pi}{3}} I_{abc}\right] \tag{3.13}$$

$$I_c = Re\left[e^{-j\frac{4\pi}{3}} I_{abc}\right] \tag{3.14}$$

where *Re* represents the complex vector's real component.

Since the orthogonal coordinates of the complex plane and the *dq* coordinate system are the same, the real and imaginary axes are equivalent to the d and q axes, respectively. The complex vector I_{abc} in the stationary reference frame is therefore identical to I_{dq}. The *dq*-axis currents in the rotating reference frame, however, can be represented as follows since the *dq*-axis rotates with the synchronous speed (ω) or rotor flux speed.

$$I_d = \frac{2}{3}\left[I_a \cos\ \theta + I_b \cos\left(\theta - \frac{2}{3}\pi\right) + I_c \cos\left(\theta - \frac{4}{3}\pi\right)\right] \quad (3.15)$$

$$I_q = -\frac{2}{3}\left[I_a \sin\ \theta + I_b \sin\left(\theta - \frac{2}{3}\pi\right) + I_c \sin\left(\theta - \frac{4}{3}\pi\right)\right] \quad (3.16)$$

And by using the Euler formula the *dq*-axis currents become:

$$I_{dq} = I_{abc}\, e^{-j\theta} \quad (3.17)$$

There is only a phase difference (θ) between the complex vector and rotating frame (*dq*-axis) which is due to angular displacement, which can be calculated by equation 3.20.

3.7.2 Decoupling of stator currents

In induction motors, the torque and flux-producing current are supplied simultaneously from the stator three-phase windings. Instantaneous torque control requires determining the field flux and torque components from the stator currents ($i_{as},\ i_{bs},\ i_{cs}$). An induction motor can only achieve instantaneous torque control under two fundamental requirements.

- The 90-degree angle exists between both torque and flux-producing currents.
- The independent control of both torque and flux-producing currents.

The reference frame transformation technique is used in the instantaneous torque control operation to convert the three-phase stator currents into *dq*-axis currents. Traditionally, the *d*-axis stator current is defined as the current that generates torque, while the *q*-axis stator current is identified as the current that produces flux. To fulfil the first criteria by obtaining orthogonal currents, it is important to align the d-axis and flux vector's (φ) actual location in vector control. The flux vector in an induction motor is the spinning magnetic field generated from the three-phase stator currents and the flux vector position illustrated in Figure 3.11.

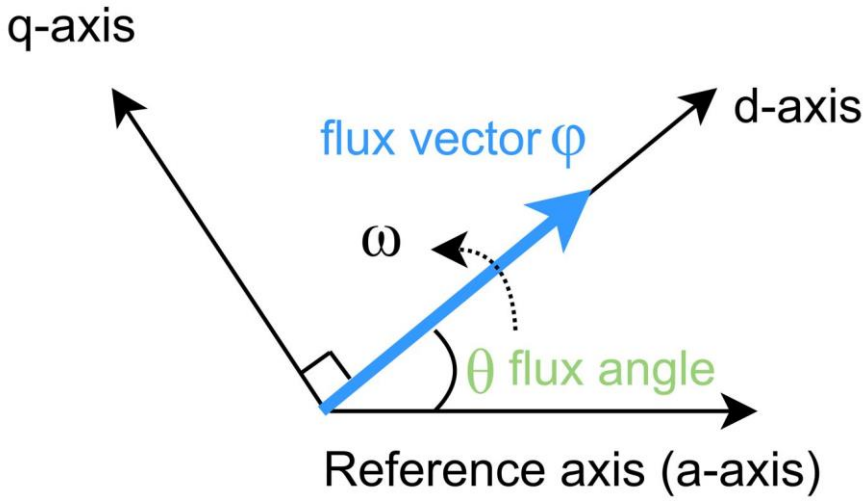

Figure 3. 11 Rotating frame *dq*-axis flux vector and flux angle presentation

Where θ is the rotating flux angle, ω is synchronous speed or rotor flux speed, and φ is the flux vector. Considering the flux vector (φ) rotates at synchronous speed (ω), then the *d*-axis must rotate synchronously to keep the alignment with the rotating flux vector. The real flux-producing current in synchronous *dq* reference frame is produced by the *d*-axis stator current. Therefore, the *d*-axis stator current (i_{ds}) can be controlled to control the flux magnitude.

The equation (3.18) represents torque (T) of induction motor:

$$T = \frac{3}{2}\frac{P}{2}\frac{L_m}{L_r}\left(\varphi_{dr}^{s} i_{qs}^{s} - \varphi_{qr}^{s} i_{ds}^{s}\right) \qquad (3.18)$$

Given that the flux in equation (3.18) above is thought to represent the rotor's flux linkage and that it is limited to the *d*-axis, the torque can be independently controlled by the *q*-axis stator current (i_{qs}) provided that the *d*-axis stator current (i_{ds}) is controlled to maintain a constant flux vector magnitude.

$$T = \frac{3}{2}\frac{PL_m}{2}\frac{L_m}{L_r}|\varphi| i_{qs}^{s} \quad where\ \left(\varphi_{dr}^{s} = |\varphi|, \varphi_{qr}^{s} = 0\right) \qquad (3.19)$$

Stator currents on the *d* & *q*-axes are orthogonal to or independent of each other. Whereas the *q*-axis stator current generates torque, the *d*-axis stator current provides flux. Consequently, it is possible to individually adjust the torque and flux.

3.7.3 Estimation of the Rotor Flux angle

The integral of the synchronous speed (ω) in the rotating frame is used to compute the rotor flux angle (θ), which fluctuates over time between the rotating and stationary reference frames.

$$\theta = \int \omega(t)dt + \theta(0) \qquad (3.20)$$

Where the initial angle $\theta(0)$ at time (t) is equal to zero, is assumed to be zero ($\theta(0) = 0$). To find the synchronous speed (ω) is discussed in the following section 3.6.4. and can be calculated from equation 3.22.

3.7.4 Indirect Rotor flux-oriented control

The indirect vector control is straightforward to utilise slip to derive the rotor flux angle indirectly. The slip dictates how the stator current is split into flux and torque-producing current, as can be seen in the steady-state per phase equivalent circuit of an induction motor presented

in section 3.5. Therefore, the necessary torque and flux can be obtained by controlling the slip. finally getting the critical slip requirement for the indirect vector control by holding the rotor flux linkage constant, which is:

$$\omega_s = \frac{1}{T_r}\frac{i_{qs}^s}{i_{ds}^s} \qquad where\ \left(T_r = \frac{L_r}{R_r}\right) \tag{3.21}$$

The above equation shows the angular frequency (ω_s) or slip relation to *d* & *q* currents. Then the rotor flux speed (synchronous speed, ω) can be obtained by using the rotor velocity (ω_r) and the slip speed (ω_s).

$$\omega = (\omega_s + \omega_r) \tag{3.22}$$

3.7.5 Flux estimation

The voltage model, which is based on stator equations, and the current model, which is based on rotor equations, are the two ways to estimate the rotor flux linkage. With the current flux estimation model, the required rotor flux linkage may be obtained as

$$\frac{d\varphi_{dr}^r}{dt} = \frac{R_r}{L_r}\varphi_{dr}^r + \frac{R_r}{L_r}L_m i_{ds}^r \tag{3.23}$$

$$\frac{d\varphi_{qr}^r}{dt} = \frac{R_r}{L_r}\varphi_{qr}^r + \frac{R_r}{L_r}L_m i_{qs}^r \tag{3.24}$$

The differential equations (3.23) and (3.24) can be integrated to obtain the rotor flux linkages.

3.7.6 Filed weakening

An effective technique for raising an induction motor's speed well above its nominal speed is field weakening. The torque decreases simultaneously when the speed is beyond the nominal value. Therefore, when high torque is required at low rotation rates and low torque is

required at high rotation speeds, field weakening is utilized. The reference flux can be obtained by the rotor mechanical speed (ω_r), rotor nominal speed (ω_{rn}), and rotor nominal flux (φ_{rn}) for a flux controller in FOC.

$$\varphi_{\mathrm{ref}} = \varphi_{\mathrm{rn}} \quad , \text{if } (\omega_r < \omega_{rn}) \tag{3.25}$$

$$\varphi_{\mathrm{ref}} = \frac{\omega_{rn}}{\omega_r} \times \varphi_{\mathrm{rn}} \quad , \text{if } (\omega_r \geq \omega_{rn})$$

The nominal rotor flux can be calculated using nominal values, nominal stator current (I_n), nominal motor speed (ω_n), nominal slip (s_n), and equivalent circuit parameters.

$$\varphi_{\mathrm{rn}} = \frac{L_m \times R_r \times I_n}{\sqrt{{R_r}^2 + (s_n \times \omega_n \times L_r)^2}} \tag{3.26}$$

Figure 3.11 depicts the vector control system block diagram for an induction motor, which includes commonly utilized PI controller for flux, speed, and current control.

3.7.7 Voltage and speed relationship

It is crucial to determine the relationship between the voltage and speed of the induction motor for the proposed modular battery packs. Depending on the motor speed, the battery pack voltage must be regulated to provide a variable DC-link voltage. The magnitude of the reference voltage (V_{m}) according to motor speed using *dq* reference frame voltage, as it is equal in both rotating and stationary reference frames.

$$V_{\mathrm{m}} = \sqrt{{V_d}^2 + {V_q}^2} \tag{3.27}$$

This reference voltage magnitude is further used in discharging control algorithm to in chapter 4, section 4.3.1 to identify the number of bypass modules to provide variable DC-link voltage and perform voltage balancing.

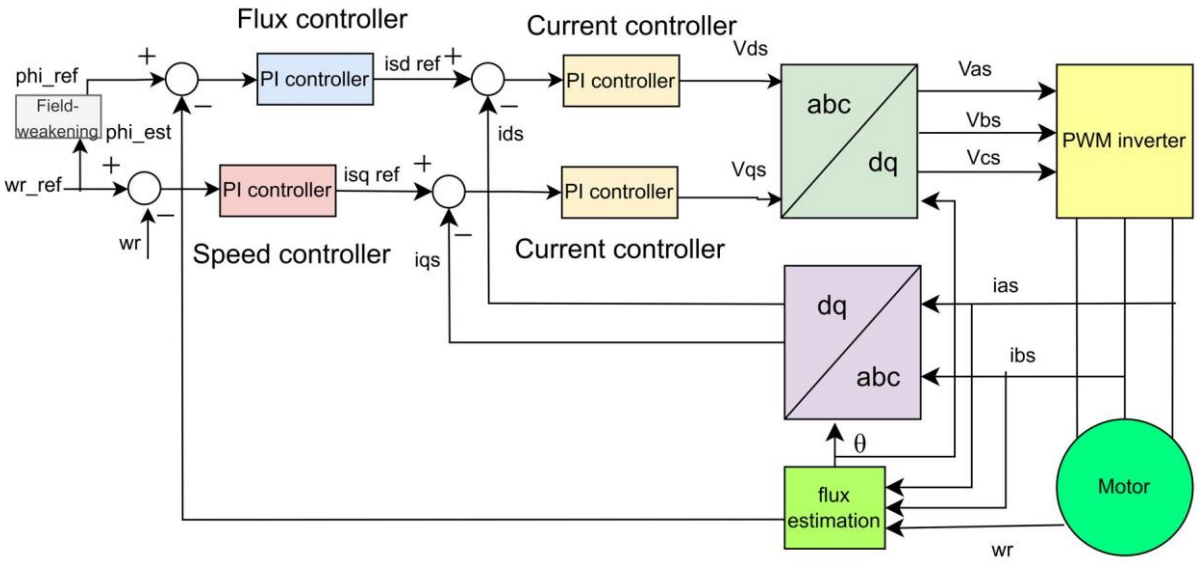

Figure 3. 12 Block diagram of FOC of an induction motor with controllers

This chapter optimised the default li-ion battery cell model and gives the parameters of building EV battery pack with the series and parallel combination of cells. The approximation of induction motor electrical model is achieved. The implementation of battery pack charging control and FOC is also discussed in this chapter. This EV battery pack and inductor motor model and associated controller will be used in the next chapter to develop the proposed modular battery pack.

Chapter 4: Proposed Bypass Balancing Method and Control

The bypass balancing method is proposed in this chapter, along with an adaptive control system, to provide modular battery packs and achieve voltage balancing. The control system includes adjusting the supply voltage during charging and modifying the battery pack voltage by the motor speed during discharging. The proposed topology and the controller operating principle for the battery pack's charging and discharging modes of operation are also covered in this chapter.

4.1 Proposed bypass cell balancing topology structure

The bypass balancing technique has a simple structure of two switches parallel to each battery cell or module. This simple structure is beneficial for implementation of this circuit in EV, due to low cost, weight, and volume. Li-ion cells are arranged in parallel and series configurations to form battery modules, which are then coupled in series to form an entire EV battery pack. The parameters, number of cells and configuration of single cell, module and battery pack are presented in chapter 3, section 3.2. Figure 4.1 (a,b) shows the basic block diagram and MATLAB Simulink diagram of an EV battery pack with a modular bypass balancing architecture. This diagram illustrates how the EV battery pack is connected to the bypass topology. Every module in the battery pack is wired to two switches, which are generally MOSFETs. The bypass switches (*S1, S3, S5,... S11*) are used to break the cell series connection to bypass the module, while the other series switches (*S2, S4, S6,... S12*) are employed to work in series to make a series connection between modules. It is essential to have a switching delay between the switch ON and OFF to prevent short circuits. The proposed topology is

implemented for the modular level, with 12 modules (*M1, M2, M3,..., M12*) connected in series. Each module is made up of 6 series connected (*sb1, sb2, sb3,..., sb6*) submodules, and each submodule consists of 74 parallel *(b1, b2, b3,..., b74*) cells, so one module consist of 444 cells .

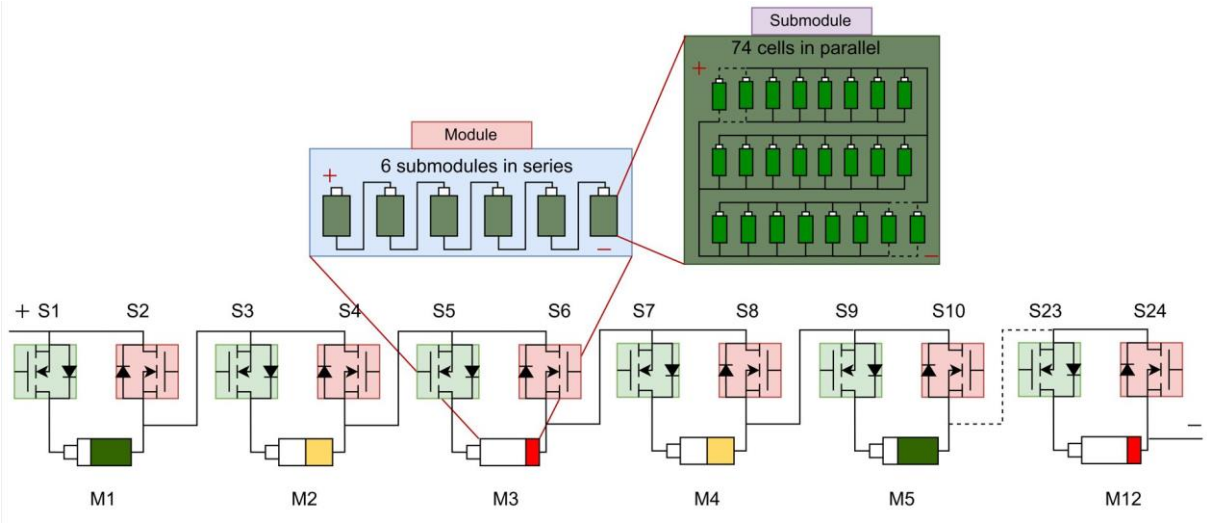

(a)

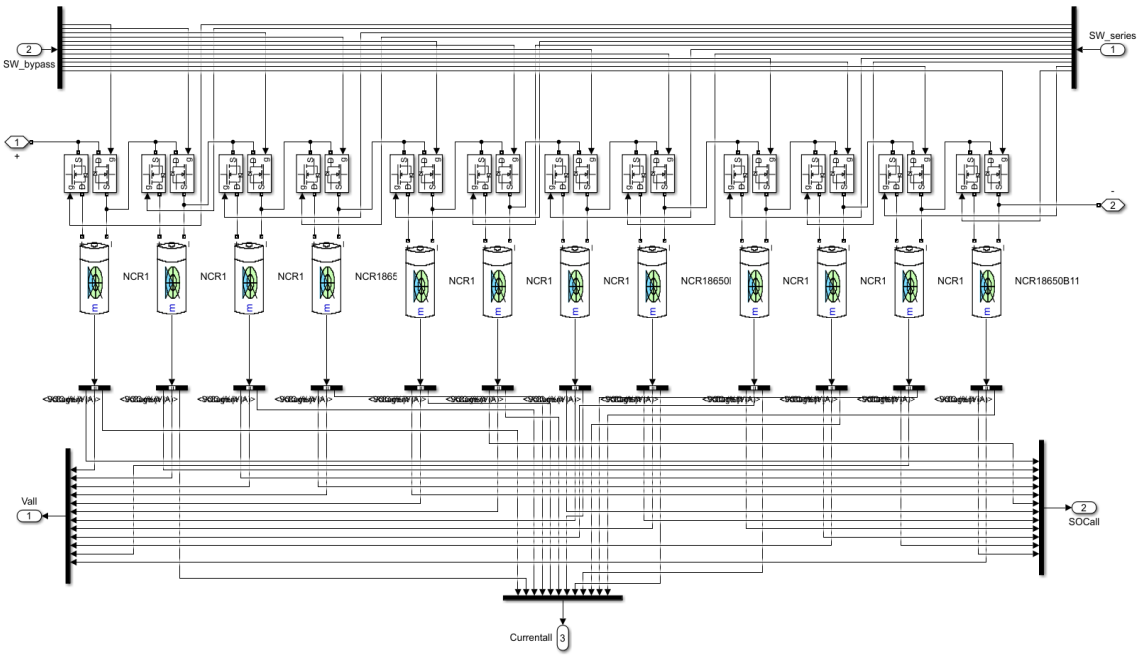

(b)

Figure 4. 1 Simulink and block diagram of EV battery pack with bypass topology.

4.2 Bypass cell balancing topology during battery pack charging

Figure 4.2 (a,b) shows the block diagram and MATLAB Simulink diagram of the suggested bypass balancing architecture for charging along with the microcontroller and CCCV charger. The battery charge controller was explained in Chapter 3, section 3.4. The charge controller utilises voltage (V_{dc}) and current (I_{dc}) signals to adjust the supply voltage according to the number of bypass modules and then sends the supply voltage signal to the DC fast charger. The bypass and series switches of the topology are controlled by the switching controller. The switching controller continuously monitors the individual module voltage and takes the decision accordingly to adjust the switching control signals (bypass switches and series switches). In Simulink the controlled voltage source is used as a DC fast charger connected to the battery pack through a series RL circuit that limits and smooth out the current ripples. The DC fast charger output voltage is controlled according to the battery charger supply voltage command.

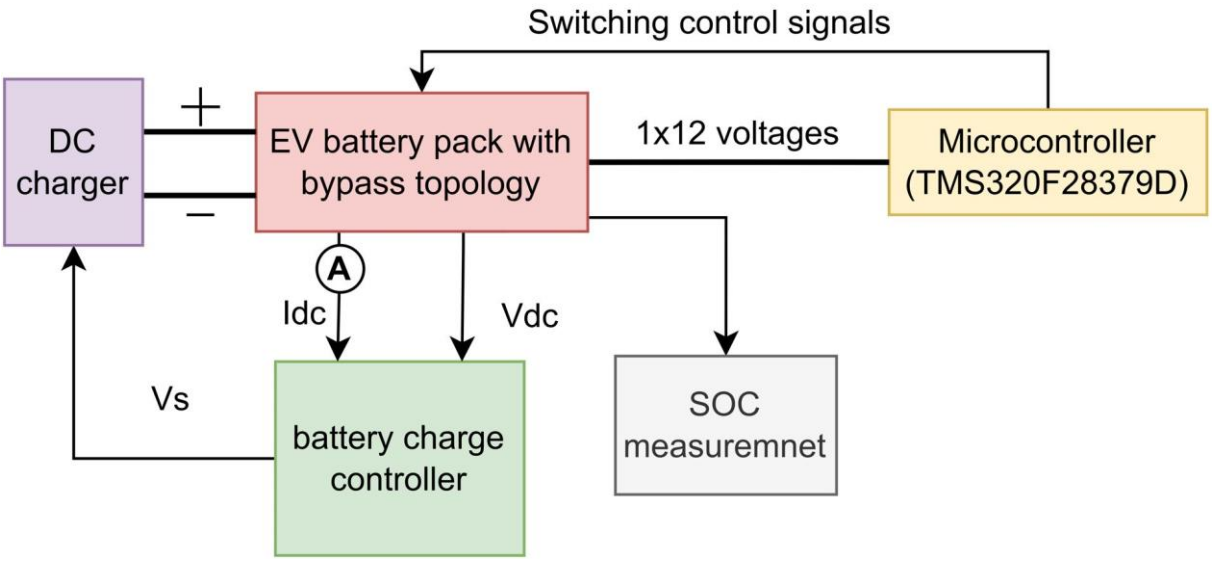

(a)

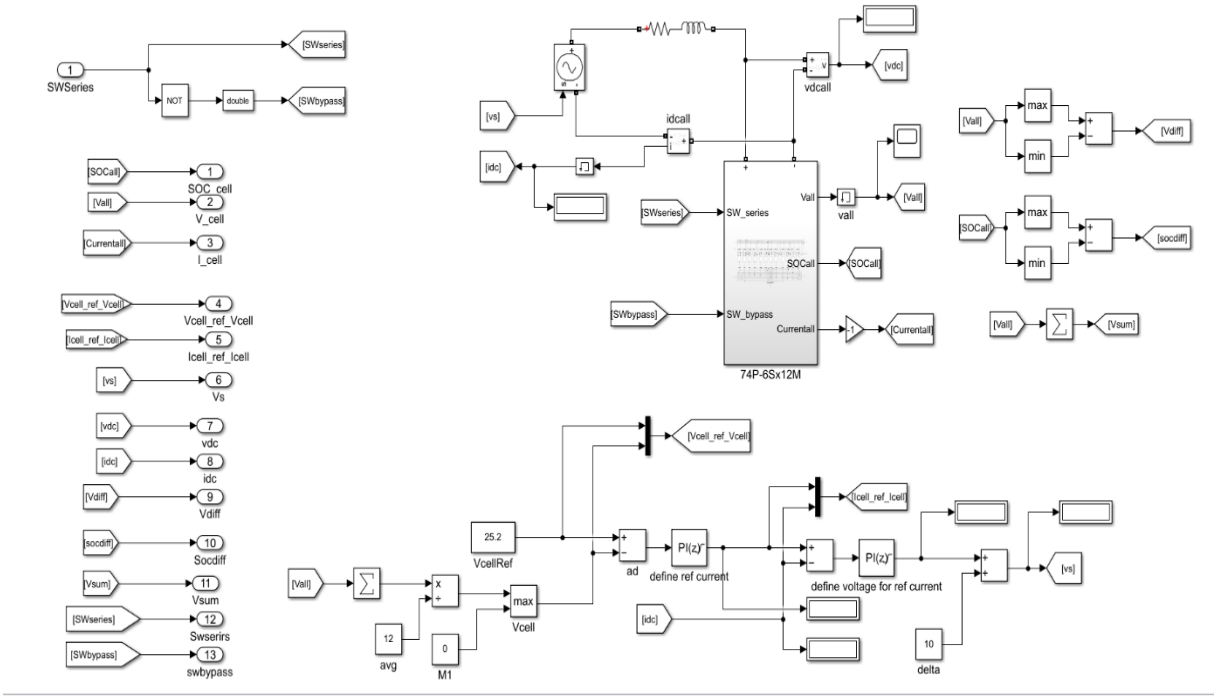

(b)

Figure 4. 2 Simulink and block diagram of proposed topology with controller during charging

4.2.1 Operating principle of EV battery pack charging

A cell balancing control algorithm typically consists of multiple important steps. Initially, either charging or discharging, the voltage of each module is continuously monitored. Upon determining a module with maximum voltage, the associated bypass switches become active. By establishing a temporary parallel channel, this switch permits a charging current to go around the module that has maximum charge. Because of this, the modules with lower voltages keep charging while the modules with higher voltages are bypassed.

the primary objective of the charging controller is to reroute the charging current of the battery modules with the highest levels of charge. The working concept of the bypass topology during the charging condition is depicted in the flow chart in Figure 4.3. The sensors continuously measure each battery pack module's voltage. Arrange these values into an array

variable so that sorting in ascending or descending order can easily be achieved. The voltage values are sorted in descending order for the charging control as the highest voltage cell needs to be bypassed. To calculate the voltage difference, find the highest and lowest voltage modules. Through the prompt activation of bypass switches, cell balancing is initiated if modules vary from a predetermined threshold value. Continue to calculate imbalance using this method and terminate the cell balancing when the imbalance reaches the lowest allowable value. Identify the specific number of bypass modules and modify the supply voltage of CCCV charger accordingly. Appendix A shows the microcontroller code for the battery pack charging mode of operation with the proposed bypass method.

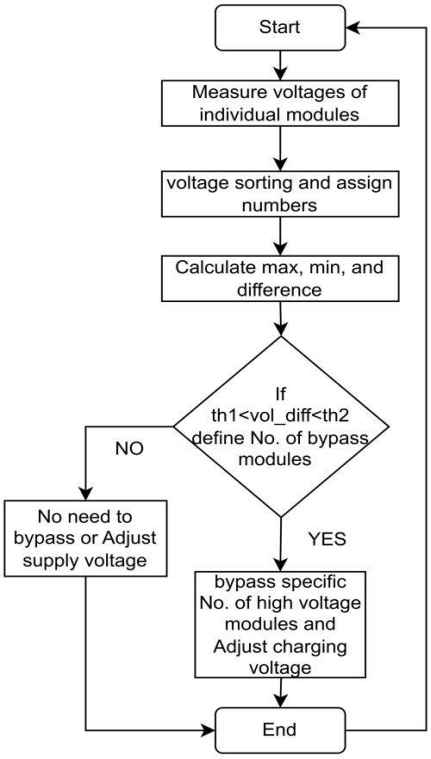

Figure 4. 3 Flow chart of the controller during battery charging

4.3 Bypass cell balancing topology during battery pack discharging

For EV battery pack discharging, the Figure 4.4(a,b,c) illustrates the block diagram and simulation of a proposed bypass balancing architecture coupled with a traction inverter and

motor. The inverter and EV battery pack are connected to supply the induction motor with a three-phase AC power source. The induction motor speed control is implemented by FOC, which was explained in Chapter 3, section 3.6. The pulse width modulation (PWM) generator's three-phase reference voltage is generated by implementing FOC. The microcontroller receives the computed amplitude of the three-phase reference voltages and uses it to further explore and modify the switching control signals to alter the battery pack voltage in accordance with the induction motor's speed. The number of bypasses is calculated by the voltage and speed relationship to bypass the number of modules accordingly. When discharging, the weak modules are chosen for bypass, and the high-energy modules are chosen to give the necessary power to the motor.

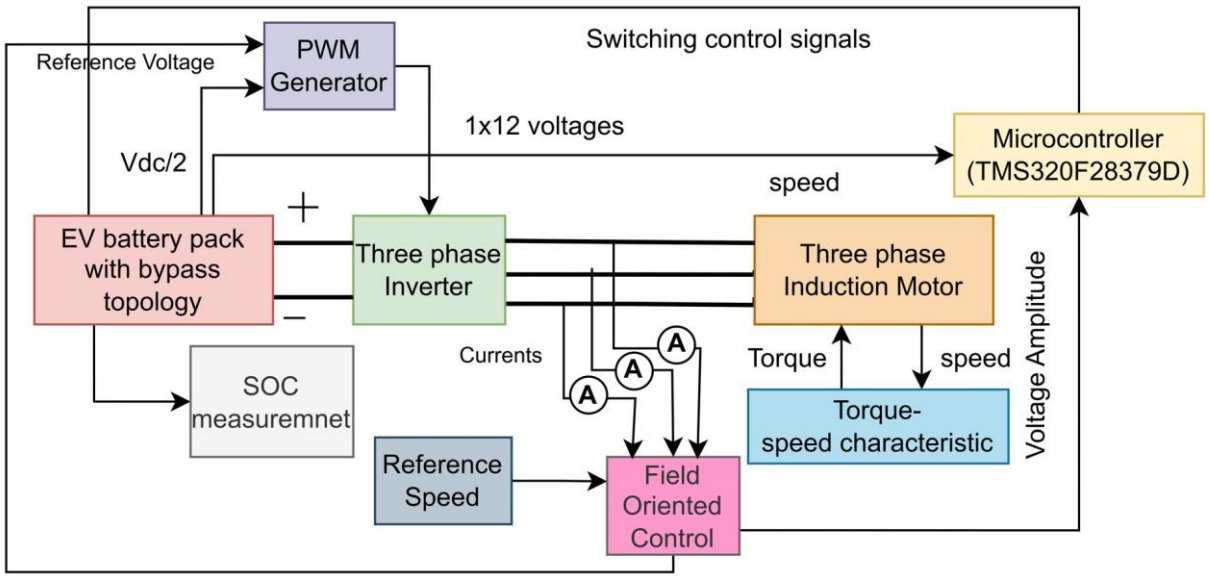

(a)

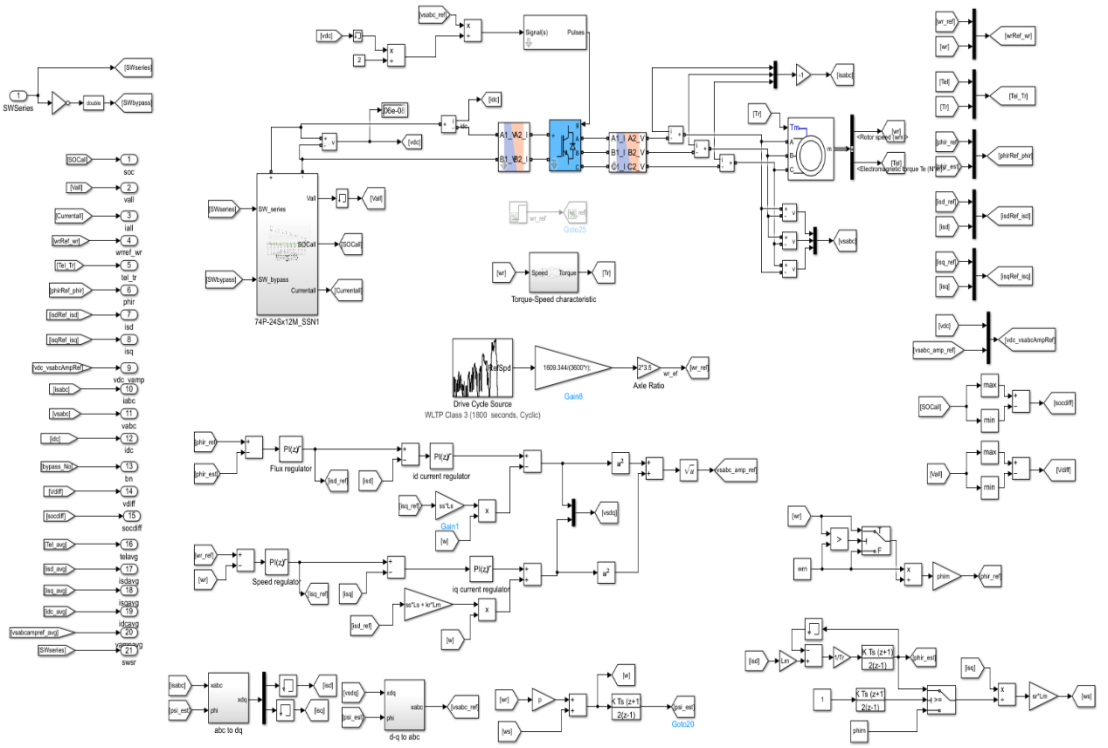

(b)

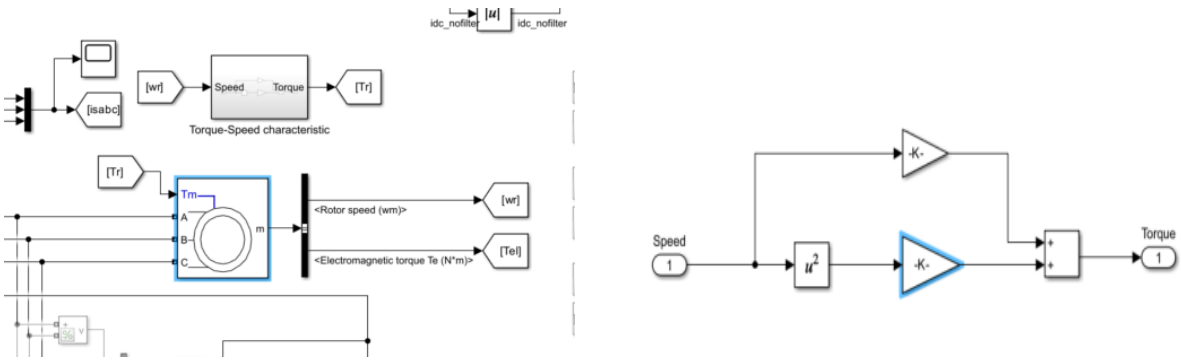

(c)

Figure 4. 4 Simulation and block diagram of proposed topology with controller during discharging

The Figure 4.4(c) shows the induction motor input as a torque which is calculated through torque-speed characteristics. The torque and speed relation of an induction motor is non-linear thus linear and quadratic equation is used to create the torque-speed relationship.

$$T = k_1 * \omega + k_2 * \omega^2 \quad (4.1)$$

During the discharging process of the battery pack, the torque is applied to the motor and the speed or load profile is provided by the WLTP-3 drive cycle which is controlled through FOC. Thus, the power (P) can directly be derived using power formula in equation 4.2, which is torque (T) into angular speed (ω) of the motor.

$$P = T * \omega \quad (4.2)$$

4.3.1 Operating principle of EV battery pack discharging

Discharging involves a slightly more complex control operation for the bypass balancing topology than charging requires. It involves FOC and required information about the motor speed vs voltage relationship. The control algorithm intended to supply a variable DC-link voltage to the traction inverter and carry out the voltage balancing procedure during the battery pack's discharging is explained by the flow chart in Figure 4.5. The first three parts of the controller flow are like the charging controller. First, measure the voltage of individual modules, then assign the index numbers and do sorting but in ascending order of voltage values, as the lowest voltage of the module needs to be bypassed, and finally calculate the maximum, minimum, and difference of voltages. The voltage amplitude needed for the traction inverter is also included in the controller, based on the motor speed determined by FOC. The necessary voltage amplitude dictates the quantity of bypass modules. To generate the necessary power, the high-energy modules are connected in series, whereas the low-energy modules are bypassed through switches. The process of balancing the voltages of modules is continuous until the battery pack is fully discharged and reaches its predefined cutoff voltage

for the protection of the battery pack. Appendix A shows the microcontroller code for the battery pack discharging mode of operation with the proposed bypass method.

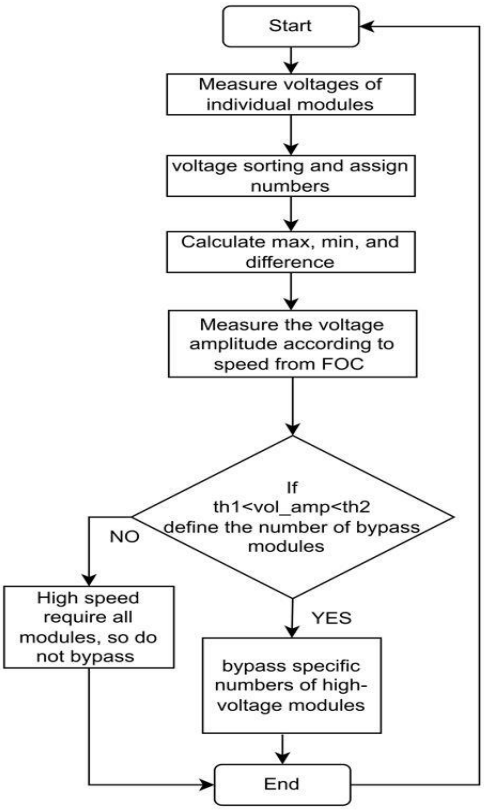

Figure 4. 5 Flow chart of the controller during battery charging

This chapter explain the process for implementation of the proposed method and controller design, which are then tested in MATLAB Simulink to analyse the results in next chapter.

Chapter 5: Performance assessment of proposed bypass topology

This chapter presents the proposed bypass topology's working principle using MATALB Simulink. The simulation result includes the verification of the battery charge controller, battery performance without a balancing circuit, and voltage balancing during charging and discharging.

5.1 CCCV charge control validation

The voltage controller, current controller, and CC to CV modes of operation of the battery charge controller are validated through testing at three different charging currents (C-rates: 0.5C, 1C, and 2C). The operating principle and block diagram of the battery charge controller are explained in Chapter 3, section 3.4. Figure 5.1(a, b, c) displays the simulation results of the CCCV charge control at various charging currents (0.5C, 1C, and 2C), demonstrating the CC to CV mode of operation. The findings demonstrate that, as could be expected for a Li-ion cell, the CC to CV mode is toggled when the battery pack's SOC rises above 80%. Since the voltage and current follow the reference input signal, the findings further illustrate the performance of voltage and current controller. Furthermore, the results in Figure 5.1(a, b, c) verifies the charging current is proportional to the charging speed. The rate at which a battery is charged or discharged in relation to its maximum capacity is known as its C-rate. 0.5C, 1C and 2C means the battery will charge approx. in 120, 60 and 30 minutes, respectively. however, as in CCCV charging the battery is charged 80 to 85 % in CC mode and the remaining charge in CV mode. Thus, to reach 100% SOC the battery takes a little longer time and charge in 133, 66 and 33 minutes for 0.5C, 1C and 2C, respectively.

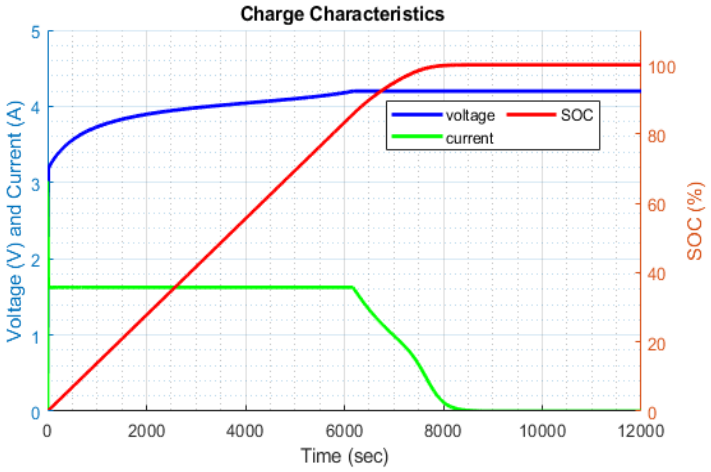

(a) Simulation results of CCCV charger at 0.5C-rate

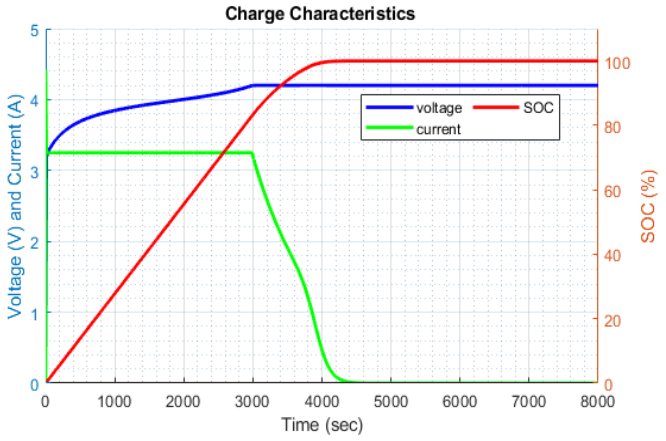

(b) Simulation results of CCCV charger at 1C-rate

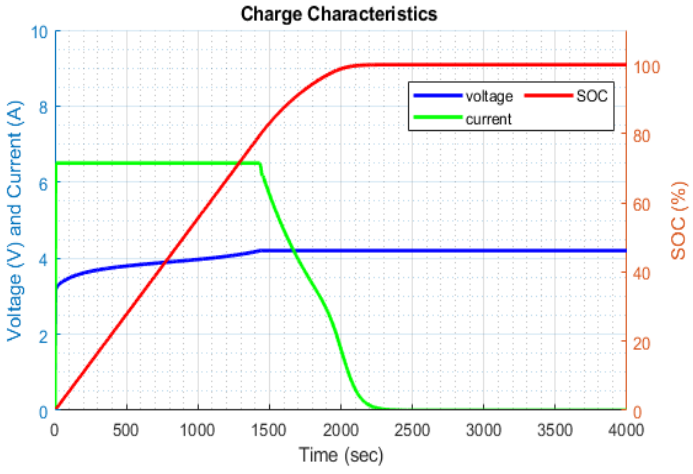

(c) Simulation results of CCCV charger at 2C-rate

Figure 5. 1 CCCV charge controller at multiple C-rates

5.2 Residual imbalance without cell balancing

To check the importance of overvoltage protection limit (25.8 V per module and 4.3 V per cell) and cell balancing topology for the EV battery pack, two cases of initial SOC imbalance are considered. The maximum initial SOC difference ($SOC_{\max\ \_diff}$) is calculated as:

$$SOC_{\max\ \_diff} = SOC_{\max} - SOC_{\min} \quad (5.1)$$

where $SOC_{\min}$ and $SOC_{\max}$ are the minimum and maximum SOC of the battery pack modules.

The maximum initial voltage difference ($V_{\max\ \_diff}$), is calculated by subtracting the lowest module voltage $V_{\min}$ from the highest module voltage $V_{\max}$.

$$V_{\max\ \_diff} = V_{\max} - V_{\min} \quad (5.2)$$

The EV SOC imbalance usually falls between 5% and 10% thus two cases of initial SOC imbalance are considered that are presented in Table 5.1. Case 1 is selected to highlight the significance of cell balancing techniques in real-world situations with slight imbalances. Case 2, on the other hand, poses a serious initial SOC imbalance that raises concerns about the performance of the proposed balancing method. Case 2 is appropriate for extensive testing since it has both modest variations between certain cells and large SOC changes between others. Case 2 has the worst initial SOC imbalance of 80%. To assure the stability and effectiveness of the balancing method, the proposed structure is put to the test under the worst-case SOC imbalance for further charging and discharging testing. The battery pack's series-connected modules are denoted by the letters M1 through M12.

Table 5. 1 Cases of different initial SOC conditions

Initial SOC (%)	**M1**	**M2**	**M3**	**M4**	**M5**	**M6**	**M7**	**M8**	**M9**	**M10**	**M11**	**M12**
Case 1: all different	10	11	12	13	14	15	16	17	18	19	20	21
Case 2: one high one low other different	10	45	46	47	48	49	50	51	52	53	54	90

The SOCs of each module are displayed in Figure 5.2(a, c), and the corresponding voltages are displayed in Figure 5.2(b, d) for Cases 1 and 2. When the battery pack is charged without consideration of the protective limit and cell balancing, the results show the voltages of the modules surpass the maximum voltage limit (25.8V).

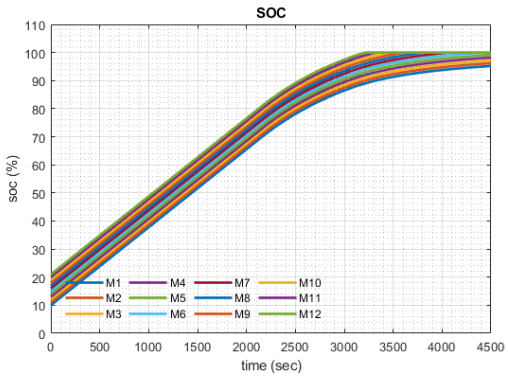

(a) Case 1: SOC graph

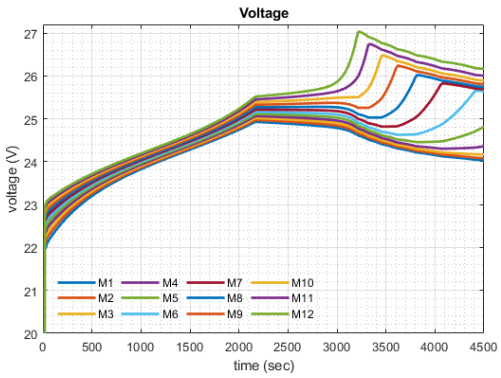

(b) Case 1: voltage graph

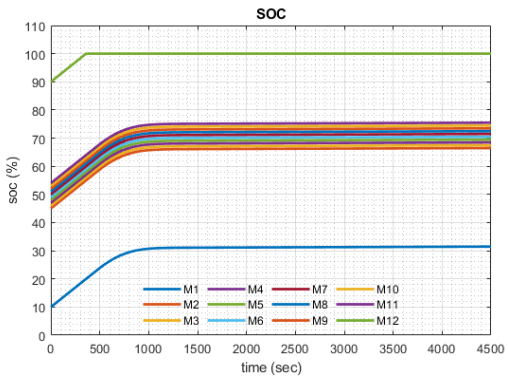

(c) Case 2: SOC graph

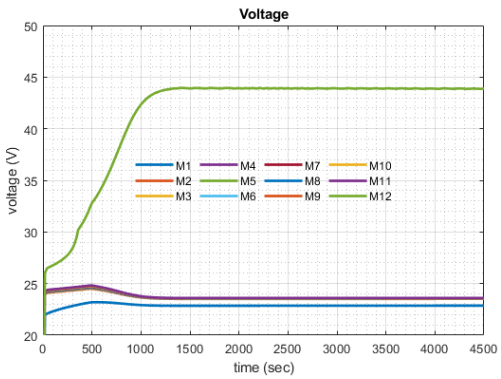

(d) Case 2: voltage graph

Figure 5. 2 Battery charging without protection limit and cell balancing for case 1 and 2

After the overvoltage protection limit has been implemented, when any battery cell surpasses its maximum voltage limit (25.8 V per module and 4.3 V per cell) the battery pack must be stopped from charging. As shown in Figure 5.3(b) the charging process is stopped at 3000 seconds when one of the modules exceed the voltage limit is due to over voltage protection. For case 1, the relevant SOC and voltages are shown in Figure 5.3(a, b). In Case 2, the highest voltage module charges quickest due to a maximum initial SOC imbalance of 80%. However, when the battery module is over the maximum voltage limit (25.8 V), charging is stopped to protect the battery pack. For case 2, the SOCs and voltages of separate modules are displayed in Figures 5.3(c) and 5.3(d). It implies that the battery pack cannot be charged in the with higher initial imbalance if there is no cell balancing circuit. Furthermore, if a battery pack has a weak capacity cell, the BMS will stop charging and the battery cannot be charged.

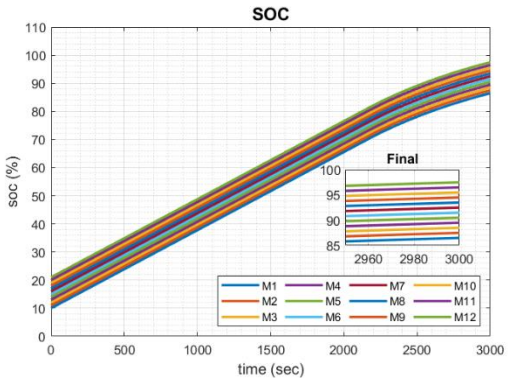

(a) Case 1: SOC graph

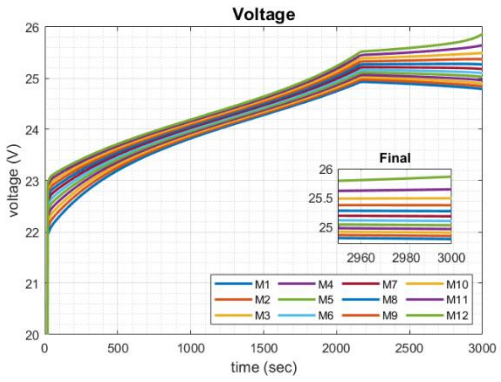

(b) Case 1: voltage graph

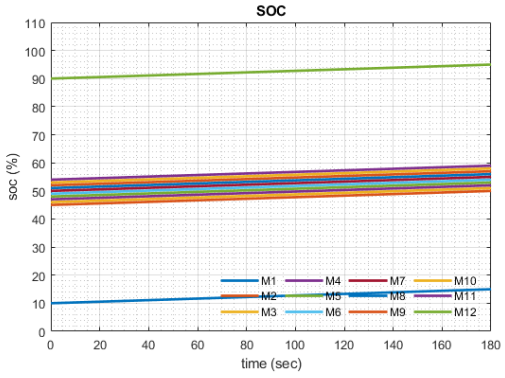

(c) Case 2: SOC graph

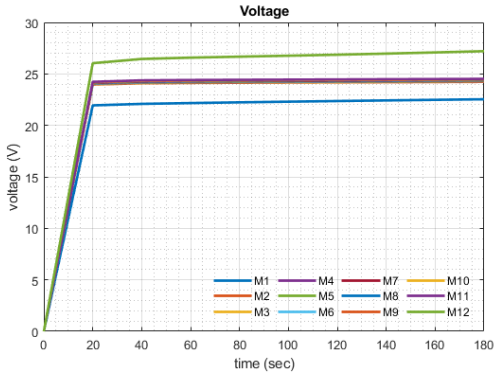

(d) Case 2: voltage graph

Figure 5. 3 Battery charging only without cell balancing for cases 1 and 2

The numerical data of residual imbalance without using cell balancing topology is given in Table 5.2 and collected from simulation results illustrated in Figure 5.3(a, b, c, d). The results show the importance of cell balancing circuit as the residual imbalance at the of charge and discharge will be the same at the start and end.

Table 5. 2 SOC and Voltage residual imbalance without balancing

1C-rate	**Initial SOC imbalance (%)**	**Residual SOC imbalance (%)**	**Initial Voltage imbalance (V)**	**Residual Voltage imbalance (V)**
Case-1	11	11	1.01	1.01
Case-2	80	80	4.1	4.1

5.3 Residual imbalance of charging with multiple C-rates

The proposed bypass method is tested for SOC/voltage balancing between series connected battery pack module with three different charging current rates (0.5C, 1C and 2C) to evaluate the balancing controller, CCCV controller and bypass method performance. The parameters of individual modules used for this testing is presented in chapter 3, section 3.2. The total battery pack capacity is 240.5 Ah, so the charging current is 120.25A, 240.5A and 481A for 0.5C, 1C and 2C, respectively. The maximum initial SOC imbalance of 80% is considered for series connected modules and each module initial SOCs are reported in Table 5.3.

Table 5. 3 Initial SOC conditions for charging

Initial SOC (%)	**M1**	**M2**	**M3**	**M4**	**M5**	**M6**	**M7**	**M8**	**M9**	**M10**	**M11**	**M12**
Case: one high one low other different	10	45	46	47	48	49	50	51	52	53	54	90

Consider that the SOC is measured to demonstrate the voltage of the Li-ion cell provides a decent proxy for SOC, and the control algorithm for balancing is based on the voltages of individual modules. However, the voltages of high SOC are balanced faster (10 seconds) than SOC balancing, because of voltage based controller, and Li-ion cell voltage and SOC

relationship. The Li-ion cells produce nearly same voltage with minimum difference for different SOC.

Figure 5.4 displays the results of the simulation, which uses Table 5.3 parameters of initial SOC imbalance and charges the battery pack at a rate of 0.5C (120.25 A) which is half of the battery pack capacity (240.5 Ah). Figure 5.4(a) displays the SOC measurement for each module to compare with voltages of each module in Figure 5.4(b) verifies the approximation of SOC. At the end of charging, the residual SOC imbalance is 0.1%, compared to an initial difference of 80%. Figure 5.4(b) shows the trace of the voltages for each module and the controller is based on these voltage measurements. The bypass topology and voltage-based control is verified as the initial voltages results shows few high-voltage modules are bypassed while other modules are charging. The final voltage values ensure zero voltage residual imbalance.

The charging current profile shown in Figure 5.4(c) illustrates CCCV charger when one of the module voltages approaches its maximum voltage (25.2V), the charging current gradually decreasing at 5000 seconds. All the currents of individual modules are shown in Figure 5.4(d), explains when the module is bypassed its current goes to zero while the other modules receive the charging current and when all the modules' voltages are balanced with minimum residual imbalance (0.1V) after 5200 seconds, the balancing process is terminated, and every module receives the same charging current until the charging process is completed. The zoomed in graph in Figure 5.4(d) shows the current profile of individual module when bypassing and reconnecting.

Figure 5.4(e) displays the voltage of the battery pack, when the initial imbalance is higher during the battery charging process, five modules are bypassed to participate in the voltage balancing process. As the imbalance between the modules decreases, fewer bypass modules are used. It is challenging for the controller to determine which modules need to be bypassed

because of voltage fluctuations when the voltage imbalance is small between two modules. As the number of bypass modules varies, Figure 5.4(e) displays change in the voltage of the battery pack. The battery charge controller output is shown in Figure 5.4(f), which allows the charger supply voltage to be modified in response to change in the battery pack voltage. At the beginning of charging process, higher number of modules (five) are bypassed to offer quick balancing rather than bypassing only one module. To prevent the charger high voltage variation, the number of bypass modules and the balancing process activation can be adjusted. When the battery pack is 75% charged, the balancing procedure can be initiated. The charging process is stopped when all the module voltages reach its fully charged voltage (25.2 V) or one of the module voltages reaches its maximum voltage limit (25.8 V).

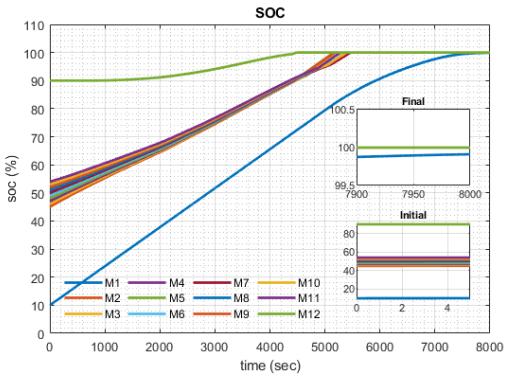

(a) SOC graph

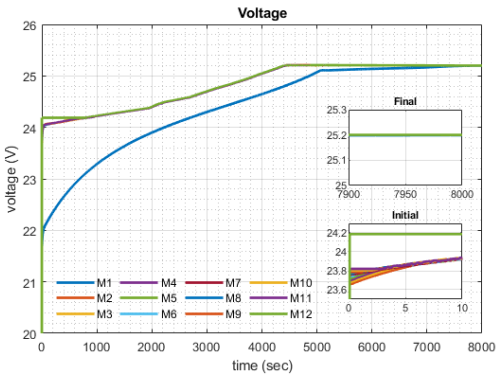

(b) voltage graph

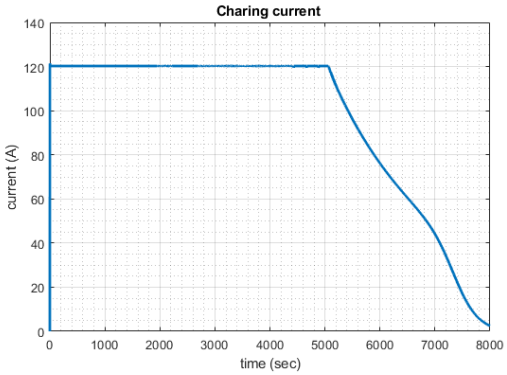

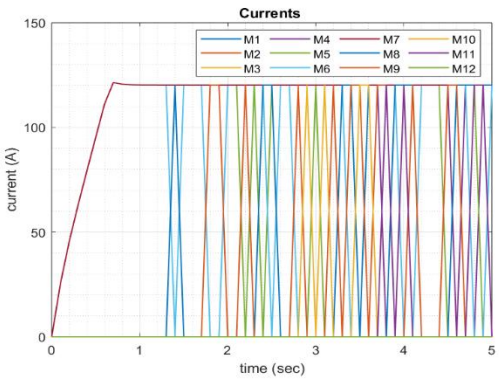

(c) charging current (0.5C-rate)

(d) individual modules currents

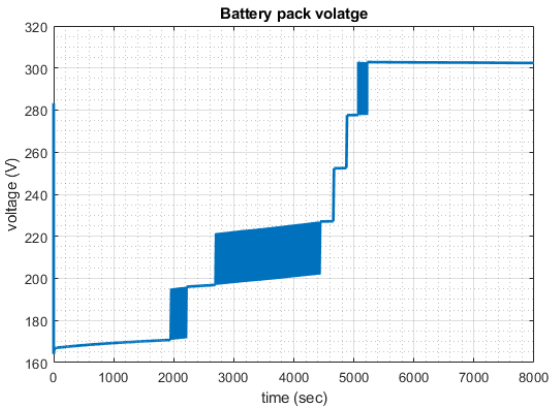

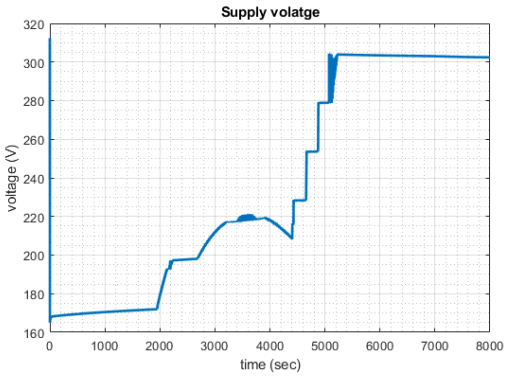

(e) battery pack voltage

(f) supply voltage

Figure 5. 4 Battery charging at 0.5C-rate with bypass cell balancing

Similarly, for 1C-rate (240.5 A) charging, which is equivalent to the battery pack capacity of 240.5 Ah, Figure 5.5(a, b) shows the simulation results of SOCs and voltages. The initial windows in Figure 5.5(a, b) show the initial SOC and voltage imbalance while the final windows show the residual imbalance at the end of charging. Figure 5.5(c) illustrates the charging current results that explain the 1C-rate (240.5 A) charging. The individual module currents are presented in Figure 5.5(d), while Figure 5.5(e, f) displays the supply and battery pack voltages. However, the results show the SOC/voltage balancing speed is increased due to higher charging and the battery pack is fully charge in 4500 seconds, as compared with the above 0.5C results.

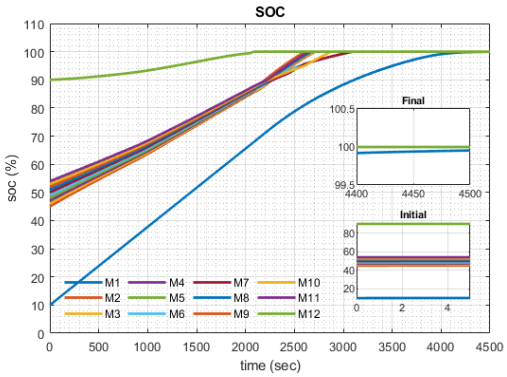

(a) soc graph

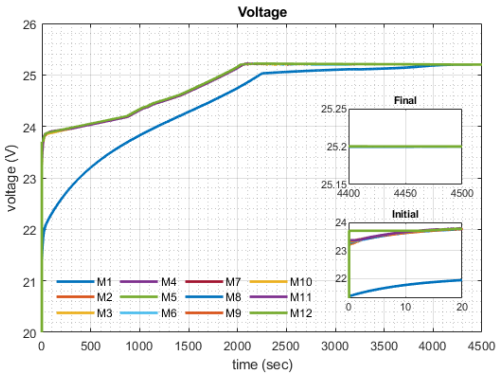

(b) voltage graph

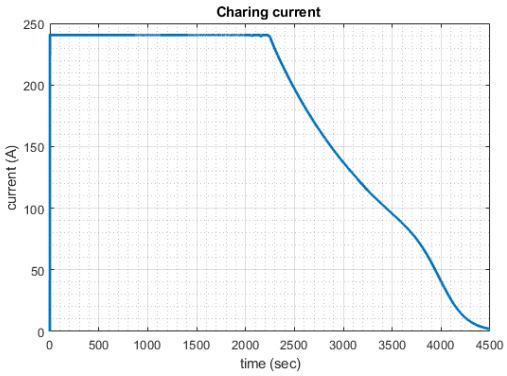

(c) charging current (1C-rate)

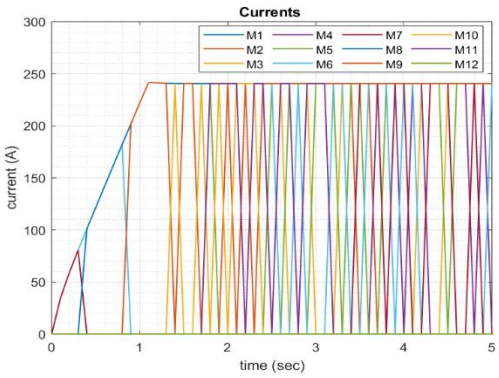

(d) individual modules currents

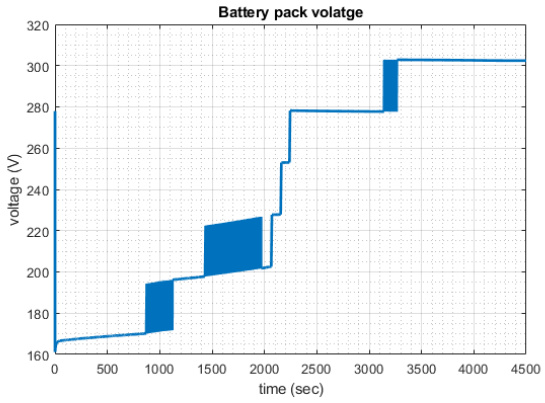

(e) battery pack voltage

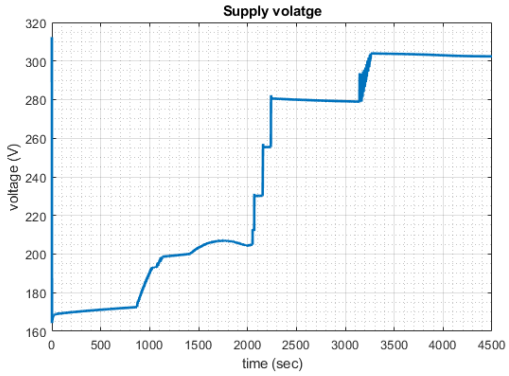

(f) supply voltage

Figure 5. 5 Battery charging at 1C-rate with bypass cell balancing

In a similar way Figure 5.6(a, b) illustrates the SOC and voltage simulation results for 2C-rate (481 A) charging, which is double the battery pack capacity (240.5 Ah). The initial SOC or voltage imbalance, and the SOC or voltage residual imbalance are expressed in the initial and final windows of Figure 5.6(a, b) respectively. The 2C-rate charging current profile is shown in Figure 5.6(c), the individual modules currents are presented in Figure 5.6(d), and Figure 5.6(e, f) displays the supply and battery pack voltages. Similarly, by increasing the balancing current up to 2C rate the battery pack is fully charged in 2000 seconds, which is 4 times faster than 0.5C.

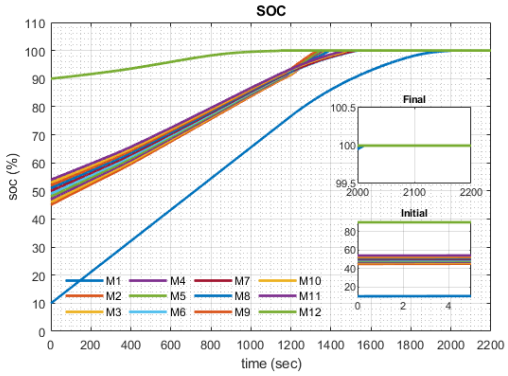

(a) soc graph

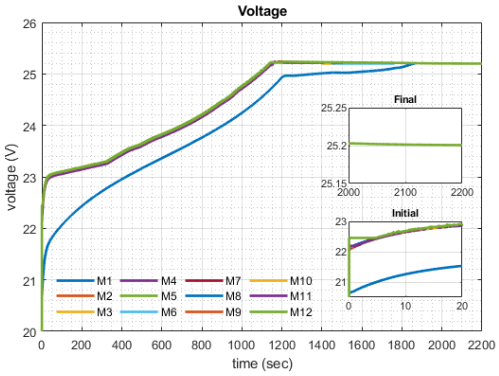

(b) voltage graph

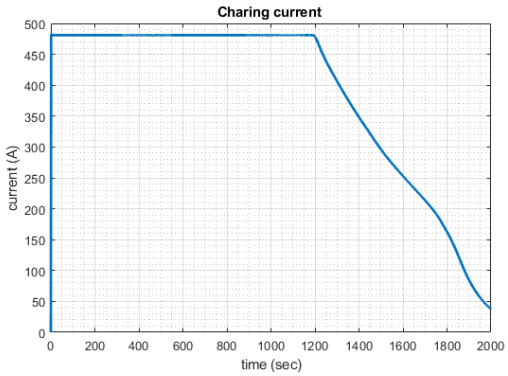

(c) charging current (2C-rate)

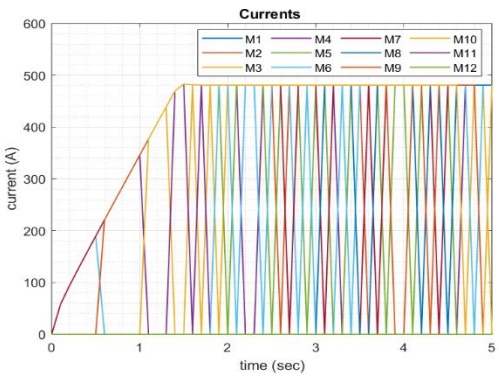

(d) individual modules currents

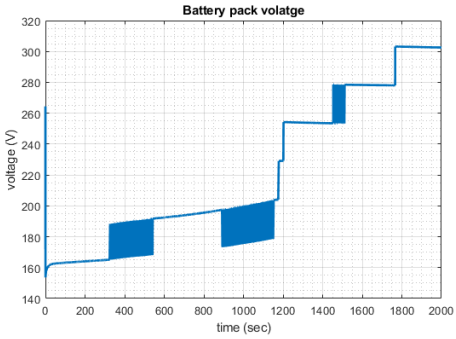

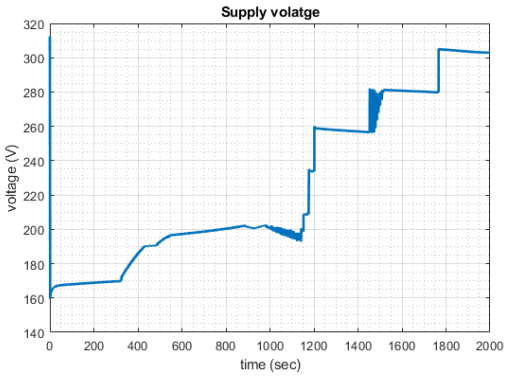

(e) battery pack voltage (f) supply voltage

Figure 5. 6 Battery charging at 2C-rate with bypass cell balancing

The proposed bypass method voltage/SOC balancing capability is verified by achieving approximately zero percent voltage/SOC residual imbalance for different C-rates (0.5C, 1C, 2C) at the end of charging.

5.4 Residual imbalance assessment of high voltage battery pack

To verify whether the proposed bypass balancing method is feasible for higher battery pack voltages and more series-connected cells. The 806.4V and 204.5Ah battery pack is created by connecting the 32 modules in series, with each module having a fully charged voltage of 25.2V. The initial SOC imbalance of the 30 modules increased by 0.5%, with the maximum initial SOC imbalance between the two modules being 80%. The simulation results for charging at 2C rate are illustrated in Figure 5.7. The SOCs and voltages of 32 modules are displayed in Figure 5.7(a, b), respectively. The initial SOC imbalance is 80% while the initial voltage imbalance is 2V between these modules. Figure 5.7(c) display the CCCV charging current profile where 2C rate (481A) current is provided in CC mode, while the current gradually diseases in the CV mode and the individual module current are presented in Figure 5.7(d) where the bypassed modules current goes to zero during balancing process. The battery pack voltage and the

charger supply voltage are presented in Figure 5.7(e, f), respectively. Here, the same controller strategy is used to bypass number of modules that is used for low voltage battery pack with a smaller number of modules which is tested in above section 5.3. high number of modules are bypassed when the voltage difference between modules is high while no module is bypass when the voltage imbalance is nearly zero. The proposed balancing topology achieved approximately zero residual imbalance verifies the feasibility of this method for a greater quantity of modules linked in series.

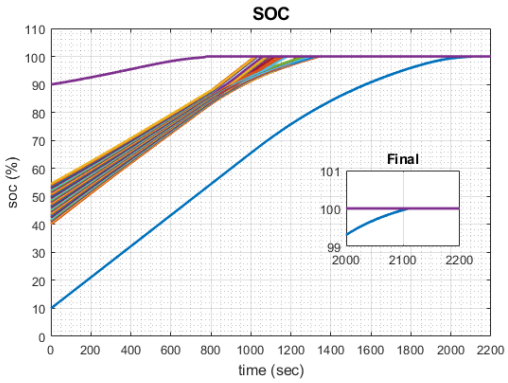

(a) soc graph

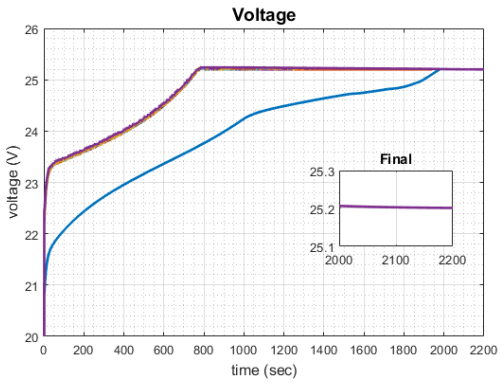

(b) voltage graph

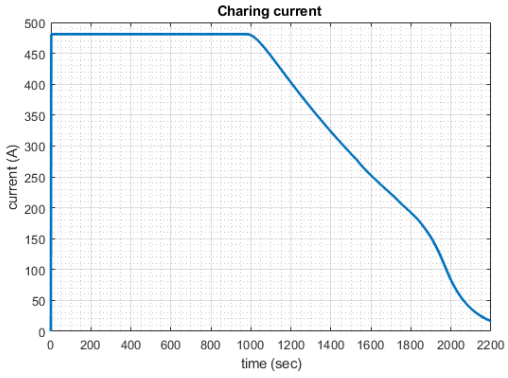

(c) charging current (2C-rate)

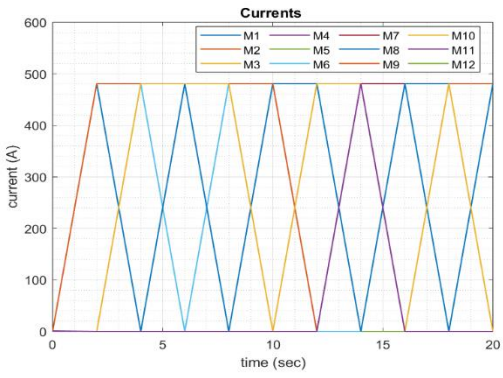

(d) individual modules currents

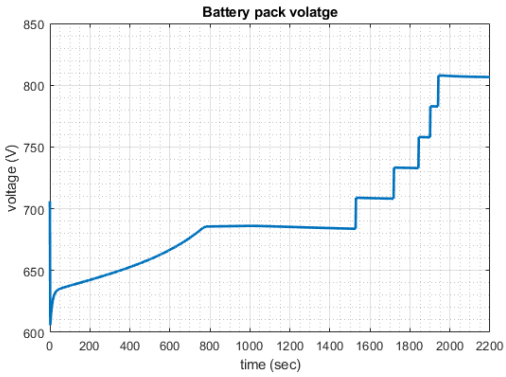

(e) battery pack voltage

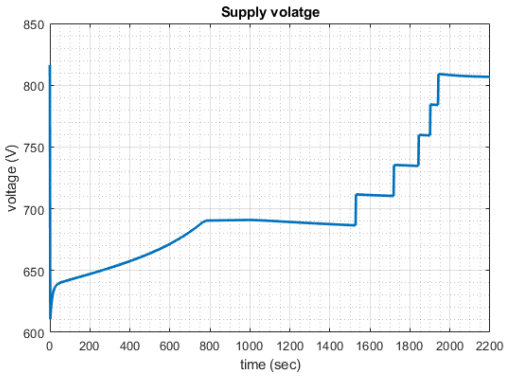

(f) supply voltage

Figure 5. 7 High voltage battery charging at 2C rate

5.5 Speed control validation

Step response testing is a useful technique to assess controller stability and dynamic performance. The system response to a sudden change in the reference input is indicated by the step response. The step response of the motor speed profile and modular battery pack voltage is displayed in Figure 5.8(b). The modular battery pack connected to the traction inverter provides variable DC-link voltage according to the motor speed, as in Figure 5.8(a). To offer a higher voltage, the battery pack links more modules in series as the speed increases. The fully charge battery pack voltage is 302.4 V, however, the set response is tested with initial SOC of all modules equal to 30% which gives the maximum voltage of battery pack is 265V. Figure 5.8(b) shows when the motor speed increases, the battery pack voltage provides maximum voltage by connecting all the modules in series. However, the battery pack voltage starts to decrease after 4 seconds because of battery pack discharge.

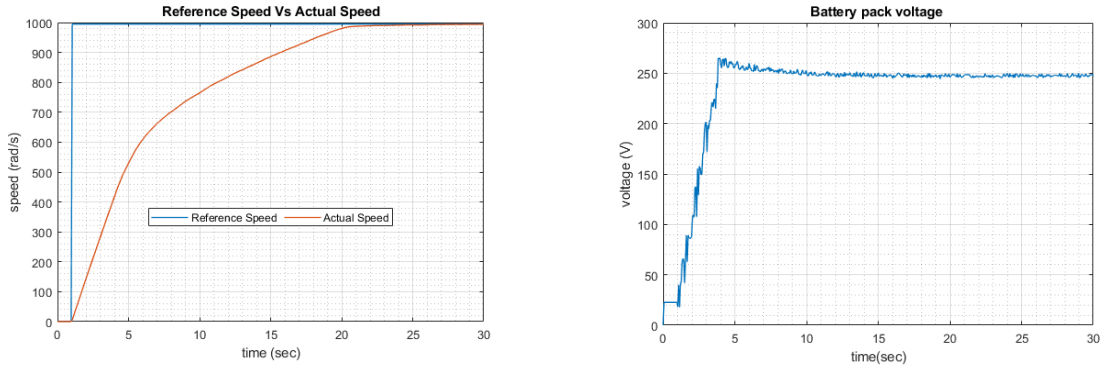

(a) Motor speed (b) Variable DC voltage

Figure 5. 8 Step response of motor speed profile and modular battery pack

5.6 Vehicle speed profile for variable discharge

A widely accepted standard for automobile testing is the Worldwide Harmonised Light Vehicle Test Procedure (WLTP). The purpose of the WLTP Class 3 (WLTP-3) drive cycle is to simulate real-world driving situations than the Class 1 and Class 2 testing cycles more closely. The WLTP-3 drive cycle was selected for the proposed cell balancing topology for battery discharge testing because of its capacity to replicate a wide range of realistic and diverse driving conditions. Standardised testing across the automobile industry is also made possible by this technique. The WLTP-3 drive cycle, depicted in Figure 5.9, has a more dynamic velocity/speed profile. It covers a 14.44 miles distance in 30 minutes with faster accelerations followed by quick braking. The WLTP-3 consists of four unique sub-parts, low (urban) at up to 35.1 mph, medium (suburban) at up to 47.6 mph, and high (rural) at up to 60.5 mph, extra-high (highway) at up to 81.5 mph. The WLTP-3 speed profile is depicted in Figures 5.9 (a) with speeds displayed in mph [157] and Figures 5.9 (b) represent simulation block of drive cycle to provide the reference speed for the EV motor.

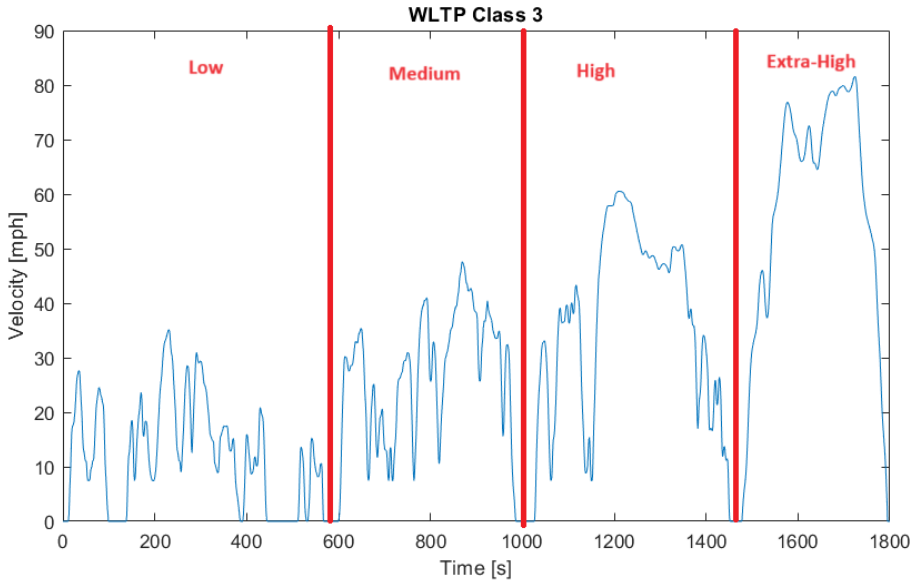

(a)

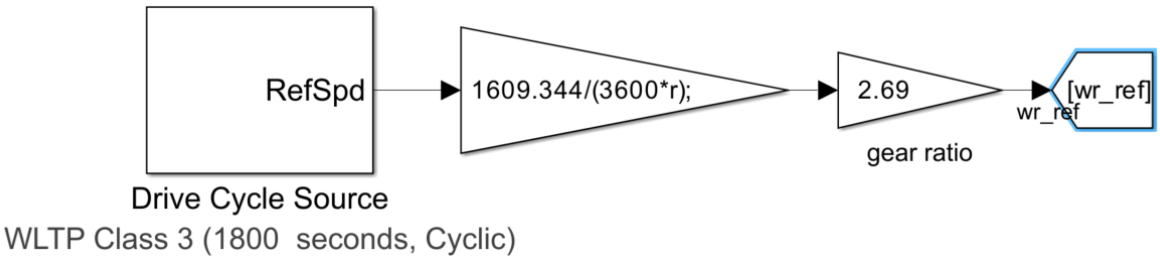

(b)

Figure 5. 9 WLTP-3 speed profile data and simulation block , adapted from [157]

Usually need to define a speed in radians per second (rad/s) in FOC which is why the WLTP-3 drive cycle speed profile is converted from miles per hour (mph) to rad/s by using the following formula. The radius of the wheel (*m*)is taken as 0.29 m.

$$Angular\ speed\ in\ rad/s = \frac{Linear\ speed\ (mph) \times 1609.34}{Radius\ of\ wheel\ (m)} \qquad (5.3)$$

Furthermore, the gear ratio needs to be multiplied with the vehicle speed to determine the induction motor speed required for the rotation of the shaft. Equation 5.2 can be used to determine the gear ratio in radians if the induction motor's maximum rotational speed is known. The maximum angular velocity of the induction motor is 994.83 rad/s (9500 rpm), the

maximum speed of the vehicle is considered as 200 mph (89.408 m/s), and radius of wheel (m) is taken as 0.2413 meters (diameter of the wheel is 19 inch). The calculation gives the gear ratio 2.69 radian which is used in this thesis.

$$Gear\ Ratio\ (\ radian) = \frac{max\ motor\ velocity\ (rad/s)}{max\ speed\ of\ vehivle\ \left(\frac{m}{s}\right)} \times\ Radius\ of\ wheel\ (m) \qquad (5.4)$$

5.7 Residual imbalance during variable discharging cycle

To check for residual imbalance between modular battery packs for discharging, the 30% maximum initial SOC imbalance is considered to reduce the testing period and to prove the concept of cell balancing. The individual module's initial SOC are presented in Table 5.5.

Table 5. 4 Cases with different initial SOC conditions for discharging

INITIAL SOC (%)	**M1**	**M2**	**M3**	**M4**	**M5**	**M6**	**M7**	**M8**	**M9**	**M10**	**M11**	**M12**
CASE: ONE HIGH ONE LOW OTHER DIFFERENT	10	20	21	22	23	24	25	26	27	28	29	40

To determine the SOC and voltage residual imbalance at the end of the discharge cycle, as well as to assess the effectiveness of the bypass balancing method, the battery pack is discharged with variable discharging rate using the WLTP-3 driving cycle. The variable speed of the motor provides real-world driving conditions with a flexible discharge rate. The controller is based on voltage values while SOCs are measured from the battery model in MATLAB Simulink.

Figure 5.10(a) shows the simulation results of individual modules SOCs. The measurement of SOC shows the voltage of Li-ion cells provides a good approximation of SOCs of the individual module. Figure 5.10(c) gives the SOC difference between series-connected modules that reduced from an initial 30% to 1% when the discharging cycle was completed. Each module's voltages are displayed in Figure 5.10(b), the constant voltages at the beginning of the discharge

profile confirm that the controller is based on voltage measurements. The voltage drop of individual module in Figure 5.10(b) is due to the sudden extreme acceleration and deceleration of the WLTP-3 speed profile. Figure 5.10(d) displays the voltage difference between the modules during the discharge operation. The battery module parameters are presented in chapter 3, section 3.2 shows fully charge voltage of individual modules is 25.2V. and the results shows 1% SOC, and the voltage residual imbalance is approximately 0% at the end of discharge.

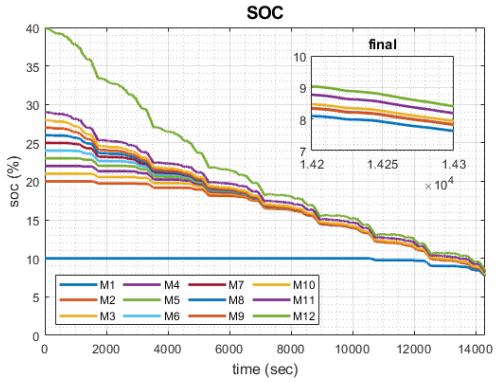

(a) soc graph

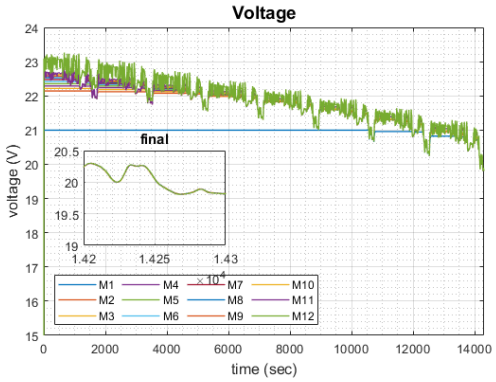

(b) voltage graph

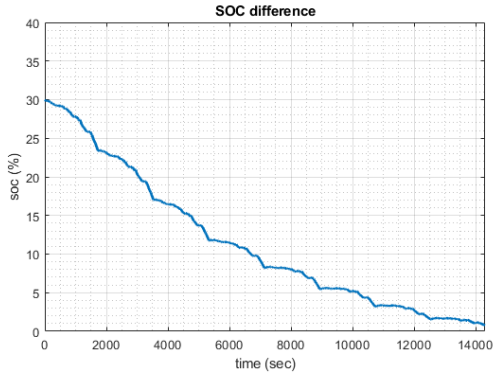

(c) soc difference

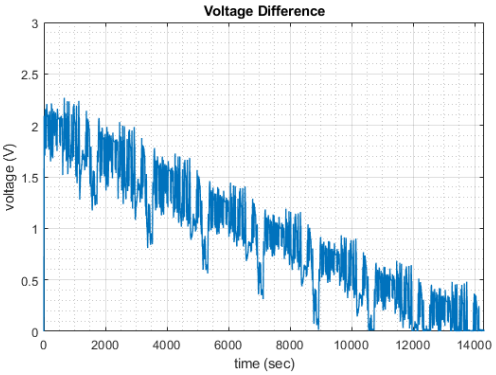

(d) voltage difference

Figure 5. 10 Battery discharging at variable load conditions

The simulation results in Figure 5.11(a) of the speed profile show that the motor speed follows the reference speed profile that shows the effectiveness of FOC for variable speed conditions. Figure 5.11(b) displays the battery pack voltage to confirm that the traction inverter's variable

DC-link supply voltage is aligned with the variable speed profile. When the speed increases the greater number of battery modules are connected in series to provide the required power.

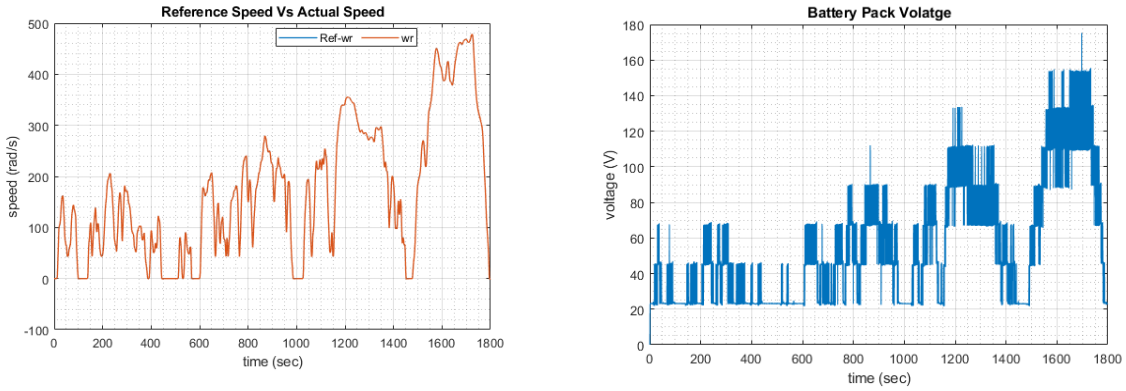

(a) Speed profile (b) Variable DC link voltage

Figure 5. 11 The speed profile and variable DC link simulation results

The results of modular battery packs achieved the SOC/voltage balancing by using bypass method as well as it provides variable DC-link voltage for the traction inverter according to the vehicle speed profile.

5.8 Cell balancing speed comparison

In literature it was difficult to compare the results of different balancing topologies, as each balancing topologies were tested for different characteristics of battery, charging, and discharging as well as the initial SOC/voltage was also different of each method. All these differences make it difficult to compare the balancing speed. However, an indicative balancing speed is calculated and compared. Thus, the proposed bypass method indicative balancing speed is 120, 60 and 30 minutes for 0.5C, 1C and 2C rates charging, respectively. The results in above section 5.7 also showed the same balancing time. The indicative balancing speed calculation and results for different charging C-rates, verifies the cell balancing time is directly proportional to the balancing current or C-rate. The bypass method utilizes higher balancing

current thus it produces faster balancing time as compared with the recent topologies mentioned in chapter 2, Table 2.3. The high balancing current also produce high power loss which is discussed in the next section.

In conclusion, this chapter provides detailed results and analysis of proposed modular battery pack during charging and discharging mode of operation. The results verify the effectiveness of controller and achieved minimum residual SOC/voltage imbalance. To verify the performance of proposed topology and controller design multiple tests are performed with different initial SOC/voltage conditions with different charging current for charging and discharging mode. The next chapter provide the power loss calculation for proposed topology to compare the traction inverter efficiency and show the advantage of using variable DC-link voltage.

Chapter 6: Power loss calculation and analysis

The power loss calculation and comparison has been presented in this chapter to shows the advantage of using variable DC-link voltage over fixed DC-link voltage for traction inverter. This chapter provides the procedure of power loss calculation for MOSFETS and IGBT. Both the conduction loss and switching loss of the individual device has been calculated. The results analysis of power loss between various cell balancing topologies is compared. The traction inverter power loss efficiency has also been calculated at the end of this chapter.

6.1 Power loss assessment at the battery pack level

The Infineon MOSFET (IAUA250N04S6N006) is considered for the battery power loss calculation due to its smaller value of internal resistance (0.64 mΩ) and highest current flow capability (250 Amps). The following formulas for calculating power loss are obtained from [158]. This power loss calculation method is applicable for all types of MOSFETS. However, if select any other device the results will be influenced by the internal resistance because the power loss is directly proportional to the internal resistance.

6.1.1 MOSFET Conduction Losses

When current flows through a conducting element, usually a semiconductor device like a transistor or diode, conduction losses occur. Conduction losses are mostly caused by the intrinsic resistance (R_{ds}) of the conducting material. A MOSFET's instantaneous conduction loss (P_{cM}) can be computed using equation 6.1.

$$P_{cM} = R_{ds} \times I_d^2 \qquad (6.1)$$

Where R_{ds} is on-state resistance and I_d is the on-state current.

Similarly, the diode instantaneous conduction losses P_{cD} can be calculated by:

$$P_{cD} = V_f \times I_F \tag{6.2}$$

Where V_f is the on-state zero-current forward voltage drop of a diode (0.8 V from the datasheet) and I_F forward current flowing through the diode that can be found from typical forward diode characteristics graph from the datasheet.

6.1.2 MOSFET Switching Losses

The switching losses of the MOSFET (P_{swM}) and the diode (P_{swD}) are determined by multiplying the ON and OFF sate switching energy by the switching frequency.

$$P_{swM} = (E_{onM} + E_{offM}) \ f_{sw} \tag{6.3}$$

Where E_{onM} is the energy loss during charging and turn ON state of the MOSFET, E_{offM} is the energy loss during discharging and turn OFF state the MOSFET and f_{sw} is the switching frequency.

The turn-on energy dissipation (E_{onM}) can be calculated using the formula:

$$E_{onM} = \frac{1}{2} V_{in}^2 \ C_{iss} \tag{6.4}$$

C_{iss} is the MOSFET input capacitance and V_{in} is the input voltage applied to the gate terminal for MOSFET.

The turn-off energy dissipation (E_{offM}) can be calculated using the formula:

$$E_{offM} = \frac{1}{2} (V_{in} - V_{out})^2 \ C_{oss} \tag{6.5}$$

C_{oss} is the MOSFET output capacitance and V_{out} is the output voltage at the MOSFET drain terminal.

Similarly, the diode switching loss P_{swD} is given by:

$$P_{swD} = (E_{onD} + E_{offD})\ f_{sw} \approx E_{onD}\ f_{sw} \qquad (6.6)$$

E_{onD} and E_{offD} is the diode energy loss during the MOSFET ON state and OFF state, respectively.

The energy dissipated during turn-on-state (E_{onD}) is revere-recovery energy can be calculated as:

$$E_{onD} = \frac{1}{4} Q_{rD}\ V_{rD} \qquad (6.7)$$

Where Q_{rD} is reverse recovery charge, and V_{rD} is reverse recovery voltage across diode.

6.1.3 MOSFET and Diode Total power loss

The total power losses of a MOSFET (P_{TM}) and Diode (P_{TD}) is a sum of conduction losses (P_{cM} , P_{cD}) and switching losses (P_{swM}, P_{swD}).

$$P_{TM} = P_{cM} + P_{swM} \qquad (6.8)$$

$$P_{TD} = P_{cD} + P_{swD} \qquad (6.9)$$

6.1.4 Proposed bypass topology total power loss

Since the frequency of the proposed bypass architecture is low (1-5 Hz), the MOSFET and diode switching losses are negligible. Since the MOSFET internal resistance is so low (0.64

mΩ), the diode voltage is less than the conduction voltage of 0.8V, indicating that the diode conduction loss can also be ignored. Therefore, the total power loss (P_{Bloss}) at the battery pack level is only due to the MOSFET conduction loss.

$$P_{Bloss} = P_{cM} \tag{6.10}$$

Figure 6.1 displays the total power loss of a single MOSFET as a function of charging or discharging current flowing through the MOSFET that produces condition loss. The maximum power loss of a single MOSFET for a 2C-rate battery current is 0.15 kW.

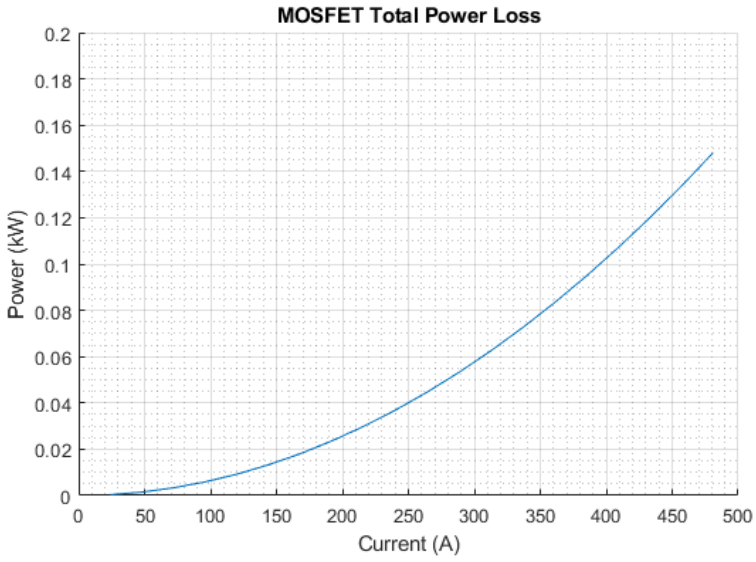

Figure 6. 1 Single MOSFET total power loss

The generic formula for calculating total power loss (P_{TBloss}) at the battery pack level for the proposed bypass balancing method can be expressed as:

$$P_{TBloss} = N \times P_{Bloss} \tag{6.11}$$

where *N* is the battery pack's total number of series-connected cells or modules.

The proposed bypass topology uses two MOSFETs per module but only one of them will be conducting at any time while the other will be off, so only 12 MOSFETs contribute to the total

power loss at the battery pack level. Figure 5.13 displays the overall power loss at the battery pack level and is calculated considering variable charging or discharging current. The vertical axis of the graph Figure 6.2 shows the power loss dissipation in kW (kilo Watt) and the horizontal axes show the multiple C-rate (0.1C to 2C-rate) of the battery pack, since the 240.5Ah total capacity battery pack is utilised in this thesis. The maximum power loss of 12 MOSFETS for a 2C-rate battery current is 1.78 kW.

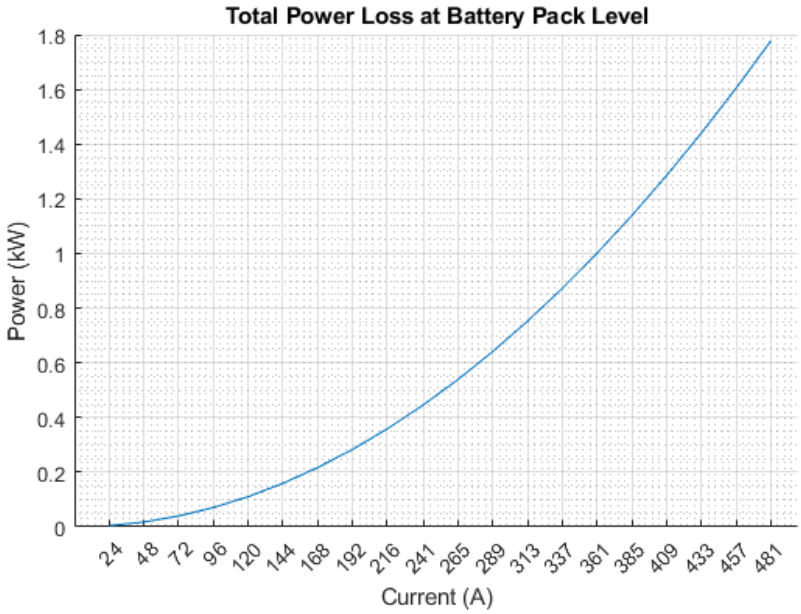

Figure 6. 2 Total power loss at the battery pack level

6.1.5 Other balancing topologies power loss

Only consider the number of MOSFETs to compare the power loss with other cell balancing topologies and neglect the power loss of other components used in these topologies. The number of switches used by different topologies was presented in Chapter 2, section 2.6, Table 2.2. Assuming the battery pack is configured in the same 12S1P configuration, Table 6.1 shows the number of switches (MOSFETs) required for other balancing topologies.

Table 6. 1 Number of switches for other balancing topologies for 12S1P

Cell balancing Topologies	**No. of Switches**	**No. of switches for 12S1P**
Single inductor (SI)	2n+2	26
Coupled inductor (CI)	2n-2	22
Single transformer (ST)	2n+2	26
Multiple transformers (MT)	n	12
Multi winding transformer (MWT)	n+1	13
Single switched capacitor (SWT)	n+5	17
Multiple switched capacitor (MSC)	2n	24
Buck-boost converter (BBC)	2n	24
Quasi-resonant converter (QRC)	2n-2	22
Ramp converter (RC)	n	12
Full bridge converter (FBC)	4n	48

Other cell balancing topologies consider a range of cell balancing current and switching frequencies. Thus, the total power loss was calculated considering different ranges of balancing current (1A to 50A) and switching frequencies (1kHz to 50kHz). The results show switching frequencies less while balancing current have more contribution in the power loss. Furthermore, these topologies require different the number of switches minimum 12 to maximum 48 for the proposed 12S1P configuration. Thus, the total power loss is calculated for minimum and maximum number of switches. The total power loss for proposed bypass topology is calculated only due to MOSFET conduction loss, however, the total power loss for other topologies is considered as the MOSFET's total conduction loss plus switching loss, illustrated in Figure 6.3. The power loss for 12 MOSFETs is shown in Figure 6.3(a) with the maximum power loss of 19W, and Figure 6.3(b) illustrates power loss for 48 MOSFETs with maximum 78W power loss.

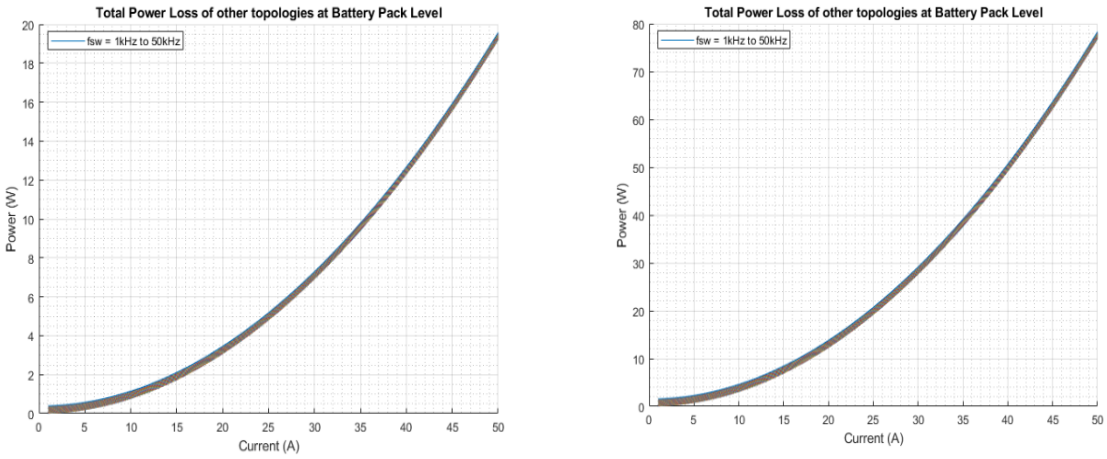

(a) 12 MOSFET (b) 48 MOSFETs

Figure 6. 3 Total power loss of other cell balancing topologies at battery pack level

6.2 Power loss assessment at the electrical drive level

The formulas for calculating the traction inverter total power loss are obtained from the ABB application note for two-level inverters. The formulas used for conduction and switching power loss calculation for IGBT module are adapted from [159]. The Infineon IGBT module (FF1400R12IP4) is considered for the power loss calculation of a two-level inverter. This method of calculating power loss can be applied to any IGBT module. However, the internal resistance of the module will affect the power loss proportionally.

6.2.1 IGBT Conduction Loss

The IGBT conducts during just a half-period, hence the conduction losses are determined by

$$P_{cigbt} = \frac{1}{2}\left(V_{CE0} \cdot \frac{I}{\pi} + r_{CE} \cdot \frac{I^2}{4}\right) + m \cdot \cos\,\phi \cdot \left(V_{CE0} \cdot \frac{I}{8} + \frac{1}{3\pi} \cdot r_{CE} \cdot I^2\right) \qquad (6.12)$$

Where V_{CE0} is collector-emitter on-state voltage and r_{CE} collector-emitter resistance can be calculated from the graphical data of IGBT output characteristics (on-state voltage as a function of collector current) from the datasheet.

$$r_{CE} = \frac{V_{CE02} - V_{CE01}}{I_{C2} - I_{C1}} \quad (6.13)$$

$$V_{CE0} = V_{CE02} - (I_{C2} \times r_{CE}) \quad (6.14)$$

Where I_{C2} , I_{C1} are collector currents and V_{CE02} , V_{CE01} collector-emitter on-state voltages.

The modulation index m can be calculated as:

$$V_{outpk} = 0.5 \times V_{DCmin} \quad (6.15)$$

$$m = \frac{V_{outpk}}{0.5 \times V_{DCmax}} \quad (6.16)$$

Where V_{DCmin} is minimum and V_{DCmax} is maximum voltage of the battery pack.

6.2.2 IGBT Switching loss

The IGBT total switching losses is the sum of ON and OFF state energy dissipation.

$$E_{sw} = E_{on} + E_{off} \quad (6.17)$$

A polynomial approximation function of IGBT switching losses can be used to represent the measured ON and OFF state energy. It is also necessary to consider how the switching energy depends on the DC voltage because the proposed modular battery packs provide the variable DC-link voltage. As a result, the switching losses with switching frequency and phase-current:

$$P_{swigbt} = f_{sw} \cdot \left(\frac{a}{2} + \frac{b \cdot I}{\pi} + \frac{c \cdot I^2}{4}\right) \cdot \frac{V_{DC}}{V_{\text{nom}}} \qquad (6.18)$$

Where *a, b* and *c* are the sum of coefficients of on-state and off-state energy in the switching process and can be calculated from datasheet graphical data of IGBT of switching energies as a function of collector current and V_{DC} is the battery pack voltage and V_{nom} is the nominal voltage.

6.2.3 Diode conduction loss

The diode conduction losses can be found in a similar manner to the IGBT conduction losses. The freewheeling diode conducts when the IGBT is turned off, hence, the diode conduction loss can be calculated as:

$$P_{cdiode} = \frac{1}{2}\left(V_{F0} \cdot \frac{I}{\pi} + r_T \cdot \frac{I^2}{4}\right) - m \cdot \cos\,\phi \cdot \left(V_{F0} \cdot \frac{I}{8} + \frac{1}{3\pi} \cdot r_T \cdot I^2\right) \qquad (6.19)$$

Where V_{F0} is the on-state diode voltage and r_T is resistance can be calculated from the diode on-state voltage as a function of forward current from the datasheet. The load (motor) power factor ($\cos\,\phi$) is considered as 0.88 and the modulation index (m) can be computed using equation (5.22).

$$m = \frac{V_{outpk}}{0.5 \times V_{DCmax}} \qquad (6.20)$$

Where the peak output voltage is V_{outpk} and V_{DCmax} is the maximum voltage of the battery pack.

$$r_T = \frac{V_{\mathrm{D02}} - V_{\mathrm{D01}}}{I_{F2} - I_{F1}} \quad (6.21)$$

$$V_{CE0} = V_{D02} - (I_{F2} \times r_T) \quad (6.22)$$

Where I_{F2} , I_{F1} are diode forward currents and V_{D02} , V_{D01} diode on-state voltages.

6.2.4 Diode Recovery Loss

The recovery losses can be expressed as a polynomial approximation function of diode switching losses with DC voltage (V_{DC}), phase-current, and switching frequency. When it comes to the diode power loss, only the recovery energy is important, and the turn-on energy can be ignored.

$$P_{rec} = f_{sw} \cdot \left(\frac{a}{2} + \frac{b \cdot I}{\pi} + \frac{c \cdot I^2}{4}\right) \cdot \frac{V_{DC}}{V_{\mathrm{nom}}} \quad (6.23)$$

where $a\ b\ and\ c$ are the coefficients of turn-off energy of the diode during the recovery process and can be calculated from datasheet graphical data of diode energy as a function of forward current and battery pack voltage is V_{DC} and V_{nom} is nominal voltage.

The IGBT total power loss (P_{IGBT}) is:

$$P_{IGBT} = P_{cigbt} + P_{swigbt} \quad (6.24)$$

Similarly, the diode total power loss (P_{Diode}) is:

$$P_{Diode} = P_{cdiode} + P_{rec} \quad (6.25)$$

The total power loss of a single IGBT and Diode is:

$$P_{Totalloss} = P_{Diode} + P_{IGBT} \quad (6.26)$$

6.2.5 Proposed modular battery pack total power loss

The three-phase two-level inverter consists of six IGBTs and freewheeling Diodes, therefore the total power loss is multiplied by a factor of 6 to get the total power loss of the traction inverter.

$$P_{lossinverter} = 6 \times P_{Totalloss} \quad (6.27)$$

Figure 6.4 displays the total power loss at the electrical drive level with a constant switching frequency of 5 kHz and a variable discharge current. According to the analysis of results, the power loss is less when using a variable DC-link voltage rather than when using a fixed DC-link voltage, where the fully charged battery pack voltage is 302.4V. The results presented in Figure 6.4 demonstrate that the traction inverter's maximum power loss at a 2C-rate discharging current is 5.8 kW with a fixed DC link voltage of 302.4V, but for the higher EV battery pack voltages the power loss will increase almost linearly as presented in Figure 6.5. The power loss results in Figure 6.5 displays, the maximum power loss is 9.19 kW and 32.53 kW with 400V and 800V fixed DC voltage at 2C-rate discharging current, respectively.

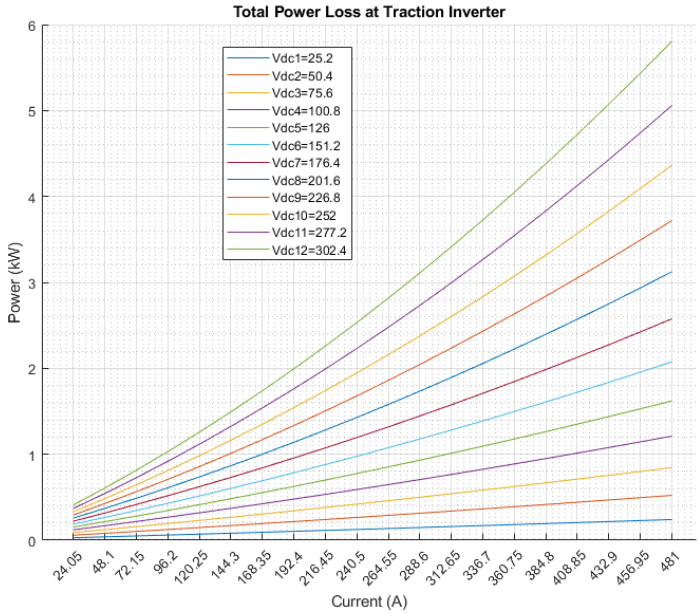

Figure 6. 4 Total Power Loss at Traction Inverter at variable DC-link voltage

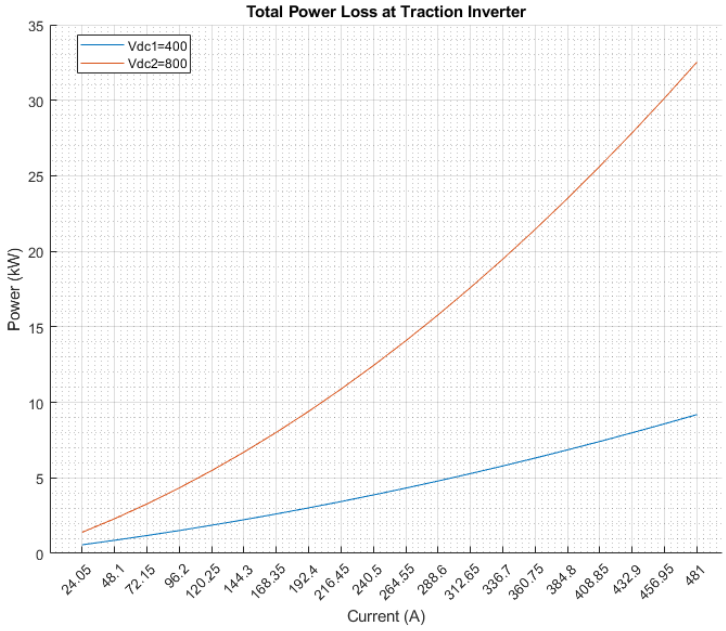

Figure 6. 5 Traction inverter total power loss at fixed DC-link voltage

To assess the inverter's performance under various operating conditions, the total power loss of a two-level inverter with variable switching frequency (typically from 5.5 to 6.5 kHz) and fixed DC link voltage of 302.4V is calculated as shown in Figure 6.6. The higher switching

frequencies typically produce lower output voltage distortion, but leads to an increase in switching losses, hence overall inverter power losses. The graphs in Figure 6.6 show the maximum power loss of the inverter at 2C rate with variable current is 5.98 kW and 6.35 kW for switching frequencies of 5.5 kHz and 6.5 kHz, respectively.

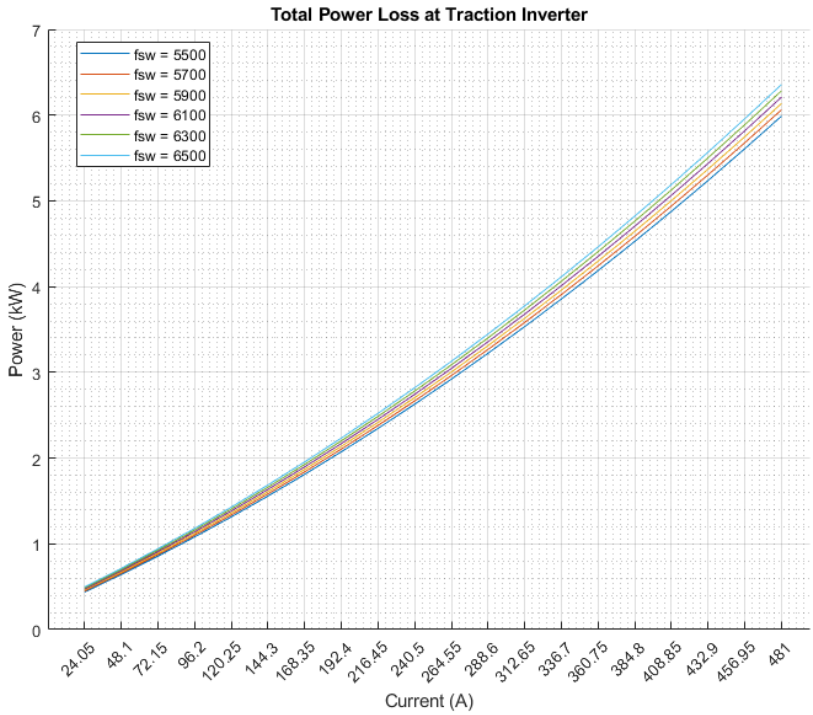

Figure 6. 6 Traction inverter power loss at variable switching frequency

It is clear from the traction inverter's power loss analysis that the variable DC link will result in reduced losses when compared to the fixed DC-link. Since the speed of an EV varies and the speed limit is typically low in cities, the high DC-link voltage is not always necessary. The employment of bypass topology can minimize power loss and provide cell balancing.

The summary of power loss calculation presented in Figure 6.7 the proposed bypass topology drawback is to produce higher power loss compared with any other cell balancing topologies at battery pack level. However, it reduces the overall power loss by reducing the power loss at the traction inverter level. Considering the maximum power loss of proposed bypass topology for

481 A balancing current and 12 MOSFETs is 1.78 kW, and maximum power loss of other topologies with 50 A balancing current and 12 MOSFETs is 19W. So, the proposed bypass topology produces 1.75 kW higher power loss then other balancing topologies at battery pack level or during charging mode. However, the power loss at fixed DC-link with maximum discharge current of 481 A is 5.8 kW but using variable DC-link voltage is 2.6 kW for bypassing 5 modules. Therefore, the proposed modular battery pack can reduce 3.2 kW power at traction inverter by providing variable DC-link. Overall, by combining the power loss at battery pack level and traction inverter level, the proposed method achieved to reduce 1.45 kW power loss. Thus, power loss is reduced by 25% by using bypass topology.

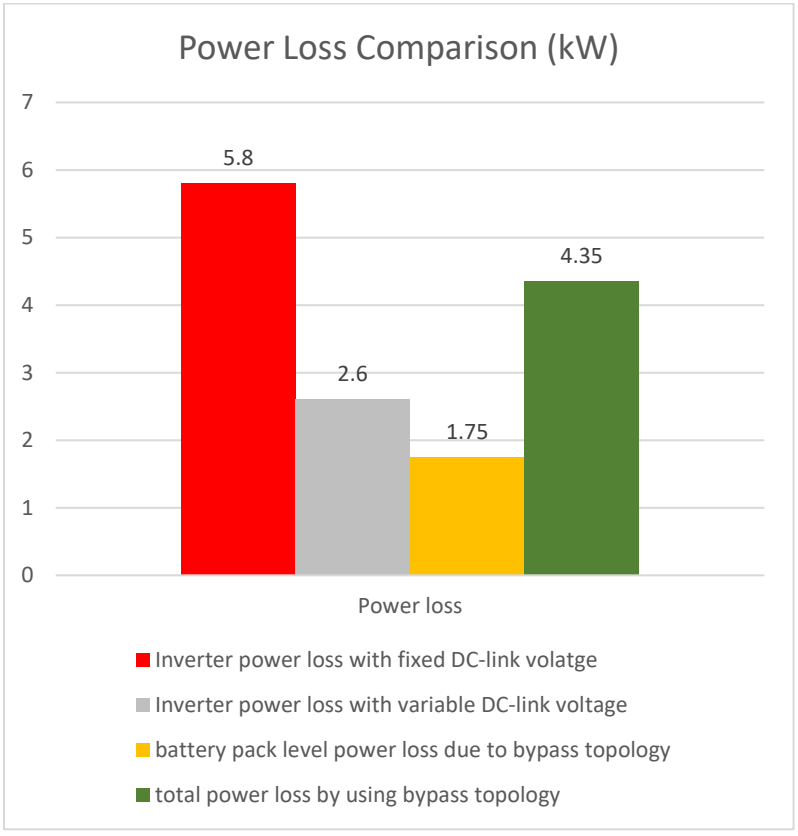

Figure 6. 7 Power loss comparison between fixed and variable DC-link voltage

6.3 Power efficiency of traction inverter

The power efficiency of a traction inverter ($\eta_{inverter}$) is commonly represented as the ratio of input power (P_{in}) to output power (P_{out}), when considering power losses. The power efficiency formula is provided by

$$\eta_{inverter} = \frac{P_{out}}{P_{in}} \times 100 \qquad (6.28)$$

When the traction inverter power loss ($P_{Tinverter}$) and battery pack power is known, then the output power of inverter (P_{out}) can be calculated as

$$P_{out} = P_{in} - P_{lossinverter} \qquad (6.29)$$

Where battery pack energy or power is 72.8 kWh calculated and mentioned in chapter 3, section 3.2, Table 3.3. The battery pack discharging rate is variable due to variable speed of the vehicle using the WLTP-3 speed profile as shown in section 5.5, Figure 5.13 and 5.14, but considering the average discharge current of the battery pack is approximately 216A which is 0.9C-rate (1.11 hours) for power efficiency calculation. Then, the battery pack can ideally provide 65.6 kW (kWh/h) input power (P_{in}) for 1.11 hours. The inverter total power loss is calculated in above section 5.8.5 that shows power loss of fixed Dc-link is 2.25 kW and variable DC-link is 1 kW when bypassing 5 modules at 0.9C-rate discharge. The discharging battery pack results in section 5.6, Figure 5.14(b) justifies that a maximum of seven modules are needed to provide the necessary DC-link voltage for the WLTP-3 drive cycle. Thus, by using equation 5.31, P_{out} is 63.3 kW and 64.6 kW for fixed and variable DC-link, respectively. Furthermore, the traction inverter efficiency can be calculated by equation 6.28, which shows 96.5% for fixed DC-link and 98.5% for variable DC-link. Hence, the traction inverter power efficiency is improved by 2% using modular battery packs in EVs.

In summary this chapter calculated the power loss and compare between proposed and other cell balancing topologies. It also verifies the improvement in traction inverter efficiency by providing variable DC-link.

Chapter 7: Experimental verification with Hardware in the loop

This chapter explains how the proposed balancing topology and modular battery pack is implemented in the HIL environment to validate the simulation results through experimentation. A battery pack module`s voltage balance during charging and discharging, and variable DC-link for traction inverter is the focus of the experimental results.

7.1 Implementation of proposed method in HIL

The HIL is categorised into two parts, real-time simulator (computer) and hardware. A real-time simulator which is a software-based system includes a model of the battery cell, EV battery pack with bypass topology, DC charger, battery charge controller, three-phase induction motor model, FOC, three-phase inverter, and PWM generator for the inverter. The hardware part contains the real TI microcontroller, interface board (operational amplifier), and OPAL-RT (real-time system hardware machine). The block diagrams in Figures 7.1 and 7.2, depict the HIL arrangement for charging and discharging EV battery packs, respectively.

The real-time simulator part for the charging and discharging both are explained in detail in Chapter 4. In the hardware part during charging the OPAL-RT continuously monitors the individual module voltages and sends it to the microcontroller through an Analog output board. The microcontroller performs tasks according to the embedded code adjusts the switching control signals for the proposed bypass topology and sends it to the OPAL-RT through an interface board. The OPAL-RT receive the switching control signals through a Digital input board. The hardware design for discharging is the same as for charging but the only difference

is that OPAL-RT receives one extra voltage amplitude signal, and the microcontroller embedded code is changed.

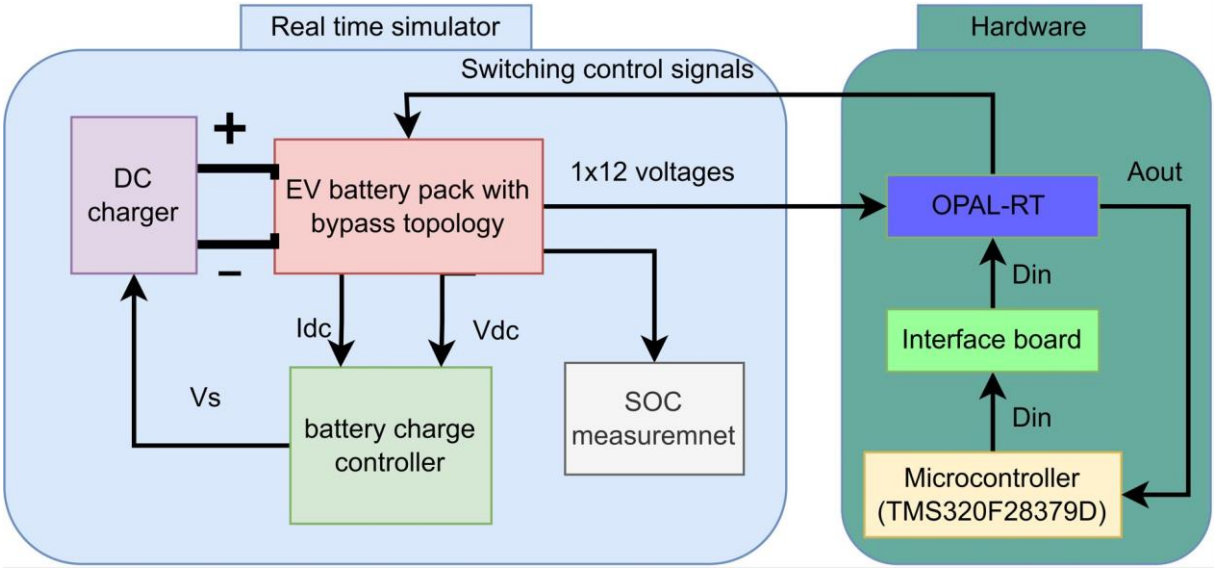

Figure 7. 1 HIL setup for EV battery charging

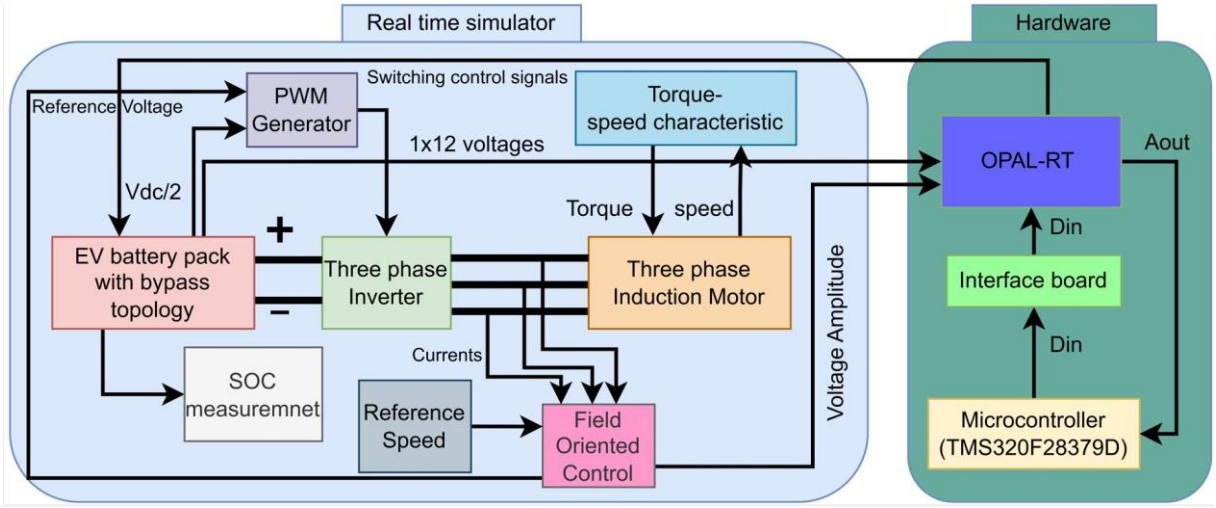

Figure 7. 2 HIL setup for EV battery discharging

Figure 7.3 shows photos of the laboratory setting used for the experiment. The proposed system has been developed on a lab Computer that is connected via an Ethernet connection to the OPAL-RT front. The TI microcontroller is connected to the OPAL-RT's backside Analog output. After that, an interface board is linked to the microcontroller's digital output to raise the

voltage, and it is connected to the OPAL-RT's digital input on the back side for controlling the switching signals inside OPAL-RT software, one of which is visible through an oscilloscope.

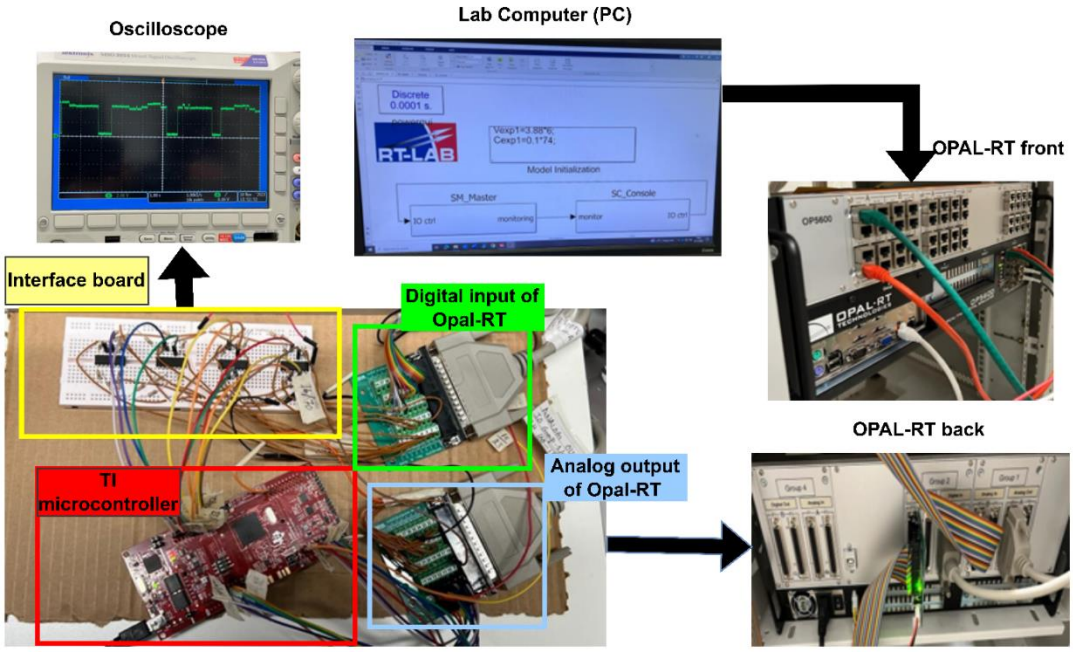

Figure 7. 3 Experimental setup in laboratory

7.2 OPAL-RT and microcontroller interface board

The microcontroller's maximum output voltage is 3.3V, but OPAL-RT's digital input voltage ranges from 4 V to 50 V. As a result, the microcontroller and OPAL-RT cannot be directly connected. Instead, an interface board is needed to increase the voltage of the microcontroller's digital output signal above 4 V. An interface board is designed using a simple circuit consisting of a non-inverting Op-Amp configured with a gain of two, such that the input and output voltages are in phase, but the amplitude becomes twice as large as the input value. In this thesis, four Op-Amp ICs (LM324N) are used to design the interface board as it consists of 4 Op-Amps. In Figure 7.4, the fundamental non-inverting Op-Amp circuit is displayed.

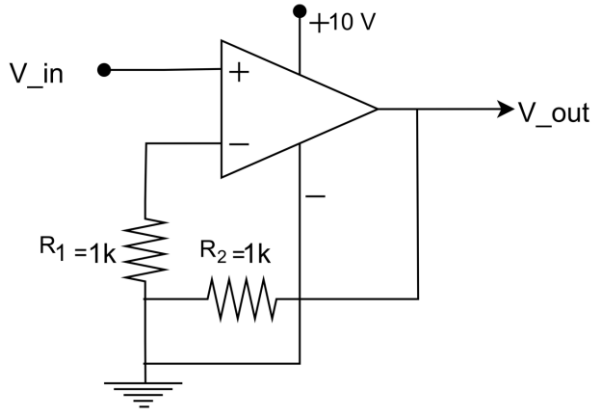

Figure 7. 4 Basic circuit diagram of non-inverting Op-Amps

where the input voltage is V_{in} applied to the positive terminal, the output voltage is V_{out}, $R_1$is the feedback resistor connected between inverting terminal and output, $R_2$is the resistor between inverting terminal and ground, and 10 V supply voltage is provided. The supply voltage should be above the necessary output voltage (above 4 V) but below the Op-Amp's maximum limit (28 V). The voltage gain of Op-Amp is 2 by using the same value of resistor, R_1 and R_2. The voltage gain (G) of a non-inverting amplifier can be calculated as:

$$G = 1 + \frac{R_2}{R_1} \qquad (7.1)$$

The microcontroller provides 12 digital output signals to the OPAL-RT, which is further split into 12 complementary digital signals using the NOT gate inside the OPAL-RT software to control 24 MOSFETs.

7.3 Modelling state-of-the-art system in OPAL-RT

The OPAL-RT system is based on MATLAB Simulink to build a model. However, it also includes it's on library in MATLAB Simulink to provide necessary blocks for the configuration of its input/output card and to make the model compatible with its system for real-time application. It also provides the blocks to record data in real-time. Overview of the OPAL-RT

software is shown in the Figure 7.5 called the RT-LAB. To start working with RT-LAB, first a new project is created (BMS_2022) and added multiple models inside the same project for different type of testing scenarios (charging or discharging of the battery pack). The edit option is used to open the model in MATLAB Simulink.

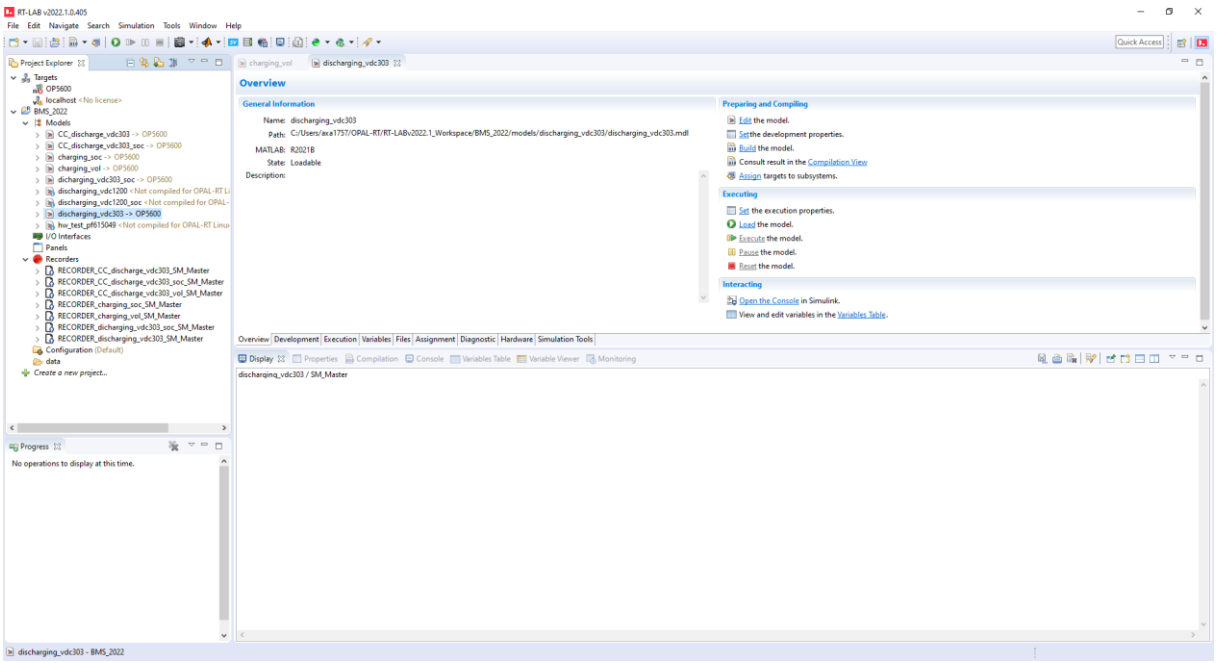

Figure 7. 5 OPAL-RT software screenshot

The MATLAB Simulink file is open to start building the model, however before adding the model in RT-LAB, the OPAL-RT input/out cards and necessary configuration is done by using the OPAL-RT library blocks. The whole model is created into two blocks SM_Master and SC_Console as presented in Figure 7.6. The SM_Master block is used for modelling (controller and proposed system) and configuration of the OPAL-RT hardware. However, the SC_Console block is used for monitoring of the signals as well as control in real time changes. The model initialisation block is used for the variables initialisation as can be seen by the name of the block.

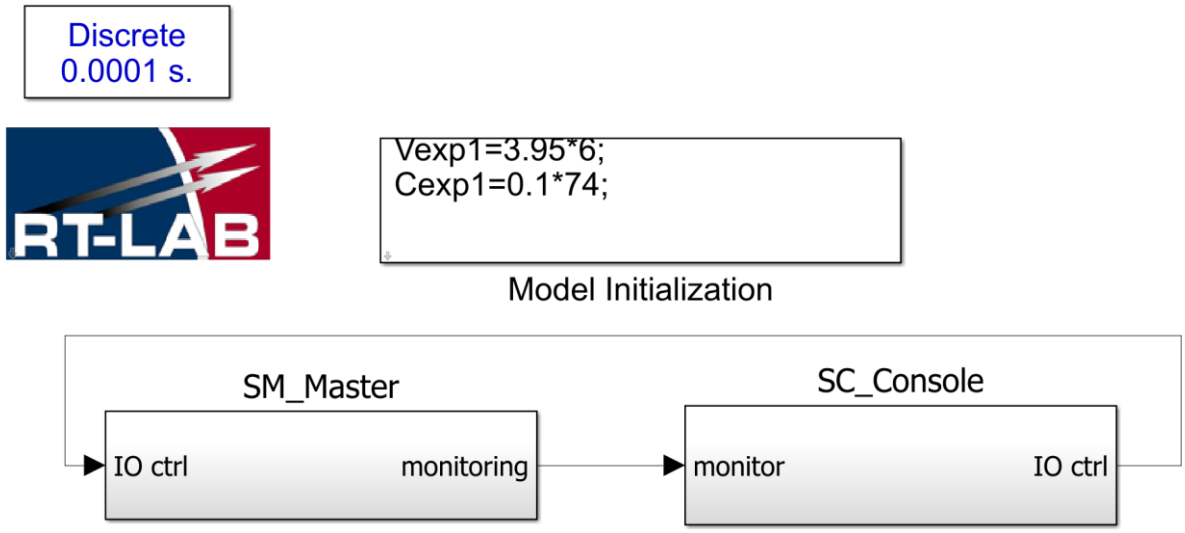

Figure 7. 6 OPAL-RT configuration and bypass topology implementation during charging

The SM_Master is further represented in Figure 7.7(a,b), which includes all the basic configuration of the I/O cards and system configuration blocks (OpCtrl, Opcomm, Dout type config, overruns). The OpwriteFile block is used for the data recoding in real time from OPAL-RT. However, the only difference in both figures (a, b) is the addition of charging and discharging modelling and control. The charging and discharging circuit and control are explained in chapter 4, section 4.2 and 4.3. Thus, any MATLAB Simulink model can be added in SM_Master block for real time testing after configuration. The configuration blocks are presented in Appendix B.

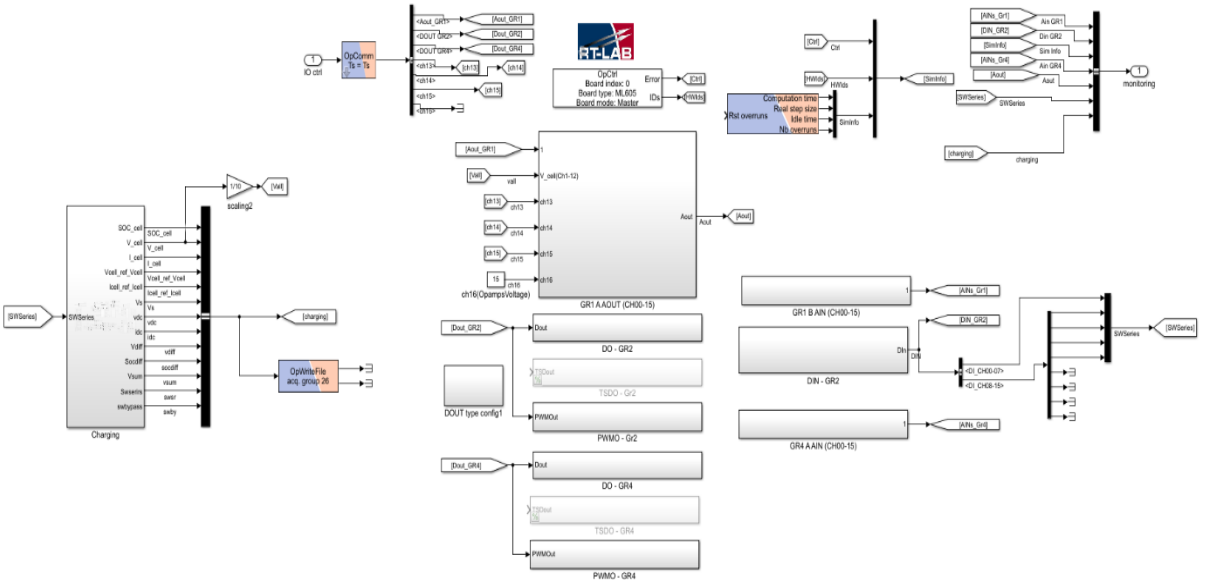

(a)

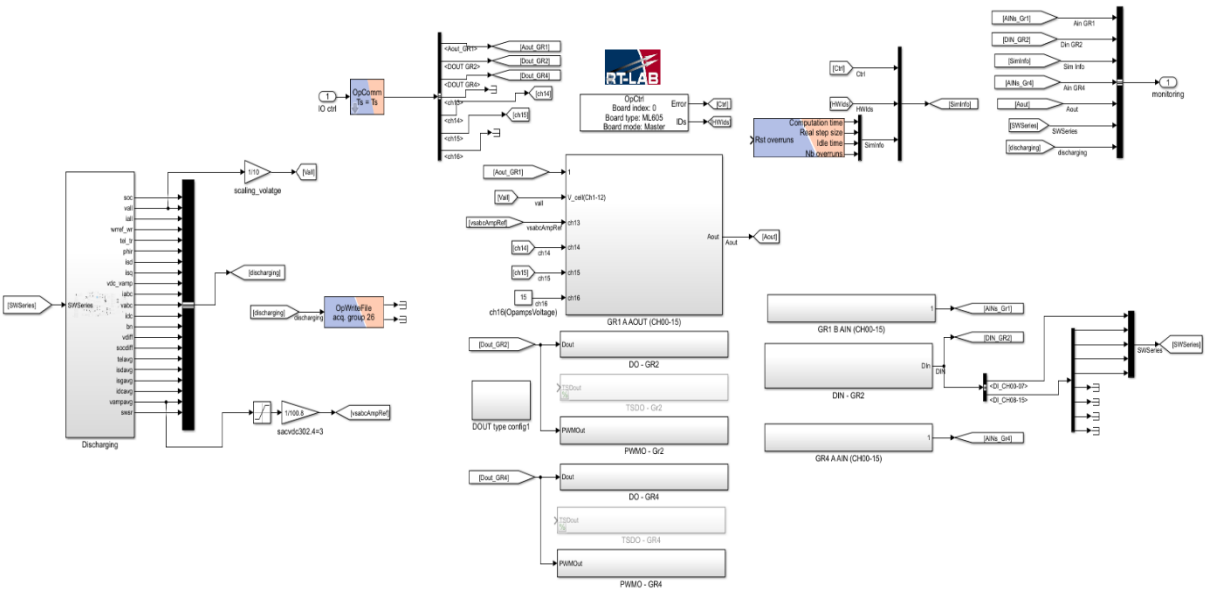

(b)

Figure 7. 7 Modelling and controller design (SM_Master)

The SC_Console block is shown in Figure 7.8, which monitors the user define signal and the status of real time singles. The timing value shows the total computation time required for the OPAL_RT microprocess to execute the model in real time. If the model is too complex and the sampling time is not enough to execute the model in real time, then it will show the overruns. The overrun helps to decide the optimal sampling time required for the model to run in real time, if the overruns increase with time during testing it means the signal results overlaps with each other. Thus, the sampling time needs to be chosen according to the model complexity to run in real time and do not produce overruns. The sampling time used for the testing proposed state-of-the-art system is 60 microseconds.

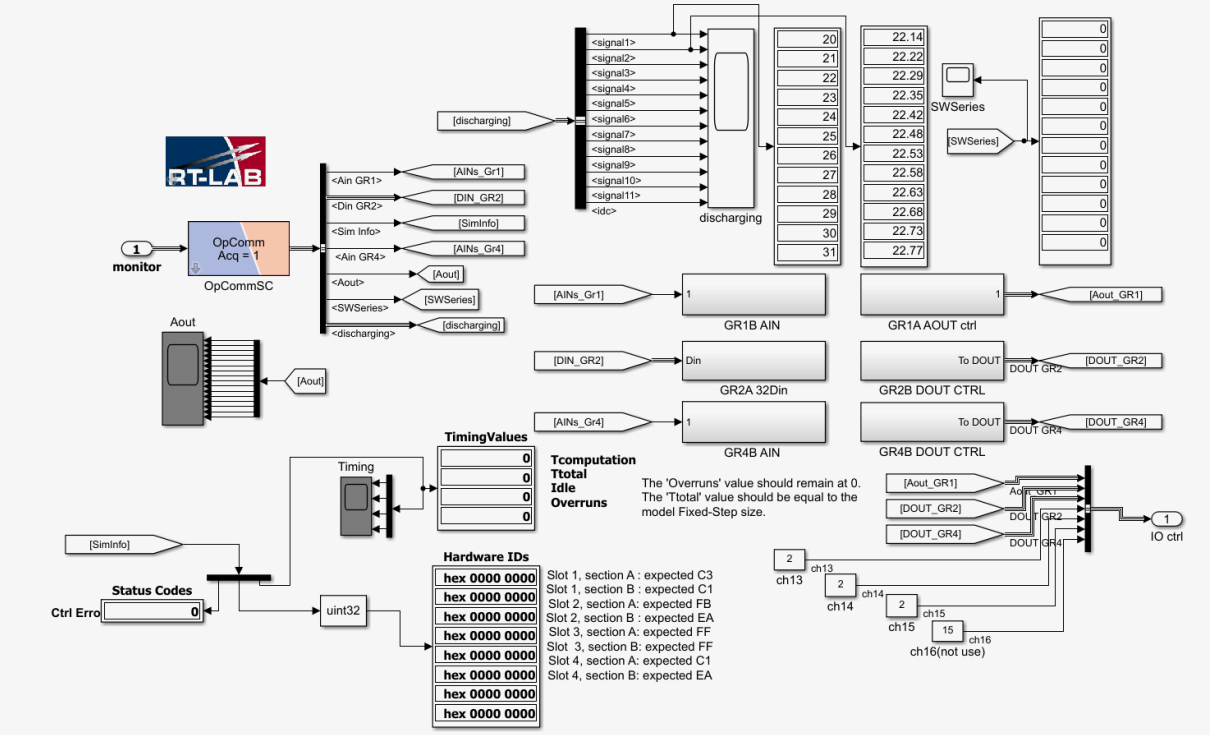

Figure 7. 8 Graphical interface for real time monitoring (SC_Console)

7.4 Experimental verification of residual imbalance during charging

The experimental testing is performed for charging battery packs with multiple C-rates (0.5C, 1C, and 2C) using the same parameters of initial SOC and voltage imbalance as used for

simulation in Chapter 5, section 5.2, Table 5.6. The voltage that can be sensed straight from the battery cell serves as the basis for the control algorithm of the proposed balancing topology. However, Figure 7.9(a) also displays the SOC for each module, demonstrating that li-ion voltage is a reliable approximation of SOC. The experimental voltage results of individual modules at 0.5C rate charging are displayed in Figure 7.9(b). Similarly, Figures 7.9(c, d) and 7.9(e, f) show the SOC and voltage outcomes for charging at 1C and 2C rates, respectively.

The only difference arises from fluctuations in voltage measurements, as the process of experimental voltage measurement introduces noise into the voltage signals. However, the variation in voltages is reduced to a maximum of 250 mV by moving average filter, to have less effect on the controller performance and achieve SOC/voltage balancing.

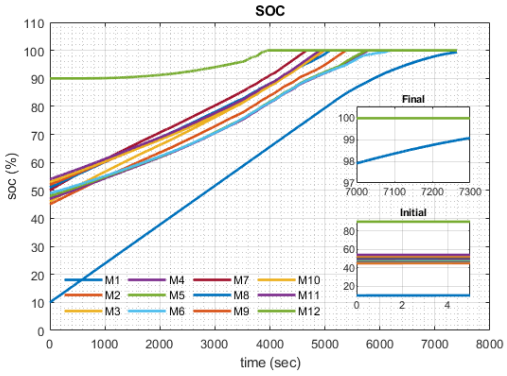

(a) soc graph

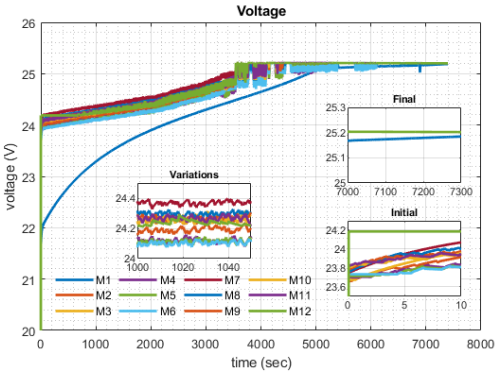

(b) voltage graph

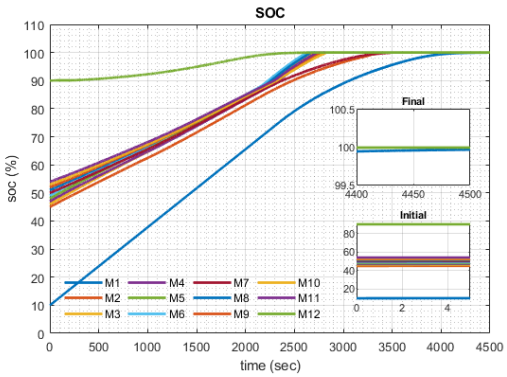

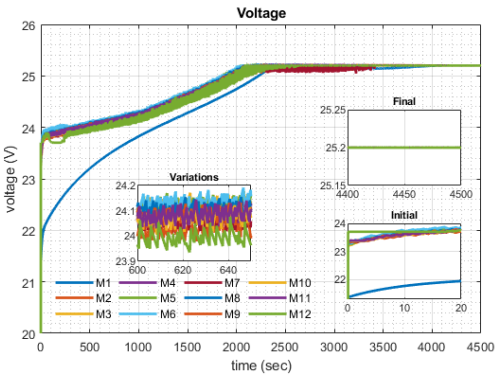

© soc graph (d) voltage graph

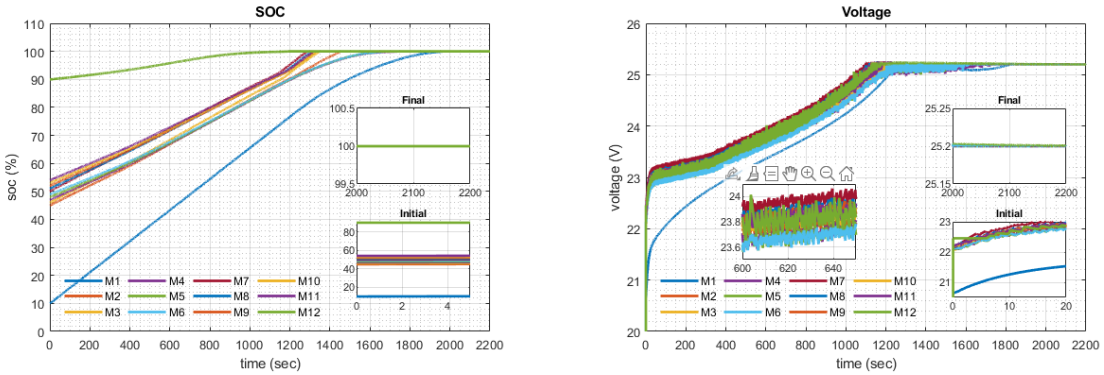

(e) soc graph (f) voltage graph

Figure 7. 9 Battery charging at multiple C-rate (0.5C, 1C, and 2C) with proposed balancing topology

The experimental and simulation results are closely matched other than voltage fluctuations. The experimental and simulation data of residual SOC and voltage imbalance for the various C-rate (0.5C, 1C, and 2C) charging modes are reported in Table 7.1. This table shows both results give approx. zero residual imbalance at the end of charging process for multiple C-rates.

Table 7. 1 Experimental and Simulation data of residual imbalance at the end of charging

C-rate	**Initial SOC imbalance of Experiment and Simulation (%)**	**Residual SOC imbalance of Experiment (%)**	**Residual SOC imbalance of Simulation (%)**	**Initial Voltage imbalance of Experiment and Simulation (V)**	**Residual Voltage imbalance of Experiment (V)**	**Residual Voltage imbalance of Simulation (V)**
0.5C	80	1	0	2.5	0.02	0
1C	80	0	0	2.3	0	0
2C	80	0	0	1.8	0	0

7.5 Experimental verification of speed control

The effectiveness of FOC in regulating motor speed is illustrated by the motor speed step response testing results with modular battery packs in Figure 7.10(a). Furthermore, Figure 7.10(b) illustrates the battery pack voltage connected with the traction inverter, which provides

variable DC-link voltage according to the speed of motor. The step response is tested with the same parameters of individual modules as tested in simulation chapter 5 section 5.5, to check the resemblance between simulation and experimental results. The maximum voltage of the battery pack is 265V due to initial 30% SOC of each module. Figure 7.10(b) shows the battery pack voltage increase with the increase in motor speed and when the battery voltage reaches to its maximum voltage it begins to decrease due to battery pack discharging.

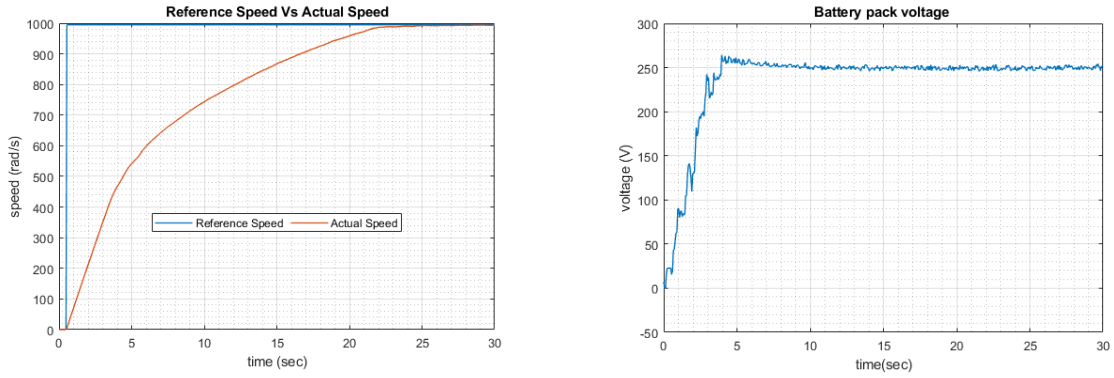

(a) Motor speed (b) Variable DC voltage

Figure 7. 10 Step response of motor speed with modular battery pack

7.6 Experimental verification of Residual imbalance at dynamic discharging

The EV battery pack was discharged under dynamic load conditions, to evaluate the effectiveness of bypass balancing method and confirm the controller design's performance through experimentation. To replicate real-world driving circumstances, the WLTP-3 drive cycle was used. As described in Chapter 5, Table 5.5, the initial imbalance circumstances for the battery pack modules were the same as those utilized in the simulation.

The SOC of the battery pack modules is depicted in Figure 7.11(a), and Figure 7.11(b) shows the corresponding voltages. During the discharging process, the SOC and voltage variations across modules are displayed in Figure 7.11(c, d). at the end of discharging, the initial voltage

difference of 2.3V is decreased to 0.5V with a variation of 250mV and the initial 30% SOC difference is reduced to 1%. When the discharging process is stopped, there is a significant decrease in the imbalance between the battery pack modules which gives a good match with the simulation's predictions. However, the fluctuations in the voltages are due to the electromagnetic noise addition in voltage measurements during experimental work. These results emphasize the modular battery pack's ability to minimize imbalances as well as the controller's successful implementation at dynamic load conditions.

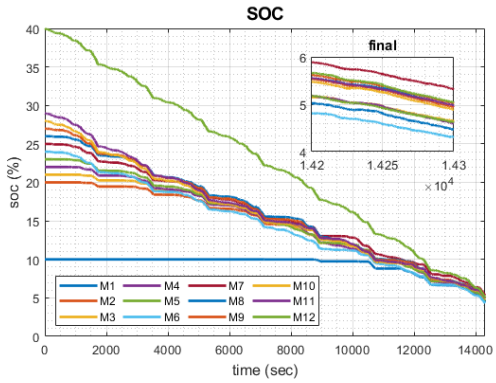

(a) soc graph

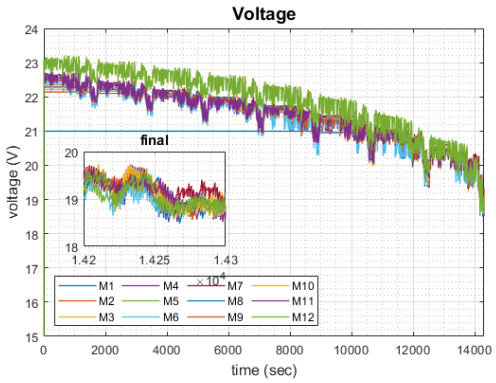

(b) voltage graph

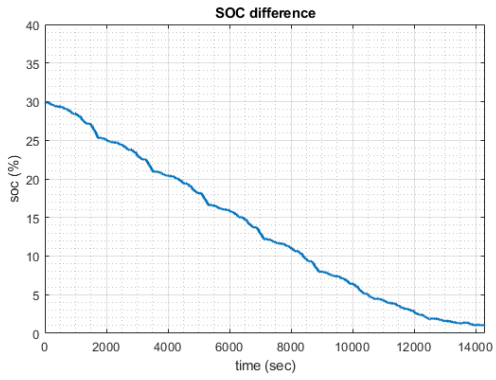

(c) soc difference

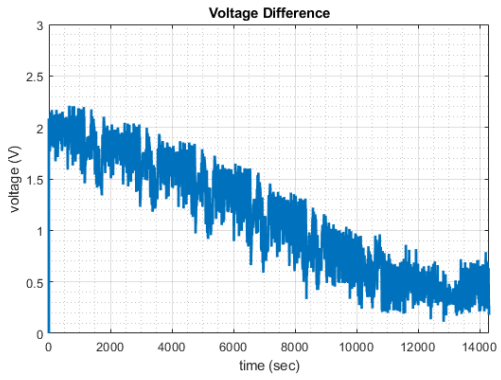

(d) voltage difference

Figure 7. 11 Voltage balancing with modular battery pack discharging with variable speed

The dynamic speed profile and the actual motor speed during the experimental testing are shown in Figure 7.12(a). The motor speed continuously follows the reference speed, demonstrating the effective performance of the FOC technique. Figure 7.12(b) displays the battery pack voltage, demonstrating how the traction inverter receives a changing DC-link voltage based on speed changes. The controller bypassed a different number of modules, which explains the reason why the variable DC link in the experimental results is not the same as the simulation. The reason the battery pack voltage is more variable than in the simulation is that the controller is based on voltage measurement, whereas the voltage varies due to noise addition in the experimental setup.

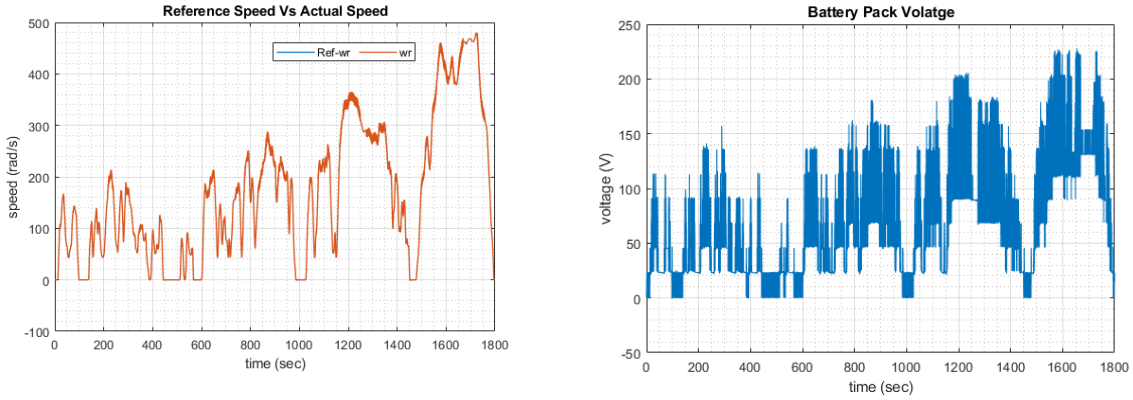

(a) Speed profile (b) Variable DC link

Figure 7. 12 Experimental results of motor speed profile and Variable DC link voltage

This chapter explains the building of experimental environment for testing proposed method. The same parameters for battery pack and inductor motor are used during HIL testing, as used for simulation, to verify the consistency between the experimental and simulated results. The conclusion of thesis and future recommendations are presented in the next chapter.

Chapter 8: Conclusion and Future Recommendation

8.1 Conclusion

The background showed the increasing demand of Li-ion batteries in EVs to provide necessary power, as EV battery pack consist of parallel and series combination of Li-ion cells. However, the traction inverter power loss and cell imbalance are the main issues with EV battery packs. The cell balancing is an important function of BMS to solve the cell imbalance problem. There are several factors of Li-ion like SOC, capacity, temperature, self-discharge rate and impedance which cause the imbalance between cells. These imbalances decrease the EV battery pack capacity utilisation as the battery stop charging or discharging due to one or more weak capacity cells presence. The cell balancing is necessary to achieve better capacity utilization of EV battery pack. The basic cell balancing techniques has been reviewed to explain the circuit complexity, number of components, energy transfer methods and control complexity of each method. The proposed bypass method has been investigated in depth to identify the important factors for its optimisation. The overview of bypass balancing method shows that the SOC were used as a control variable. However, the SOC estimation is challenging as well as it increases the controller complexity, and accurate SOC estimation is not possible due to variations in battery characteristics (voltage, temperature, current). The voltage-based control is also difficult due to variation in voltage measurement, but it eliminates the need of SOC estimation. Furthermore, identify the requirement of an adaptive charge controller to adjust the supply voltage according to the number of bypass cells or modules.

The literature also verified the benefits of using variable DC-link for inverter to achieve lower power losses and reduced THD to increase efficiency. The DC-DC converters used to provide variable DC-link voltage for many applications like energy storage system and PV system but

in hybrid EVs these converters focused on battery charging during regenerative braking system. In EVs, DC-DC converter can provide variable DC-link voltage, but it will also introduce power loss and cannot deal with the imbalance between battery pack cells or modules. The proposed modular battery packs with bypass balancing method gives benefits of providing flexible DC-link voltage to the EV traction inverter and voltage balancing between series-connected modules in the EV battery pack.

The MATLAB Simulink was used to develop the proposed method and design control algorithms. The results in chapter 3 section 3.2 demonstrate the cell model charge and discharge characteristics follows the datasheet graphs. The EV battery module is developed by modifying the parameters of the cell model, then these modules are connected in series to create the EV battery pack with the proposed bypass method. The per phase equivalent circuit model parameter were also calculated and optimised to develop induction motor model. The CCCV battery charge controller was implemented using two cascaded PI controllers for voltage and current control. The outer loop controls voltage while the inner loop controls current, and the output gives the supply voltage command for charger to adjust its voltage. The CCCV provides the CC at the beginning of charging while shift to CV mode after battery pack is charged up to 80% SOC which helps to perform fast charging. This controller also adjusts the charger supply voltage according to the number of bypass modules and the battery pack charging results in chapter 5 section 5.3 confirms it. FOC is another controller that was designed to control the induction motor speed and provide the voltage vs speed relationship, which was further used in battery pack discharging to provide variable DC-link voltage to the traction inverter.

The proposed method simulation and HIL results of battery pack charging and discharging mode presented in chapter 5 and 7, respectively. The results for the step response of the motor

speed explain the validation of FOC for motor speed control. The results of individual module voltages and SOCs also showed the Li-ion cells gives a good approximation of SOC.

The proposed topology was tested for the different conditions of initial SOC or voltage imbalance and the results shows approximately zero percent residual imbalance. According to simulation results, at the end of the battery pack's charge cycle, the proposed bypass method effectively balances the module voltages or SOCs with the approximately zero residual imbalance. At the end of discharge, 1% SOC and 0V voltage imbalance showed but the discharge voltage also showed fluctuation of 0.5V, which is due to rapid acceleration and deacceleration in the speed profile. To check the feasibility and performance of the controller, multiple C-rates (0.5C, 1C, 2C) charging current used for charging, and WLTP-3 dynamic speed profile used for discharging.

The experimental results of charging and discharging showed approximately zero SOC/voltage residual imbalance with some voltage variations due to noise. The fluctuations in voltage are due to noise in the experimental setup.

The proposed method produces higher power loss during charging mode compared with other balancing methods, but lower losses during discharging mode compared with fixed DC-link, which reduce overall system power loss.

This thesis verified the research claims that the proposed bypass method provides variable DC-link voltage for the traction inverter which reduce the power loss and increase the inverter efficiency. The comparison of bypass topology with other methods in terms of indicative cell balancing speed shows rapid balancing because of higher balancing current. The proposed method achieved approximate zero SOC/voltage residual imbalance for both charge and discharge process

8.2 Future Recommendation

Numerous prospects for further research are presented by this thesis of modular battery packs with embedded cell balancing for EV battery packs.

1. This thesis does not consider the impact of the proposed topology on the cell temperature. The implementation of the modular battery pack in a real EV with consideration of an improved controller design for battery pack thermal management.
2. Design an advanced digital filter for voltage measurement to minimize voltage fluctuation which will improve the overall system performance.
3. Create a real-time regenerative braking charge controller to charge the cells or modules with lower capacity. This will decrease cell imbalance and may increase balancing speed.

References

[1] G. Bridge and E. Faigen, "Towards the lithium-ion battery production network: Thinking beyond mineral supply chains," *Energy Research & Social Science*, vol. 89, p. 102659, 2022.

[2] G. Bridge and E. Faigen, "Lithium, Brexit and Global Britain: Onshoring battery production networks in the UK," *The Extractive Industries and Society*, vol. 16, p. 101328, 2023.

[3] D. Thiruvonasundari and K. Deepa, "Optimized passive cell balancing for fast charging in electric vehicle," *IETE Journal of Research*, vol. 69, no. 4, pp. 2089-2097, 2023.

[4] "Electric vehicle outlook 2024." https://about.bnef.com/electric-vehicle-outlook/ (accessed 15/07/2024.

[5] T. Kim, W. Song, D.-Y. Son, L. K. Ono, and Y. Qi, "Lithium-ion batteries: outlook on present, future, and hybridized technologies," *Journal of materials chemistry A*, vol. 7, no. 7, pp. 2942-2964, 2019.

[6] H. Bae and Y. Kim, "Technologies of lithium recycling from waste lithium ion batteries: a review," *Materials advances*, vol. 2, no. 10, pp. 3234-3250, 2021.

[7] M. K. Hasan, M. Mahmud, A. A. Habib, S. Motakabber, and S. Islam, "Review of electric vehicle energy storage and management system: Standards, issues, and challenges," *Journal of energy storage*, vol. 41, p. 102940, 2021.

[8] "Tesla Model S 75D." https://ev-database.org/uk/car/1070/Tesla-Model-S-75D (accessed 15/07/2024.

[9] "Nissan Leaf." https://ev-database.org/uk/car/1656/Nissan-Leaf (accessed 15/07/2024.

[10] "Audi Q8 e-tron 55 quattro." https://ev-database.org/uk/car/1770/Audi-Q8-e-tron-55-quattro (accessed 15/07/2024.

[11] "Jaguar I-Pace EV400." https://ev-database.org/uk/car/1287/Jaguar-I-Pace-EV400 (accessed 15/07/2024.

[12] "Hyundai Kona Electric 64 kWh." https://ev-database.org/uk/car/1423/Hyundai-Kona-Electric-64-kWh (accessed 15/07/2024.

[13] "Porsche Taycan Turbo." https://ev-database.org/uk/car/1927/Porsche-Taycan-Turbo (accessed 15/07/2024.

[14] "Hyundai IONIQ 5 Long Range 2WD." https://ev-database.org/uk/car/1662/Hyundai-IONIQ-5-Long-Range-2WD (accessed 15/07/2024.

[15] "Kia EV6 Long Range 2WD." https://ev-database.org/uk/car/1481/Kia-EV6-Long-Range-2WD (accessed 15/07/2024.

[16] H. Dai, B. Jiang, X. Hu, X. Lin, X. Wei, and M. Pecht, "Advanced battery management strategies for a sustainable energy future: Multilayer design concepts and

research trends," *Renewable and Sustainable Energy Reviews,* vol. 138, p. 110480, 2021.

[17] Y. Wang *et al.*, "A comprehensive review of battery modeling and state estimation approaches for advanced battery management systems," *Renewable and Sustainable Energy Reviews,* vol. 131, p. 110015, 2020.

[18] M. U. Ali, A. Zafar, S. H. Nengroo, S. Hussain, M. Junaid Alvi, and H.-J. Kim, "Towards a smarter battery management system for electric vehicle applications: A critical review of lithium-ion battery state of charge estimation," *Energies,* vol. 12, no. 3, p. 446, 2019.

[19] M. Shen and Q. Gao, "A review on battery management system from the modeling efforts to its multiapplication and integration," *International Journal of Energy Research,* vol. 43, no. 10, pp. 5042-5075, 2019.

[20] H. A. Gabbar, A. M. Othman, and M. R. Abdussami, "Review of battery management systems (BMS) development and industrial standards," *Technologies,* vol. 9, no. 2, p. 28, 2021.

[21] S. Wen, "Cell balancing buys extra run time and battery life," *Analog Applications Journal,* vol. 1, 2009.

[22] F. Zhu, G. Liu, C. Tao, K. Wang, and K. Jiang, "Battery management system for Li-ion battery," *The Journal of Engineering,* vol. 2017, no. 13, pp. 1437-1440, 2017.

[23] M. Verasamy, M. Faisal, P. J. Ker, and M. Hannan, "Charging and discharging control of Li-Ion battery energy management for electric vehicle application," *Int. J. Eng. Technol,* vol. 7, no. 4, pp. 482-486, 2018.

[24] A. Bhattacharjee, R. K. Mohanty, and A. Ghosh, "Design of an optimized thermal management system for Li-ion batteries under different discharging conditions," *Energies,* vol. 13, no. 21, p. 5695, 2020.

[25] M. Cacciato, G. Nobile, G. Scarcella, and G. Scelba, "Real-time model-based estimation of SOC and SOH for energy storage systems," *IEEE Transactions on Power Electronics,* vol. 32, no. 1, pp. 794-803, 2016.

[26] M. R. M. Kassim, W. A. W. Jamil, and R. M. Sabri, "State-of-charge (soc) and state-of-health (soh) estimation methods in battery management systems for electric vehicles," in *2021 IEEE International Conference on Computing (ICOCO)*, 2021: IEEE, pp. 91-96.

[27] M. Murnane and A. Ghazel, "A closer look at state of charge (SOC) and state of health (SOH) estimation techniques for batteries," *Analog devices,* vol. 2, pp. 426-436, 2017.

[28] S.-C. Huang, K.-H. Tseng, J.-W. Liang, C.-L. Chang, and M. G. Pecht, "An online SOC and SOH estimation model for lithium-ion batteries," *Energies,* vol. 10, no. 4, p. 512, 2017.

[29] X. Hu, K. Zhang, K. Liu, X. Lin, S. Dey, and S. Onori, "Advanced fault diagnosis for lithium-ion battery systems: A review of fault mechanisms, fault features, and diagnosis procedures," *IEEE Industrial Electronics Magazine,* vol. 14, no. 3, pp. 65-91, 2020.

[30] X. Li and Z. Wang, "A novel fault diagnosis method for lithium-Ion battery packs of electric vehicles," *Measurement,* vol. 116, pp. 402-411, 2018.

[31] R. Xiong, Q. Yu, and W. Shen, "Review on sensors fault diagnosis and fault-tolerant techniques for lithium ion batteries in electric vehicles," in *2018 13th IEEE Conference on Industrial Electronics and Applications (ICIEA)*, 2018: IEEE, pp. 406-410.

[32] L. Buccolini, A. Ricci, C. Scavongelli, G. DeMaso-Gentile, S. Orcioni, and M. Conti, "Battery Management System (BMS) simulation environment for electric vehicles," in *2016 IEEE 16th International Conference on Environment and Electrical Engineering (EEEIC)*, 2016: IEEE, pp. 1-6.

[33] A. Hauser and R. Kuhn, "High-voltage battery management systems (BMS) for electric vehicles," in *Advances in battery technologies for electric vehicles*: Elsevier, 2015, pp. 265-282.

[34] D. Marcos, M. Garmendia, J. Crego, and J. A. Cortajarena, "Functional Safety BMS Design Methodology for Automotive Lithium-Based Batteries," *Energies,* vol. 14, no. 21, p. 6942, 2021.

[35] D. V. Cadar, D. M. Petreus, and T. M. Patarau, "An energy converter method for battery cell balancing," in *33rd International Spring Seminar on Electronics Technology, ISSE 2010*, 2010: IEEE, pp. 290-293.

[36] U. Murali, "Thermal management for electric aviation: An product development approach," 2022.

[37] G. Georgiadis, "Thermal management of Lithium–ion batteries used in EVs and HEVs," 2017.

[38] G. Altemose, P. Hellermann, and T. Mazz, "Active cell balancing system using an isolated share bus for Li-Ion battery management: Focusing on satellite applications," in *2011 IEEE Long Island Systems, Applications and Technology Conference*, 2011: IEEE, pp. 1-7.

[39] M. Cherukuri and M. Kanthi, "Battery management system design for electric vehicle," in *2019 IEEE international conference on distributed computing, VLSI, Electrical circuits and robotics (DISCOVER)*, 2019: IEEE, pp. 1-6.

[40] Z. B. Omariba, L. Zhang, and D. Sun, "Review of battery cell balancing methodologies for optimizing battery pack performance in electric vehicles," *IEEE Access,* vol. 7, pp. 129335-129352, 2019.

[41] C.-Y. Zun, S.-U. Park, and H.-S. Mok, "New cell balancing charging system research for lithium-ion batteries," *Energies,* vol. 13, no. 6, p. 1393, 2020.

[42] A. Fill and K. P. Birke, "Influences of Cell to Cell Variances and the Battery Design on thermal and electrical imbalances among parallel Lithium-Ion Cells," in *2021 22nd IEEE International Conference on Industrial Technology (ICIT)*, 2021, vol. 1: IEEE, pp. 391-396.

[43] V. Muenzel, M. Brazil, I. Mareels, J. De Hoog, and D. A. Thomas, "Modeling reversible self-discharge in series-connected Li-ion battery cells," in *IEEE 2013 Tencon-Spring*, 2013: Ieee, pp. 470-474.

[44] S. S. Zhang, "The effect of the charging protocol on the cycle life of a Li-ion battery," *Journal of power sources,* vol. 161, no. 2, pp. 1385-1391, 2006.

[45] M. Baumann, L. Wildfeuer, S. Rohr, and M. Lienkamp, "Parameter variations within Li-Ion battery packs–Theoretical investigations and experimental quantification," *Journal of Energy Storage,* vol. 18, pp. 295-307, 2018.

[46] R. Gogoana, "Internal resistance variances in lithium-ion batteries and implications in manufacturing," Massachusetts Institute of Technology, 2012.

[47] Y. Zheng, X. Han, L. Lu, J. Li, and M. Ouyang, "Lithium ion battery pack power fade fault identification based on Shannon entropy in electric vehicles," *Journal of Power Sources,* vol. 223, pp. 136-146, 2013.

[48] T. R. Tanim, M. G. Shirk, R. L. Bewley, E. J. Dufek, and B. Y. Liaw, "Fast charge implications: Pack and cell analysis and comparison," *Journal of Power Sources,* vol. 381, pp. 56-65, 2018.

[49] F. S. J. Hoekstra, H. J. Bergveld, and M. Donkers, "Optimal control of active cell balancing: Extending the range and useful lifetime of a battery pack," *IEEE Transactions on Control Systems Technology,* vol. 30, no. 6, pp. 2759-2766, 2022.

[50] Panasonic. *NCR-18650B,* 2G23X0KYKU. [Online]. Available: https://www.imrbatteries.com/content/panasonic_ncr18650b-2.pdf. Accessed: 15/07/2024.

[51] W. Choi and S. Hong, "An Experimental Study on the Cell Balancing Parameters for Faulty Cell Detection in a Battery Module," *Batteries,* vol. 8, no. 11, p. 218, 2022.

[52] S. Kumar, S. K. Rao, A. R. Singh, and R. Naidoo, "Switched-Resistor Passive Balancing of Li-Ion Battery Pack and Estimation of Power Limits for Battery Management System," *International Journal of Energy Research,* vol. 2023, 2023.

[53] L. Xie *et al.*, "A facile approach to high precision detection of cell-to-cell variation for Li-ion batteries," *Scientific reports,* vol. 10, no. 1, p. 7182, 2020.

[54] A. Naha *et al.*, "An incremental voltage difference based technique for online state of health estimation of Li-ion batteries," *Scientific Reports,* vol. 10, no. 1, p. 9526, 2020.

[55] B. Jiang, "Active cell balancing algorithms in lithium-ion battery," 2020.

[56] M. Uzair, G. Abbas, and S. Hosain, "Characteristics of battery management systems of electric vehicles with consideration of the active and passive cell balancing process," *World Electric Vehicle Journal,* vol. 12, no. 3, p. 120, 2021.

[57] A. B. Ahmad, C. A. Ooi, D. Ishak, and J. Teh, "Cell balancing topologies in battery energy storage systems: A review," in *10th International Conference on Robotics, Vision, Signal Processing and Power Applications: Enabling Research and Innovation Towards Sustainability*, 2019: Springer, pp. 159-165.

[58] P. V. Chombo and Y. Laoonual, "A review of safety strategies of a Li-ion battery," *Journal of Power Sources,* vol. 478, p. 228649, 2020.

[59] A. A. Habib, M. K. Hasan, M. Mahmud, S. Motakabber, M. I. Ibrahimya, and S. Islam, "A review: Energy storage system and balancing circuits for electric vehicle application," *IET Power Electronics,* vol. 14, no. 1, pp. 1-13, 2021.

[60] L. Komsiyska *et al.*, "Critical review of intelligent battery systems: Challenges, implementation, and potential for electric vehicles," *Energies,* vol. 14, no. 18, p. 5989, 2021.

[61] M. S. H. Lipu *et al.*, "Review of electric vehicle converter configurations, control schemes and optimizations: Challenges and suggestions," *Electronics,* vol. 10, no. 4, p. 477, 2021.

[62] K. Liu, K. Li, Q. Peng, and C. Zhang, "A brief review on key technologies in the battery management system of electric vehicles," *Frontiers of mechanical engineering,* vol. 14, pp. 47-64, 2019.

[63] X. Lü *et al.*, "Energy management of hybrid electric vehicles: A review of energy optimization of fuel cell hybrid power system based on genetic algorithm," *Energy Conversion and Management,* vol. 205, p. 112474, 2020.

[64] U. K. Das *et al.*, "Advancement of lithium-ion battery cells voltage equalization techniques: A review," *Renewable and Sustainable Energy Reviews,* vol. 134, p. 110227, 2020.

[65] M. Daowd, N. Omar, P. Van Den Bossche, and J. Van Mierlo, "Passive and active battery balancing comparison based on MATLAB simulation," in *2011 IEEE Vehicle Power and Propulsion Conference*, 2011: IEEE, pp. 1-7.

[66] T. Duraisamy and D. Kaliyaperumal, "Adaptive passive balancing in battery management system for e-mobility," *International Journal of Energy Research,* vol. 45, no. 7, pp. 10752-10764, 2021.

[67] W. C. Lee, D. Drury, and P. Mellor, "Comparison of passive cell balancing and active cell balancing for automotive batteries," in *2011 IEEE Vehicle Power and Propulsion Conference*, 2011: IEEE, pp. 1-7.

[68] P. S. Babu and K. Ilango, "Comparative analysis of passive and active cell balancing of li ion batteries," in *2022 Third International Conference on Intelligent Computing Instrumentation and Control Technologies (ICICICT)*, 2022: IEEE, pp. 711-716.

[69] S. Dalvi and S. Thale, "Design of DSP controlled passive cell balancing network based battery management system for EV application," in *2020 IEEE India Council International Subsections Conference (INDISCON)*, 2020: IEEE, pp. 84-89.

[70] J. Carter, Z. Fan, and J. Cao, "Cell equalisation circuits: A review," *Journal of Power Sources,* vol. 448, p. 227489, 2020.

[71] Y. Hua *et al.*, "A comprehensive review on inconsistency and equalization technology of lithium-ion battery for electric vehicles," *International Journal of Energy Research,* vol. 44, no. 14, pp. 11059-11087, 2020.

[72] A. Kelkar, Y. Dasari, and S. S. Williamson, "A comprehensive review of power electronics enabled active battery cell balancing for smart energy management," in *2020 IEEE International Conference on Power Electronics, Smart Grid and Renewable Energy (PESGRE2020)*, 2020: IEEE, pp. 1-6.

[73] T. A. Abdul-jabbar, A. Kersten, A. Mashayekh, A. A. Obed, A. J. Abid, and M. Kuder, "Efficient battery cell balancing methods for low-voltage applications: A review," in *2022 IEEE International Conference in Power Engineering Application (ICPEA)*, 2022: IEEE, pp. 1-7.

[74] J. S. F. Lu, "A COMPARATIVE ANALYSIS OF SINGLE SWITCHED CAPACITOR AND SWITCHED SHUNTING RESISTOR BATTERY CELL BALANCING METHODS," *Journal of Engineering & Technological Advances*, vol. 8, no. 2, pp. 25-39, 2023.

[75] S. Kumar, S. K. Rao, A. R. Singh, and R. Naidoo, "Switched-Resistor Passive Balancing of Li-Ion Battery Pack and Estimation of Power Limits for Battery Management System," *International Journal of Energy Research*, vol. 2023, no. 1, p. 5547603, 2023.

[76] F. S. Azad, A. A. Habib, A. Rahman, and I. Ahmed, "Active cell balancing of Li-Ion batteries using single capacitor and single LC series resonant circuit," *Bulletin of Electrical Engineering and Informatics*, vol. 9, no. 4, pp. 1318-1325, 2020.

[77] T. Conway, "A Simple Robust Active BMS for Lithium Ion Battery Stacks," *Authorea Preprints*, 2023.

[78] T. Duraisamy and D. Kaliyaperumal, "Active cell balancing for electric vehicle battery management system," *International Journal of Power Electronics and Drive Systems*, vol. 11, no. 2, p. 571, 2020.

[79] K. B. Meti, P. D. Inamati, R. D. Gaddanakeri, H. R. Patil, A. Patil, and A. B. Raju, "Active Cell Balancing using Multi-winding Forward Converter for Lithium-ion Battery," in *2022 International Conference on Smart Generation Computing, Communication and Networking (SMART GENCON)*, 2022: IEEE, pp. 1-7.

[80] A. F. Moghaddam and A. Van Den Bossche, "An active cell equalization technique for lithium ion batteries based on inductor balancing," in *2018 9th International Conference on Mechanical and Aerospace Engineering (ICMAE)*, 2018: IEEE, pp. 274-278.

[81] A. Panchal, K. Bhatt, S. Gitaye, M. Bhand, and A. Sheikh, "Design and Simulation of an Inductor based Active Cell Balancing Circuit for Lithium-ion Batteries," in *2022 4th Global Power, Energy and Communication Conference (GPECOM)*, 2022: IEEE, pp. 89-94.

[82] V.-L. Pham, V.-T. Duong, and W. Choi, "High-efficiency active cell-to-cell balancing circuit for Lithium-Ion battery modules using LLC resonant converter," *Journal of Power Electronics*, vol. 20, pp. 1037-1046, 2020.

[83] C. Y. Pok, "Active Cell Balancing with DC/DC Converter for Electric Vehicle," Tunku Abdul Rahman University College, 2022.

[84] M. O. Qays, Y. Buswig, M. L. Hossain, M. M. Rahman, and A. Abu-Siada, "Active cell balancing control strategy for parallelly connected LiFePO 4 batteries," *CSEE Journal of Power and Energy Systems*, vol. 7, no. 1, pp. 86-92, 2020.

[85] N. Reema, M. Shreelakshmi, G. Jagadan, and N. Sasidharan, "A novel coupled inductor based active balancing technique for ultracapacitors," in *2020 IEEE International Conference on Power Electronics, Drives and Energy Systems (PEDES)*, 2020: IEEE, pp. 1-6.

[86] A. Samanta and S. Chowdhuri, "Active cell balancing of lithium-ion battery pack using dual DC-DC converter and auxiliary lead-acid battery," *Journal of Energy Storage*, vol. 33, p. 102109, 2021.

[87] D. Shylla, R. Swarnkar, R. Harikrishnan, and S. H. M. Ali, "Active Cell Balancing During Charging and Discharging of Lithium-Ion Batteries in MATLAB/Simulink," in *2023 Second International Conference on Electronics and Renewable Systems (ICEARS)*, 2023: IEEE, pp. 201-208.

[88] J. Kacetl, J. Fang, T. Kacetl, N. Tashakor, and S. Goetz, "Design and analysis of modular multilevel reconfigurable battery converters for variable bus voltage powertrains," *IEEE Transactions on Power Electronics*, vol. 38, no. 1, pp. 130-142, 2022.

[89] Y. Li, P. Yin, and J. Chen, "Active equalization of lithium-ion battery based on reconfigurable topology," *Applied Sciences*, vol. 13, no. 2, p. 1154, 2023.

[90] B. Majmunovic, R. Sarda, R. Teodorescu, C. Lascu, and M. Ricco, "Highly efficient smart battery pack for EV drivetrains," in *2017 IEEE Vehicle Power and Propulsion Conference (VPPC)*, 2017: IEEE, pp. 1-5.

[91] M. Ricco, J. Meng, T. Gherman, G. Grandi, and R. Teodorescu, "Smart battery pack for electric vehicles based on active balancing with wireless communication feedback," *Energies*, vol. 12, no. 20, p. 3862, 2019.

[92] C. Zhang, Y. Li, J. Huang, Z. Xia, and J. Liu, "Research on alternating equalization control systems for lithium-ion cells charging," *World Electric Vehicle Journal*, vol. 12, no. 3, p. 114, 2021.

[93] M. Abareshi, M. Hamzeh, S. Farhangi, and S. M. M. Alavi, "Robust control of a forward-converter active battery cell balancing," *IET Power Electronics*, 2023.

[94] M. Afkar, R. Gavagsaz-Ghoachani, M. Phattanasak, and S. Pierfederici, "Operating mode analysis of a Modular Converter: Experimental validation," *IEEE Transactions on Industry Applications*, vol. 58, no. 4, pp. 4889-4902, 2022.

[95] A. Avila, A. Garcia-Bediaga, I. Alzuguren, M. Vasić, and A. Rujas, "A modular multifunction power converter based on a multiwinding flyback transformer for EV application," *IEEE Transactions on Transportation Electrification*, vol. 8, no. 1, pp. 168-179, 2021.

[96] E. Chatzinikolaou and D. J. Rogers, "Cell SoC balancing using a cascaded full-bridge multilevel converter in battery energy storage systems," *IEEE Transactions on Industrial Electronics*, vol. 63, no. 9, pp. 5394-5402, 2016.

[97] A. Farzan Moghaddam and A. Van den Bossche, "A Ćuk converter cell balancing technique by using coupled inductors for lithium-based batteries," *Energies*, vol. 12, no. 15, p. 2881, 2019.

[98] A. A. Habib and M. K. Hasan, "Lithium-ion battery state-of-charge balancing circuit using single resonant converter for electric vehicle applications," *Journal of Energy Storage*, vol. 61, p. 106727, 2023.

[99] Z. Li, R. Lizana, A. V. Peterchev, and S. M. Goetz, "Distributed balancing control for modular multilevel series/parallel converter with capability of sensorless operation," in *2017 IEEE Energy Conversion Congress and Exposition (ECCE)*, 2017: IEEE, pp. 1787-1793.

[100] A. F. Moghaddam and A. Van den Bossche, "Flyback converter balancing technique for lithium based batteries," in *2019 8th International Conference on Modern Circuits and Systems Technologies (MOCAST)*, 2019: IEEE, pp. 1-4.

[101] H. Moradisizkoohi, N. Elsayad, and O. A. Mohammed, "An integrated interleaved ultrahigh step-up DC–DC converter using dual cross-coupled inductors with built-in input current balancing for electric vehicles," *IEEE Journal of Emerging and Selected Topics in Power Electronics*, vol. 8, no. 1, pp. 644-657, 2019.

[102] G. L. Schiavon, E. Agostini Jr, and C. B. Nascimento, "Quasi-Resonant Single-Switch High-Voltage-Gain DC-DC Converter with Coupled Inductor and Voltage Multiplier Cell," *Energies*, vol. 16, no. 9, p. 3874, 2023.

[103] Y. Shang, C. Zhang, N. Cui, and J. M. Guerrero, "A cell-to-cell battery equalizer with zero-current switching and zero-voltage gap based on quasi-resonant LC converter and boost converter," *IEEE Transactions on Power Electronics*, vol. 30, no. 7, pp. 3731-3747, 2014.

[104] N. Ganesha, G. Yadav, and C. Gowrishankara, "Analysis and implementation of inductor based active battery cell balancing topology," in *2020 IEEE International Conference on Power Electronics, Drives and Energy Systems (PEDES)*, 2020: IEEE, pp. 1-6.

[105] A. Farzan Moghaddam and A. Van den Bossche, "A single transformer for active cell equalization method of lithium-ion batteries with two times fewer secondaries than cells," *Electronics*, vol. 8, no. 9, p. 951, 2019.

[106] K.-M. Lee, S.-W. Lee, Y.-G. Choi, and B. Kang, "Active balancing of Li-ion battery cells using transformer as energy carrier," *IEEE Transactions on Industrial Electronics*, vol. 64, no. 2, pp. 1251-1257, 2016.

[107] L. Wan, Y. Chen, and Y. Zhou, "Design of Balanced Charging Circuit for Lithium Ion Battery," in *2019 Chinese Control Conference (CCC)*, 2019: IEEE, pp. 6476-6480.

[108] T. Bat-Orgil, B. Dugarjav, and T. Shimizu, "Battery cell balancer with active power decoupling function," in *2019 10th International Conference on Power Electronics and ECCE Asia (ICPE 2019-ECCE Asia)*, 2019: IEEE, pp. 1-7.

[109] T. Girijaprasanna and C. Dhanamjayulu, "A LC Voltage Equalization Methodology to Enable Balancing of Li-ion Cells Connected in Series," in *2021 Innovations in Power and Advanced Computing Technologies (i-PACT)*, 2021: IEEE, pp. 1-6.

[110] S. Luo, D. Qin, H. Wu, T. Wang, and J. Chen, "Multi-Cell-to-Multi-Cell Battery Equalization in Series Battery Packs Based on Variable Duty Cycle," *Energies*, vol. 15, no. 9, p. 3263, 2022.

[111] Z. Zhang, L. Zhang, L. Hu, and C. Huang, "Active cell balancing of lithium-ion battery pack based on average state of charge," *International Journal of Energy Research*, vol. 44, no. 4, pp. 2535-2548, 2020.

[112] T. M. Bui, C.-H. Kim, K.-H. Kim, and S. B. Rhee, "A modular cell balancer based on multi-winding transformer and switched-capacitor circuits for a series-connected battery string in electric vehicles," *Applied Sciences*, vol. 8, no. 8, p. 1278, 2018.

[113] J. Du, Y. Wang, A. Tripathi, and J. S. L. Lam, "Li-ion battery cell equalization by modules with chain structure switched capacitors," in *2016 Asian Conference on Energy, Power and Transportation Electrification (ACEPT)*, 2016: IEEE, pp. 1-6.

[114] A. Jain and S. K. Jain, "Multi-layer cell balancing using switched inductor and switched capacitor topology," in *2021 28th International Workshop on Electric Drives: Improving Reliability of Electric Drives (IWED)*, 2021: IEEE, pp. 1-6.

[115] A. Lasić, Ž. Ban, B. Puškarić, and V. Šunde, "Supercapacitor stack active voltage balancing circuit based on dual active full bridge converter with selective low voltage side," in *2020 IEEE 11th International Symposium on Power Electronics for Distributed Generation Systems (PEDG)*, 2020: IEEE, pp. 627-636.

[116] L. Liu, R. Mai, B. Xu, W. Sun, W. Zhou, and Z. He, "Design of parallel resonant switched-capacitor equalizer for series-connected battery strings," *IEEE Transactions on Power Electronics*, vol. 36, no. 8, pp. 9160-9169, 2021.

[117] A. F. Moghaddam and A. Van den Bossche, "A cell equalization method based on resonant switched capacitor balancing for lithium ion batteries," in *2018 9th International Conference on Mechanical and Aerospace Engineering (ICMAE)*, 2018: IEEE, pp. 337-341.

[118] R. Paul, "Electric vehicle cell balancing using single and multi tiered switched capacitor," in *2022 4th International Conference on Energy, Power and Environment (ICEPE)*, 2022: IEEE, pp. 1-6.

[119] S. Singirikonda and Y. Obulesu, "Active cell voltage balancing of Electric vehicle batteries by using an optimized switched capacitor strategy," *Journal of Energy Storage*, vol. 38, p. 102521, 2021.

[120] Y. Wang, H. Yin, S. Han, A. Alsabbagh, and C. Ma, "A novel switched capacitor circuit for battery cell balancing speed improvement," in *2017 IEEE 26th International Symposium on Industrial Electronics (ISIE)*, 2017: IEEE, pp. 1977-1982.

[121] Y. Ye and K. W. E. Cheng, "Analysis and design of zero-current switching switched-capacitor cell balancing circuit for series-connected battery/supercapacitor," *IEEE Transactions on Vehicular Technology*, vol. 67, no. 2, pp. 948-955, 2017.

[122] Y. Ye and K. W. E. Cheng, "An automatic switched-capacitor cell balancing circuit for series-connected battery strings," *Energies*, vol. 9, no. 3, p. 138, 2016.

[123] Y. Ye, K. W. E. Cheng, Y. C. Fong, X. Xue, and J. Lin, "Topology, modeling, and design of switched-capacitor-based cell balancing systems and their balancing exploration," *IEEE Transactions on Power Electronics*, vol. 32, no. 6, pp. 4444-4454, 2016.

[124] Y. Ye, J. Lin, Z. Li, and X. Wang, "Double-tiered cell balancing system with switched-capacitor and switched-inductor," *IEEE Access*, vol. 7, pp. 183356-183364, 2019.

[125] Y. Ye, J. Jiang, E. Zhao, P. Li, Z. Li, and X. Hui, "An Improved Balancing Strategy for Inductor-Based Balancing Circuit," in *2023 IEEE International Conference on Power Science and Technology (ICPST)*, 2023: IEEE, pp. 387-391.

[126] A. Farzan Moghaddam and A. Van den Bossche, "An efficient equalizing method for lithium-ion batteries based on coupled inductor balancing," *Electronics*, vol. 8, no. 2, p. 136, 2019.

[127] L. Liu, G. Goetting, and J. Xie, "Loss minimization using variable dc-link voltage technique for permanent magnet synchronous motor traction system in battery electric vehicle," in *2018 IEEE Vehicle Power and Propulsion Conference (VPPC)*, 2018: IEEE, pp. 1-5.

[128] C. Pinto, J. V. Barreras, E. Schaltz, and R. E. Araujo, "Evaluation of advanced control for li-ion battery balancing systems using convex optimization," *IEEE Transactions on Sustainable Energy*, vol. 7, no. 4, pp. 1703-1717, 2016.

[129] A. M. Imtiaz, F. H. Khan, and H. Kamath, "A low-cost time shared cell balancing technique for future lithium-ion battery storage system featuring regenerative energy distribution," in *2011 Twenty-Sixth Annual IEEE Applied Power Electronics Conference and Exposition (APEC)*, 2011: IEEE, pp. 792-799.

[130] H.-S. Park, C.-E. Kim, C.-H. Kim, G.-W. Moon, and J.-H. Lee, "A modularized charge equalizer for an HEV lithium-ion battery string," *IEEE Transactions on industrial electronics*, vol. 56, no. 5, pp. 1464-1476, 2009.

[131] J. Cao, N. Schofield, and A. Emadi, "Battery balancing methods: A comprehensive review," in *2008 IEEE Vehicle Power and Propulsion Conference*, 2008: IEEE, pp. 1-6.

[132] Y. Chen *et al.*, "An any-cell (s)-to-cell (s) equalization method with a single magnetic component for Lithium-ion battery pack," *Journal of Energy Storage*, vol. 33, p. 102071, 2021.

[133] X. Liu, H. Pang, and Y. Geng, "Dual-Layer Inductor Active Equalization Control for Series-Connected Lithium-Ion Batteries Based on SOC Estimation," *Electronics*, vol. 11, no. 8, p. 1169, 2022.

[134] V.-L. Pham, V.-T. Duong, and W. Choi, "A low cost and fast cell-to-cell balancing circuit for lithium-Ion battery strings," *Electronics*, vol. 9, no. 2, p. 248, 2020.

[135] J. C. Hall, "Battery cell bypass topology," United States, (accessed 15/07/2024), [Online]. Available: https://patents.google.com/patent/US5898291A/en

[136] B. Lawson, "A software configurable battery," in *26th Int. Battery, Hybrid Fuel Cell Electr. Veh. Symp*, 2012, pp. 252-263.

[137] S. Kıvrak, T. Özer, Y. Oğuz, and M. M. Kelek, "Novel active and passive balancing method-based battery management system design and implementation," *Journal of Power Electronics*, vol. 21, pp. 1855-1865, 2021.

[138] K. Sayed, A. Almutairi, N. Albagami, O. Alrumayh, A. G. Abo-Khalil, and H. Saleeb, "A review of DC-AC converters for electric vehicle applications," *Energies*, vol. 15, no. 3, p. 1241, 2022.

[139] S. Sridharan and P. T. Krein, "Optimizing variable DC link voltage for an induction motor drive under dynamic conditions," in *2015 IEEE Transportation Electrification Conference and Expo (ITEC)*, 2015: IEEE, pp. 1-6.

[140] P. Karlovsky, O. Lipcak, J. Bauer, and J. Lettl, "Predictive torque control of induction motor with integrated DC-link voltage optimisation," *IET Power Electronics,* vol. 13, no. 15, pp. 3396-3406, 2020.

[141] X. Ding, P. Lu, and Z. Shan, "A high-accuracy switching loss model of SiC MOSFETs in a motor drive for electric vehicles," *Applied Energy,* vol. 291, p. 116827, 2021.

[142] L. Liu *et al.*, "Loss minimization of traction systems in battery electric vehicles using variable dc-link voltage technique—experimental study," in *2020 22nd European Conference on Power Electronics and Applications (EPE'20 ECCE Europe)*, 2020: IEEE, pp. P. 1-P. 8.

[143] T.-S. Li, Y.-H. Yang, C.-A. Cheng, and Y.-M. Chen, "A variable DC-link voltage determination method for motor drives with SiC MOSFETs," in *2020 IEEE Workshop on Wide Bandgap Power Devices and Applications in Asia (WiPDA Asia)*, 2020: IEEE, pp. 1-6.

[144] K. J. Reddy and S. Natarajan, "Energy sources and multi-input DC-DC converters used in hybrid electric vehicle applications–A review," *International journal of hydrogen energy,* vol. 43, no. 36, pp. 17387-17408, 2018.

[145] D. Wu, H. Qamar, H. Qamar, and R. Ayyanar, "Comprehensive Analysis and Experimental Validation of 240-Clamped Space Vector PWM Technique Eliminating Zero States for EV Traction Inverters With Dynamic DC Link," *IEEE Transactions on Power Electronics,* vol. 35, no. 12, pp. 13295-13307, 2020.

[146] K. K. Prabhakar, M. Ramesh, A. Dalal, C. U. Reddy, A. K. Singh, and P. Kumar, "Efficiency investigation for electric vehicle powertrain with variable DC-link bus voltage," in *IECON 2016-42nd Annual Conference of the IEEE Industrial Electronics Society*, 2016: IEEE, pp. 1796-1801.

[147] D. Zhou, J. Wang, N. Hou, Y. Li, and J. Zou, "Dual-port inverters with internal DC–DC conversion for adjustable DC-link voltage operation of electric vehicles," *IEEE Transactions on Power Electronics,* vol. 36, no. 6, pp. 6917-6928, 2020.

[148] MATLAB. "Battery." https://uk.mathworks.com/help/sps/powersys/ref/battery.html?s_tid=doc_ta (accessed 15/07/2024.

[149] S. S. Acharige, M. E. Haque, M. T. Arif, N. Hosseinzadeh, K. N. Hasan, and A. M. T. Oo, "Review of electric vehicle charging technologies, standards, architectures, and converter configurations," *IEEE Access,* vol. 11, pp. 41218-41255, 2023.

[150] S. B. Shahapure, V. A. Kulkarni, and S. M. Shinde, "A Technology Review of Energy Storage Systems, Battery Charging Methods and Market Analysis of EV Based on Electric Drives," *Development,* vol. 6, no. 8, 2022.

[151] Z. Cao, A. Mahmoudi, S. Kahourzade, and W. L. Soong, "An overview of electric motors for electric vehicles," in *2021 31st Australasian Universities power engineering conference (AUPEC)*, 2021: IEEE, pp. 1-6.

[152] Z. Wang, T. W. Ching, S. Huang, H. Wang, and T. Xu, "Challenges faced by electric vehicle motors and their solutions," *IEEE Access,* vol. 9, pp. 5228-5249, 2020.

[153] H. El Hadraoui, M. Zegrari, A. Chebak, O. Laayati, and N. Guennouni, "A multi-criteria analysis and trends of electric motors for electric vehicles," *World Electric Vehicle Journal*, vol. 13, no. 4, p. 65, 2022.

[154] S. Madichetty, S. Mishra, and M. Basu, "New trends in electric motors and selection for electric vehicle propulsion systems," *IET Electrical Systems in Transportation*, vol. 11, no. 3, pp. 186-199, 2021.

[155] S. Thangavel, D. Mohanraj, T. Girijaprasanna, S. Raju, C. Dhanamjayulu, and S. Muyeen, "A comprehensive review on electric vehicle: battery management system, charging station, traction motors," *IEEE access*, vol. 11, pp. 20994-21019, 2023.

[156] S.-H. Kim, *Electric motor control: DC, AC, and BLDC motors*. Elsevier, 2017.

[157] "Emission Test Cycles standards." https://dieselnet.com/standards/cycles/wltp.php (accessed 07 July 2024, 2024).

[158] D. Graovac, M. Purschel, and A. Kiep, "MOSFET power losses calculation using the data-sheet parameters," *Infineon application note*, vol. 1, pp. 1-23, 2006.

[159] H. E. S. Ltd, "Application Note 5SYA 2053-04 Applying IGBTs," 2006. Accessed: 15/07/2024. [Online]. Available: https://search.abb.com/library/Download.aspx?DocumentID=5SYA2053-04&LanguageCode=en&DocumentPartId=&Action=Launch

Appendix A: Microcontroller code for charging and discharging

Microcontroller code for modular battery packs and cell balancing during charging and discharging mode of operation is developed by using MATLAB Simulink "Embedded Coder Support Package for Texas Instruments C2000 Processors". The code was developed in Simulink, which generates the C-code and is embedded directly into the microcontroller using a USB serial communication cable.

Charging:

Initialization

ts=0.05; % for moving average 20 points (1/0.05)

tavg=1; % for moving average

adcgain=3/4095; % binary to BCD (binary code decimal) conversion, 12-bit ADC maximum input value (0-4095)

Simulink code

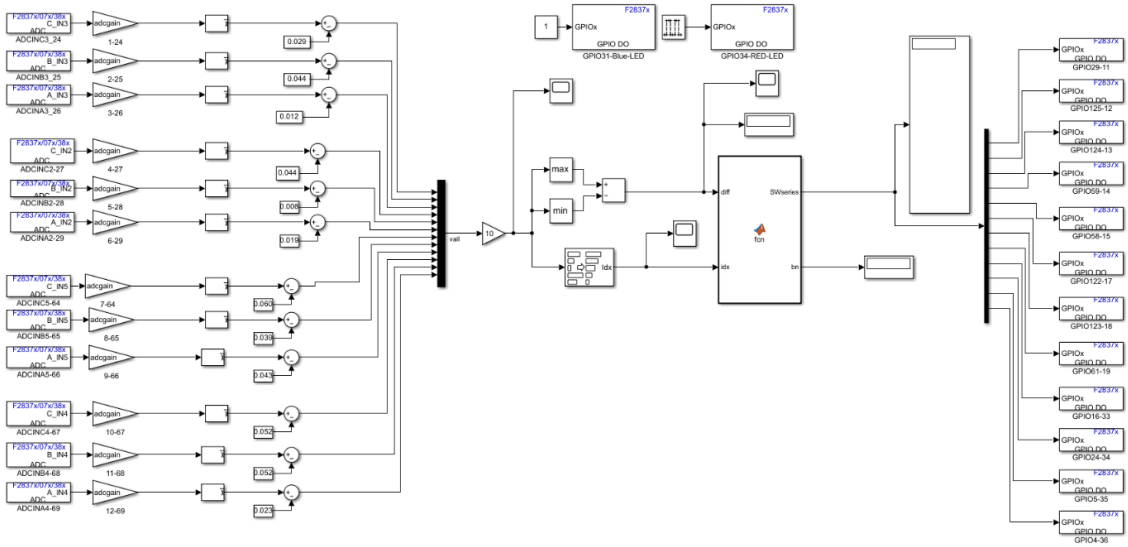

Figure A. 1 Cell balancing code during charging operation

MATLAB S-function code

```
function [SWseries,bn] = fcn(diff, idx)
if(diff>=0.500)
    bn=5;
elseif(diff<0.500 && diff>=0.400)
    bn=4;
elseif(diff<0.400 && diff>=0.300)
    bn=3;
elseif(diff<0.300 && diff>=0.200)
    bn=2;
elseif(diff<0.200 && diff>=0.100)
    bn=1;
else
    bn=0;
end
SWseries=ones(1,12);
for i=1:bn
   SWseries(1,idx(i))=0;
end
end
```

Discharging:

Initialization

ts=0.05; % for moving average 20 points (1/0.05)

tavg=1; % for moving average

adcgain=3/4095; % binary to BCD (binary code decimal) conversion, 12-bit ADC maximum input value (0-4095)

Simulink code

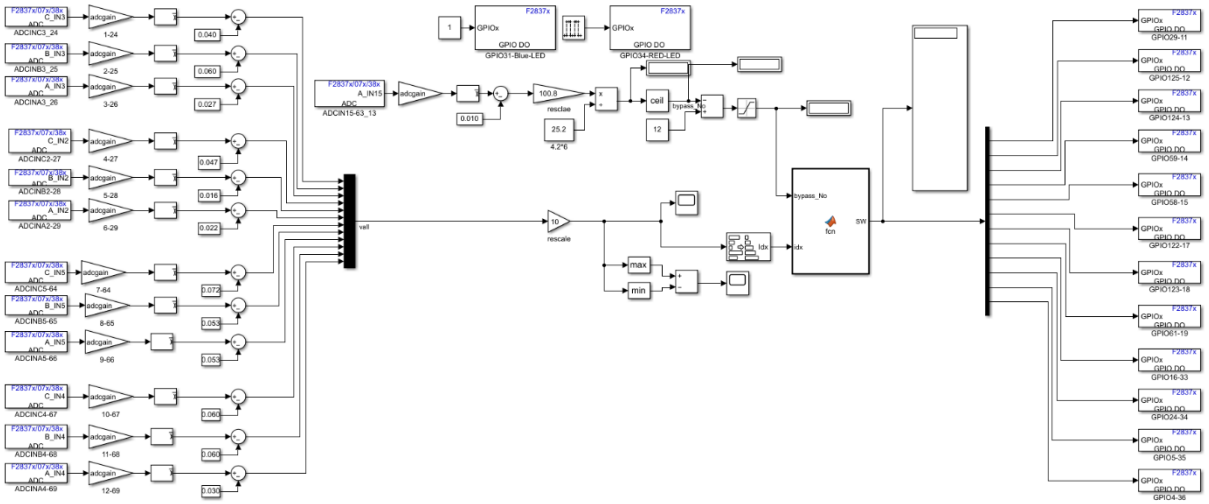

Figure A. 2 Cell balancing code during discharging operation

MATLAB S-function code

```
function SW = fcn(bypass_No, idx)
SW=ones(1,12);
 if (bypass_No >= 0)
    for i=1:bypass_No
        SW(1,idx(i))=0;
    end
 end
end
```

Appendix B: Multiple cases of initial SOC and voltage imbalance results

Results of low voltage battery pack during charging mode

The proposed topology is tested for multiple C-rates with multiple initial SOC difference to prove the performance of controller and proposed method.

Case 1: 50% maximum initial SOC Difference

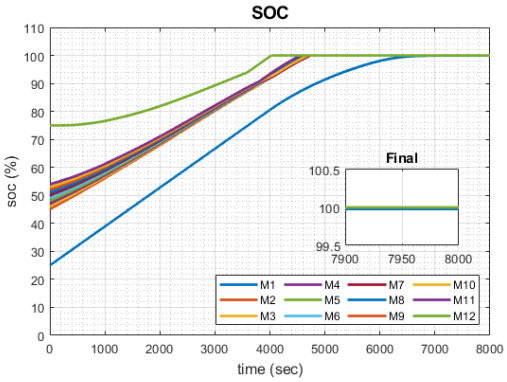

(a) soc graph

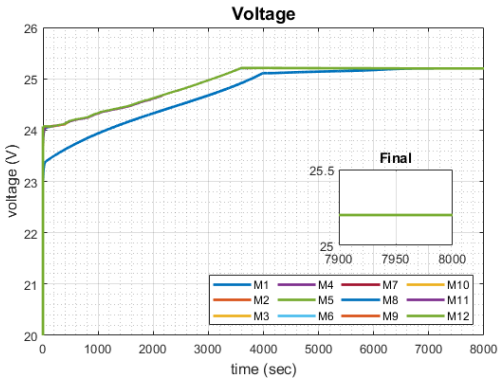

(b) voltage graph

Case 2: 30% maximum initial SOC Difference

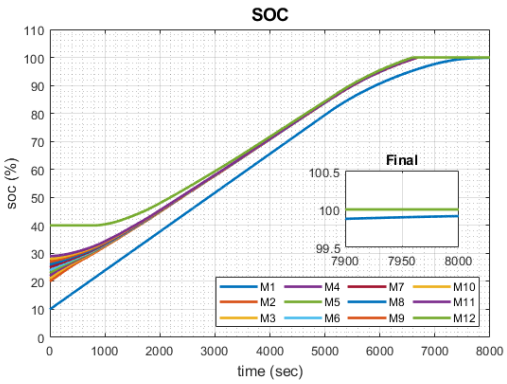

(c) soc graph

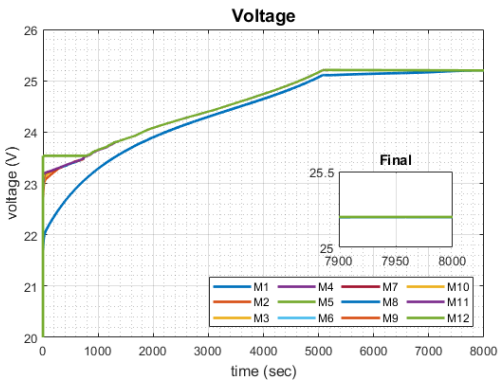

(d) voltage graph

Figure B. 1 Results of charging for multiple cases initial SOC difference at 0.5C-rate

Case 1: 50% maximum initial SOC Difference

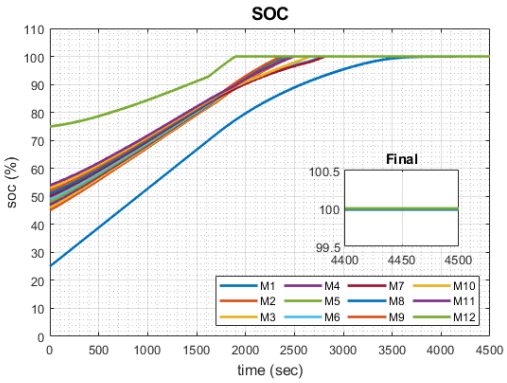

(a) soc graph

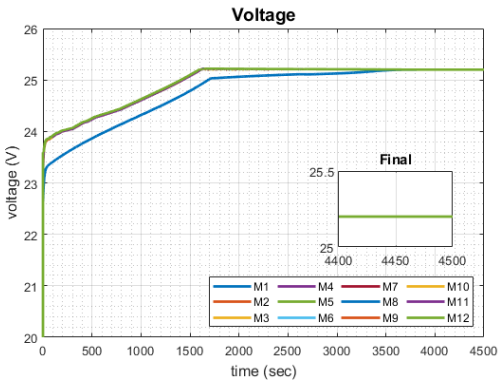

(b) voltage graph

Case 2: 30% maximum initial SOC Difference

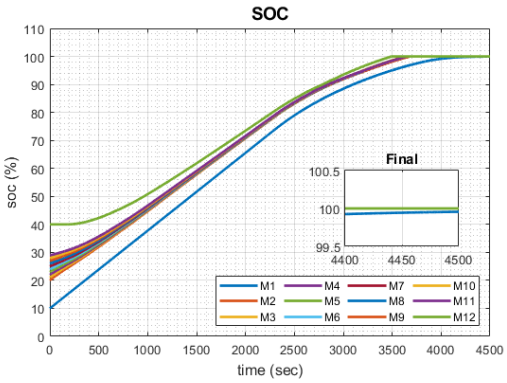

(c) soc graph

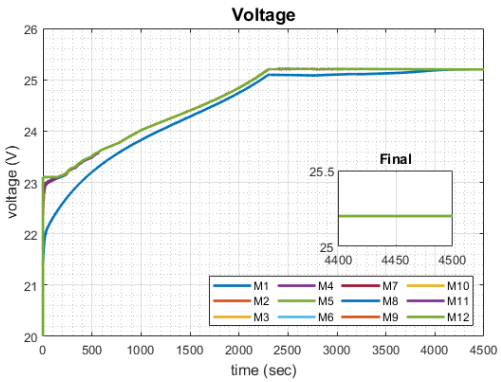

(d) voltage graph

Figure B. 2 Results of charging for multiple cases initial SOC difference at 1C-rate

Case 1: 50% maximum initial SOC Difference

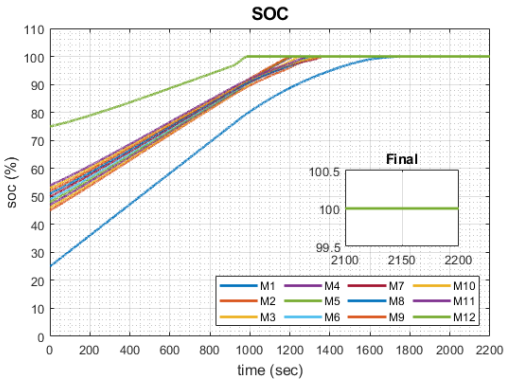

(a) soc graph

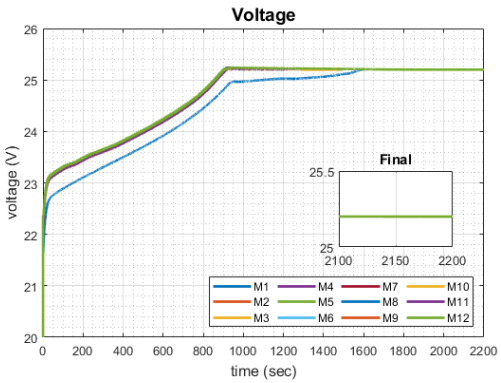

(b) voltage graph

Case 2: 30% maximum initial SOC Difference

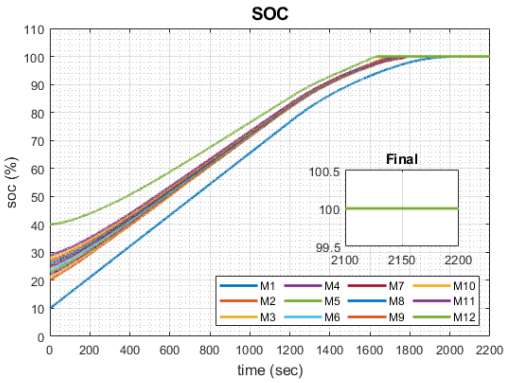

(c) soc graph

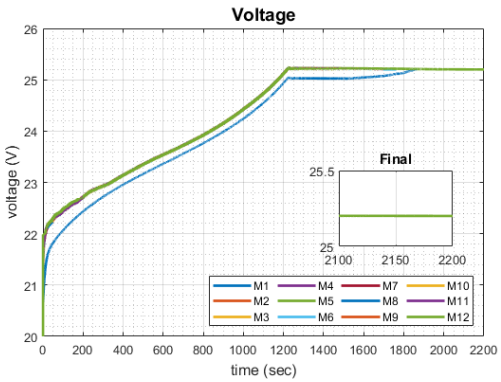

(d) voltage graph

Figure B. 3 Results of charging for multiple cases initial SOC difference at 2C-rate

Results of high voltage battery pack during charging mode

The propped bypass method with a greater number of modules connected in series is tested for 0.5C and 1C rate of charging.

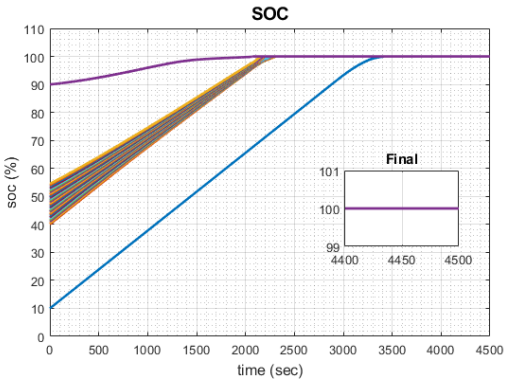

(a) soc graph

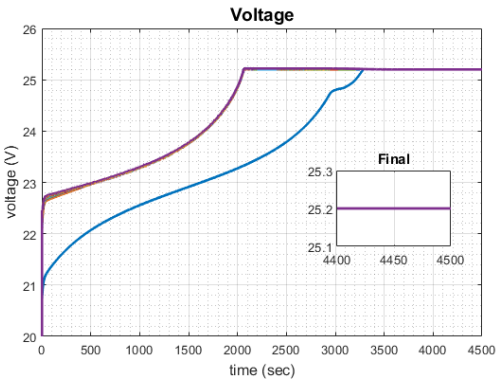

(b) voltage graph

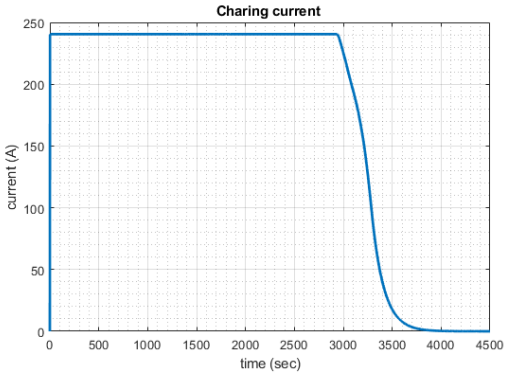

(c) charging current (1C-rate)

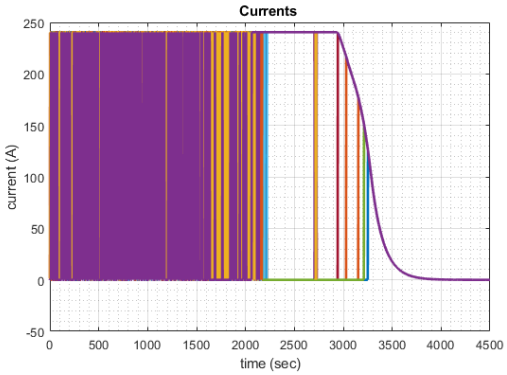

(d) individual modules currents

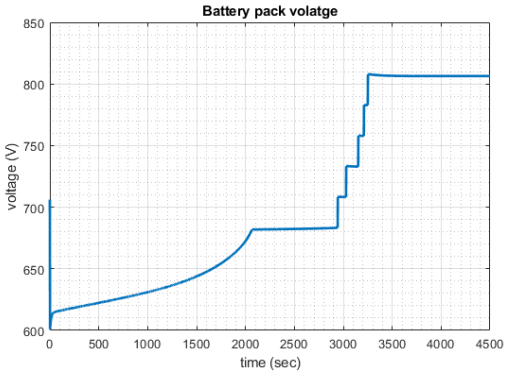

(e) battery pack voltage

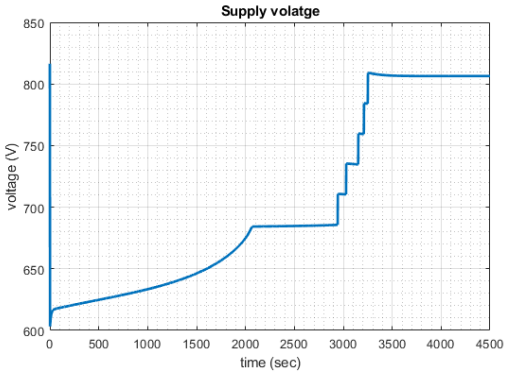

(f) supply voltage

Figure B. 4 High voltage battery charging at 1C rate

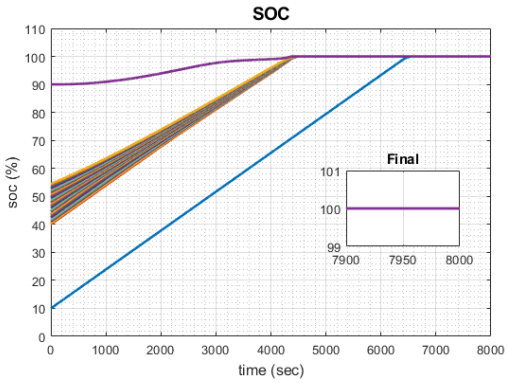

(a) soc graph

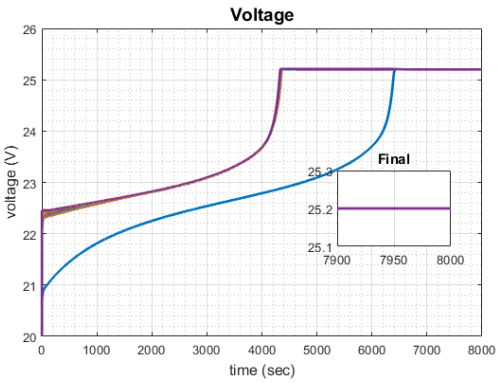

(b) voltage graph

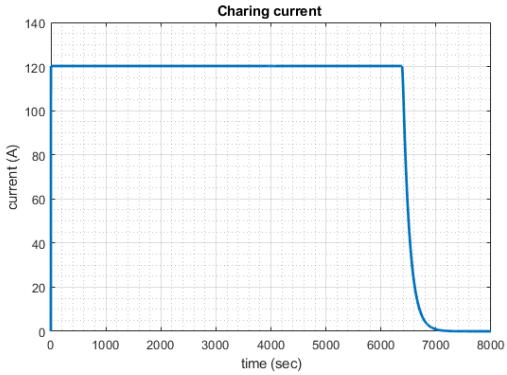

(c) charging current (2C-rate)

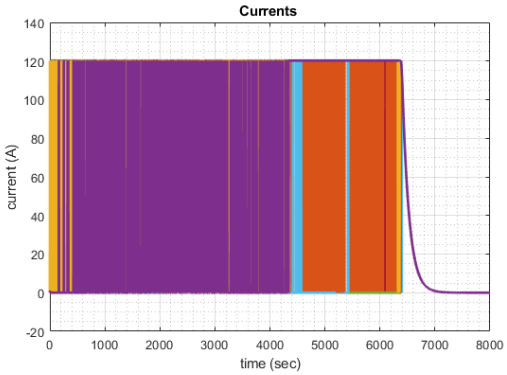

(d) individual modules currents

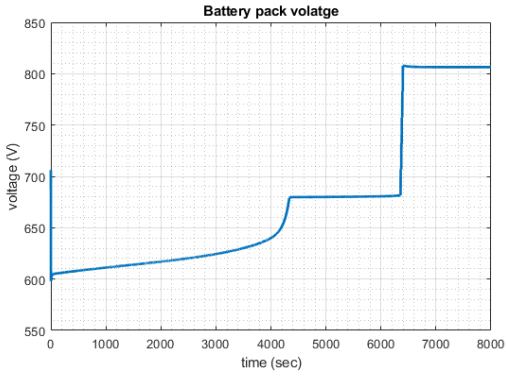

(e) battery pack voltage

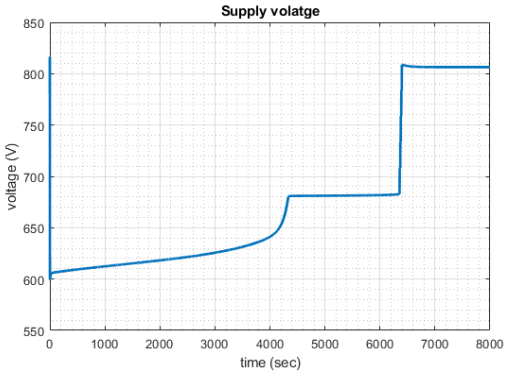

(f) supply voltage

Figure B. 5 High voltage battery charging at 0.5C-rate

Results of high voltage battery pack during discharging mode

The proposed topology is tested for higher voltage battery pack, variable speed, and multiple initial SOC difference (10% and 20%) to prove the performance of controller and proposed method during discharging mode.

Case 1: 20% maximum initial SOC Difference

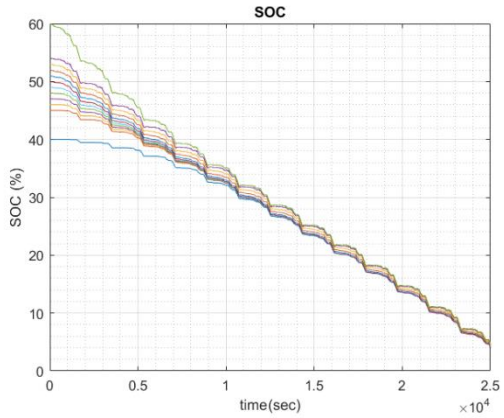

(a) soc graph

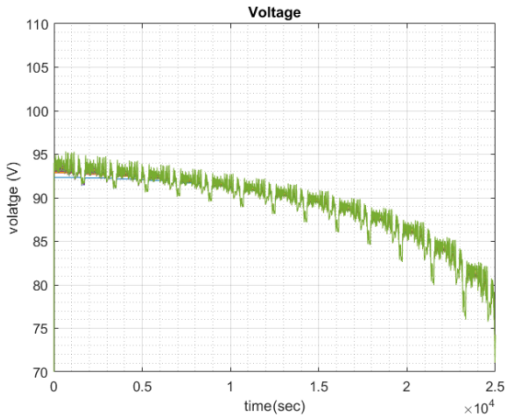

(b) voltage graph

Case 2: 11% maximum initial SOC Difference

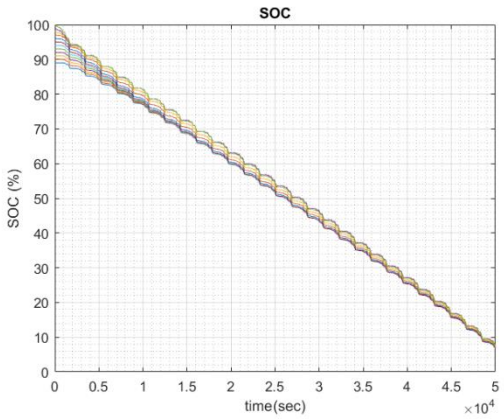

(c) soc graph

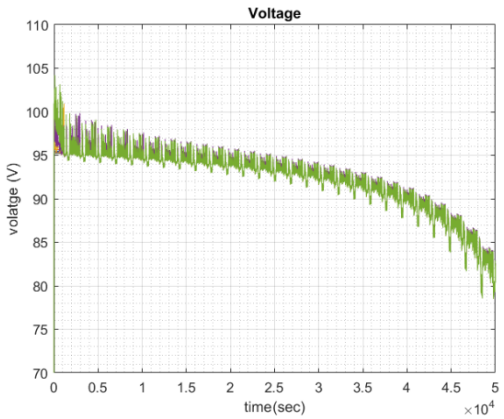

(d) voltage graph

Figure B. 6 Simulation results of discharging for multiple cases with higher voltage